UNIVERSIDADE FEDERAL DO RIO GRANDE DO NORTE
TELECOM PARISTECH

METAMATERIAL INSPIRED IMPROVED ANTENNAS AND CIRCUITS

DAVI BIBIANO BRITO

NATAL, RN - BRAZIL
DECEMBER 2010

UNIVERSIDADE FEDERAL DO RIO GRANDE DO NORTE
TELECOM PARISTECH

Metamaterial Inspired Improved Antennas and Circuits

Davi Bibiano Brito

D.Sc. Dissertation presented to the UFRN Graduate Program in Electrical and Computer Engineering (Area: Telecommunications) and Telecom ParisTech Graduate Program in Electronics and Telecommunications as part of the requirements to obtain the title of Doctor of Science.

Natal, RN - Brazil
December 2010

Metamaterial Inspired Improved Antennas and Circuits

A Thesis Presented to The Academic Faculty

by

Davi Bibiano Brito

In Partial Fulfillment Of the Requirements for the Degree Doctor of Science in Electrical Engineering

Advisor: Prof. Dr. Adaildo Gomes d'Assunção (UFRN)
Advisor: Prof. Dr. Xavier Begaud (Telecom ParisTech)
Co-Advisor: Prof. Dr. Humberto César Chaves Fernandes (UFRN)
Examiner: Prof. Dr. José Ricardo Bergmann, (PUC-Rio)
Examiner: Prof. Dr. Tan-Phu Vuong (INPG-Grenoble)
Examiner: Prof. Dr. Gervásio Protásio dos Santos Cavalcante (UFPA)
Examiner: Prof. Dr. Bernard Huyart (Telecom ParisTech)

Ata da 61ᵃ sessão de defesa de Tese de Doutorado do Programa de Pós-graduação em Engenharia Elétrica e de Computação da UFRN, realizada em 06 de dezembro de 2010 no Auditório do NUPEG/UFRN.

1 Aos 06 (seis) dias do mês de dezembro do ano de dois mil e dez, foi realizada a
2 sexagésima primeira sessão de defesa de tese de doutorado do Programa de Pós-
3 Graduação em Engenharia Elétrica e de Computação da UFRN, na qual o
4 doutorando **Davi Bibiano Brito** apresentou o trabalho que tem como título:
5 **"Metamaterial Inspired Improved Antennas and Circuits"**. A sessão teve início
6 às 09h00min, tendo a banca examinadora sido constituída pelos participantes:
7 Bernard Huyart (Dr. Telecom ParisTech – Examinador Externo –Presidente),
8 Xavier Begaud (Dr. Telecom ParisTech – Orientador), Adaildo Gomes d'Assunção
9 (Dr. UFRN – Orientador), Humberto César Chaves Fernandes (Dr. UFRN – Co-
10 Orientador), José Ricardo Bergmann (Dr. PUC-Rio – Relator – Examinador
11 Externo), Tan-Phu Vuong (Dr. INPG-Grenoble – Relator – Examinador Externo) e
12 Gervásio Protásio dos Santos Cavalcante (Dr. UFPA – Examinador Externo). Após
13 a apresentação do trabalho e o exame pela banca, o doutorando foi considerado
14 APROVADO_____, do que eu, Paulo Yvens Farias Rolim, lavrei a presente ata, que
15 vai assinada pelos examinadores, pelo doutorando e por mim.
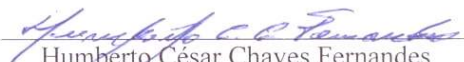

_____
Bernard Huyart
(Examinador Externo – Presidente)

_____
Davi Bibiano Brito
(Doutorando)

_____
Xavier Begaud
(Orientador)

_____
Adaildo Gomes d'Assunção
(Orientador)

_____
Humberto César Chaves Fernandes
(Co-orientador)

_____
José Ricardo Bergmann
(Relator – Examinador Externo)

_____
Tan-Phu Vuong
(Examinador Externo)

_____
Gervásio Protásio dos Santos Cavalcante
(Examinador Externo)

_____
Paulo Yvens Farias Rolim
(Secretário – PPgEEC)

In Loving Memory Of My Beloved Mother

Acknowledgements

Foremost, I would like to express my sincere gratitude to my advisors Prof. Adaildo Gomes D'Assunção, Prof. Xavier Begaud and Prof. Humberto César Chaves Fernandes for the continuous support of my Ph.D study and research, for their patience, motivation, and immense knowledge. Their guidance helped me in all the time of research and writing of this thesis. Besides my advisors, I would like to thank my fellow labmates at UFRN and Telecom ParisTech for the stimulating discussions and for all the fun we have had in the last four years.

Last but not the least, I would like to thank my family for all their love and encouragement. My Grandparents Rafael, Dione and Maria for their love and support. My Uncle José for his help. For my parents Dacio e Roberta (for giving birth to me at the first place) who raised me with a love of science and supported me in all my pursuits. And most of all for my loving, supportive, encouraging, and patient Pollyana whose faithful support during the final stages of this Ph.D. is so appreciated. Thank you all.

List of Publications

D. B. Brito, "Metamaterial Inspired Improved Antennas and Circuits", Tese de Doutorado, PGGEEC - UFRN, COMELEC – TELECOM PARISTECH, Natal-RN, dezembro de 2010, 102 p.

D. B. Brito, X. Begaud, A. G. D'Assuncao, and H. C. C. Fernandes, "Ultra wideband monopole antenna with Split Ring Resonator for notching frequencies", EuCAP 2010. 4th European Conference on Antennas and Propagation, pp. 1 - 5, Barcelona, Espanha, Abril 2010.

D. B. Brito, X. Begaud, A. G. D'Assuncao, and H. C. C. Fernandes, "Ultra Wideband Monopole Antenna using Split Ring Resonator", COSTic0803 3rd Management Committee/Working Group, Meeting and Workshop, Atenas, Grécia, Outubro 2009.

D. B. Brito, H. C. C. Fernandes, "Unilateral Fin Line Directional Coupler". International Journal of Infrared and Millimeter Waves, v. 28, p. 651-661, Setembro 2007.

Table of Contents

List of Acronyms and Symbols

$\vec{\nabla}$	Nabla operator
$\vec{B}$	Magnetic field
c	Velocity of light
CSRR	Complementary Split Ring Resonator
$\vec{D}$	Electric displacement field
DNG	Double-Negative
DPS	Double-Positive
$\vec{E}$	Electric field
EBG	Electromagnetic Band-Gap
ENG	Epsilon-negative
ε_0	Free space permittivity
ε_{eff}	Effective permittivity
ε_r	Relative permittivity
FSS	Frequency Selective Surfaces
FP	Fabry-Pérot
$\vec{H}$	Magnetizing field
HIS	High Impedance Surface
$\vec{k}$	Wave vector
LHM	Left Handed Metamaterial
λ	Wavelength
λ_0	Free space wavelength
λ_g	Guided wavelength
MNG	Mu-Negative
μ_0	Free space permeability
μ_{eff}	Effective permeability
μ_r	Relative permeability
η	Index of refraction
PCB	Printed Circuit Board
PEC	Perfectly Electrically Conducting
RF	Radio Frequency
$\vec{S}$	Poynting vector
SNG	Single-Negative
SRR	Split Ring Resonator
σ	Conductivity of the metal
TW	Thin-Wire
ω	Angular frequency

List of Figures

List of Tables

Abstract

Metamaterials exhibiting negative refraction have attracted a great amount of attention in recent years mostly due to their exquisite electromagnetic properties. These materials are artificial structures that exhibit characteristics not found in nature. It is possible to obtain a metamaterial by combining artificial structures periodically. We investigated the unique properties of Split Ring Resonators, High impedance Surfaces and Frequency Selective Surfaces and composite metamaterials. We have successfully demonstrated the practical use of these structures in antennas and circuits. We experimentally confirmed that composite metamaterial can improve the performance of the structures considered in this thesis, at the frequencies where electromagnetic band gap transmission takes place.

Keywords: Left-Handed Material, Metamaterial, Split Ring Resonator, Negative Permittivity, Negative Permeability, High Impedance Surface, Frequency Selective Surface, Electromagnetic Band Gap, Negative Refraction, Fabry-Pérot.

Chapter 1

Introduction

Recently developments in electromagnetics in the radio frequency to optical spectral ranges and novel fabrication techniques offer a great number of exciting new applications. These structures are called metamaterials and they have electromagnetic characteristics that do not occur or are not readily available in natural materials.

The purpose of this thesis is to develop new structures, for communication systems that can provide improved functionality and performance. The great potential of metamaterials to develop such novel structures offers an alternative with potential to overcome limitations of current solutions. In this context metamaterials is a breakthrough, mainly to their exquisite material properties and ability to guide and control electromagnetic waves in a way that natural occurring materials cannot.

The thesis is organized into seven chapters. Chapter 2 presents the general theory of metamaterials that enables its characterization, including the behavior of electromagnetic waves explained through the Maxwell`s equations. Metamaterials, which have special optical properties such as a negative refractive index are described. Metamaterials examples like the Split Ring Resonator (SRR) and the High Impedance Surface (HIS) that will be used in this thesis are presented.

In Chapter 3 the Frequency Selective Surfaces (FSS) are studied with a brief stated of art, types and forms of the most used structures and some applications are presented. The typical behavior of the most common element types available to the FSS designers are discussed. The Frequency Selective Surface theory is considered starting with a comparison of available elements to the metamaterial FSS variants. Finally this section ends with a discussion of wideband radiating arrays.

Chapter 4 describes the use of a Complementary Split Ring Resonator (CSRR) in two metamaterials applications; in the first the CSRR is placed as a parasite element in the conductor patch of a microstrip circular monopole. This metamaterial structure is used as a

stop band filter for blocking the Unlicensed National Information Infrastructure (UN-II) band between 5 GHz to 6 GHz. The second application is a microstrip filter that is used as an alternative for blocking the UN-II band. The band-notched characteristic is achieved by etching a CSRR structure in the ground plane of a microstrip transmission line. It has been demonstrated that CSRR etched in the ground plane of a planar transmission media (microstrip) provides a negative effective permittivity to the structure.

In Chapter 5 a HIS metallic electromagnetic structure is used as ground plane in two directive antennas, a patch antenna and a suspended U-Shaped antenna. This structure is characterized by having high surface impedance. Unlike normal conductors, this surface does not support propagating surface waves, and it reflects electromagnetic waves with no phase reversal, which can be used to improve the antennas performance.

Chapter 6 describes the use of the Fabry-Pérot (FP) optical concept as an alternative to produce highly directive antennas. This FP medium is formed employing a HIS as a metamaterial substrate and a FSS as a partially reflecting surface (PRS) superstrate. The used antennas are those described in Chapter 5. This configuration leads to single feed and low profile highly directive antennas. In addition some optical concepts are presented for a better understanding. Chapter 7 presents the conclusions and perspectives for future works.

Chapter 2

Metamaterials

There have been a large number of definitions for metamaterials [1-8], they can be generally defined as a class of ''artificial'' media, exhibiting extraordinary electromagnetic properties that cannot be found in natural ones [1]. The name given to this structurally altered materials is based on the Greek μετά (meta) that means "beyond". The subject of metamaterials have seen many exciting applications and has drawn considerable attention from both the physics and engineering communities worldwide. The interest for both communities can be explained by the fact that physicists normally study the way nature works while engineers try to apply the knowledge and metamaterials can be place in between science and engineering.

From the point of view of fundamental science nothing is new in metamaterials theory. Throughout this chapter, it will be shown that metamaterials can be understood by using well-known theoretical tools, however, almost all new applications arising from metamaterial concepts can be understood by using more conventional approaches, that is, without the need to invoke these metamaterial concepts.

2.1 Metamaterials Overview

During the research process to write this document the first attempt to explore the concept of "artificial" materials appears back to 1898 when J. C. Bose [9] conducted the first microwave experiment on twisted structures, geometries that were essentially artificial chiral[1] elements by today's terminology. In 1905, Lamb [10] suggested the existence of backward waves, which are associated with reflection directions based on the signs of permittivity and

permeability. Since then, artificial complex materials have been the subject of research worldwide.

A key feature of these artificial materials is the negative refraction, that some titles leads to the given name "left handed materials" (LHM), materials that refract light in a way which is contrary to the normal "right handed" rules of electromagnetism, Fig. 2.1. When an electromagnetic wave passes through this material the electric vector $\vec{E}$, the electromagnetic vector $\vec{H}$ and the wave vector $\vec{k}$ do not abide the right-handed law. The first study of general properties of wave propagation in such a LHM medium has been attributed to Veselago [11]. In his work he showed that a plate of material with negative index of refraction would focus light in the same way that a curved lens made with conventional materials, in the absence of any material that had these properties. This initial work fell into obscurity.
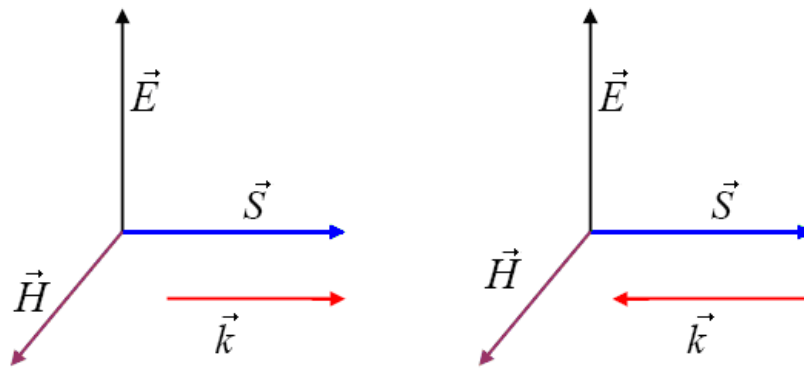
Fig. 2.1 – Diagram showing the Poynting vectors of an electromagnetic wave. On left, normal materials, and on the right metamaterials.

Permittivity (ε) and permeability (μ) are two parameters used to characterize the electric and magnetic properties of materials interacting with the electromagnetic fields. The permittivity is a measure of how much a medium changes to absorb electrical energy when subjected to an electric field. It relates $\vec{D}$ and $\vec{E}$, where $\vec{D}$ is the electric displacement by the medium and $\vec{E}$ is the electric field strength. The common term dielectric constant is the ratio of permittivity of the material to that of free space ($\varepsilon_0 = 8.85 \times 10^{-12}$). It is also named as the relative permittivity. Permeability is a constant of proportionality that exists between magnetic induction and magnetic field intensity. Free space permeability μ_0 is approximately 1.257×10^{-6} [1].

---

[1]In geometry, a figure is chiral, and said to have chirality, if it is not identical to its mirror image, or more particularly if it cannot be mapped to its mirror image by rotations and translations alone. A chiral object and its mirror image are said to beenantiomorphs.

As mentioned before, Electric permittivity and magnetic permeability are the parameters that determine the electric and magnetic properties of materials. Together they determine the material's response to electromagnetic radiation. In ordinary materials both permittivity and permeability are positive. However, for such metamaterials the effective permittivity and effective permeability are negative values but the propagation of electromagnetic waves is still possible since their product remains positive.

In this case, the refractive index in the Snell's law[2] is negative, an incident wave experiences a negative refraction at an interface, and we have a backward wave for which the phase of the waves moves in the direction opposite to the direction of the energy flow [3]. Assuming an isotropic medium, the ray diagram for an interface between a medium with a positive index of refraction and a LHM can be seen in Fig. 2.2.
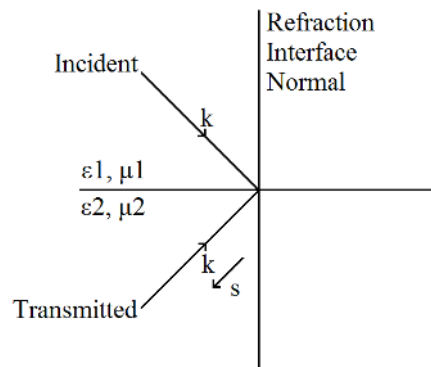
Fig. 2.2 – Ray diagram of interface between n>0 and n<0 media.

The diagram shown in Fig. 2.2 can be explained by using Snell's law. For the case where the refractive index is positive for both media the ray could pass through the interface. When the refractive indexes are $\eta_1 > 0$ and $\eta_2 < 0$ the transmitted beam travels through the second medium on the same side of the incident wave in the normal direction [7]. The resulting wave moves backwards. That can be explained with the help of Fig. 2.1 were the poynting vector $\vec{S}$ is in the direction of energy flow and continues in the same direction as in a normal material but the wave vector k propagates in the negative direction.

$$\eta = \pm\sqrt{\mu\varepsilon} \tag{2.1}$$

[2]In optics and physics, Snell's law (also known as Descartes' law, the Snell–Descartes law, and the law of refraction) is a formula used to describe the relationship between the angles of incidence and refraction, when referring to light or other waves passing through a boundary between two different isotropic media, such as water and glass. This law says that the ratio of the sines of the angles of incidence and of refraction is a constant that depends on the media.

Ziolkowski [5] has categorized metamaterials by their constitutive parameters as described in Fig. 2.3. In the equation 2.1 the ± sign is assumed for general proposes. The four possible combinations for the sign of ε and μ are (+,+), (+,-), (-,+) and (-,-). Most of the materials in nature have positive permittivity and permeability, and hence, they are referred to as double-positive (DPS) media. In contrast, if both of these quantities are negative, they are called double-negative (DNG) or LHMs.

Therefore, materials with one negative parameter are named single-negative (SNG) and are further classified into two subcategories, namely, epsilon-negative (ENG) and mu-negative (MNG). Interestingly, natural materials such as cold plasma and silver exhibit negative permittivities at microwave and optical frequencies, respectively, and ferromagnetic materials exhibit a negative permeability behavior in the VHF and UHF regimes. However, to date, no materials that exhibit simultaneous negative permittivity and permeability have been found in nature, so, they must be designed artificially.
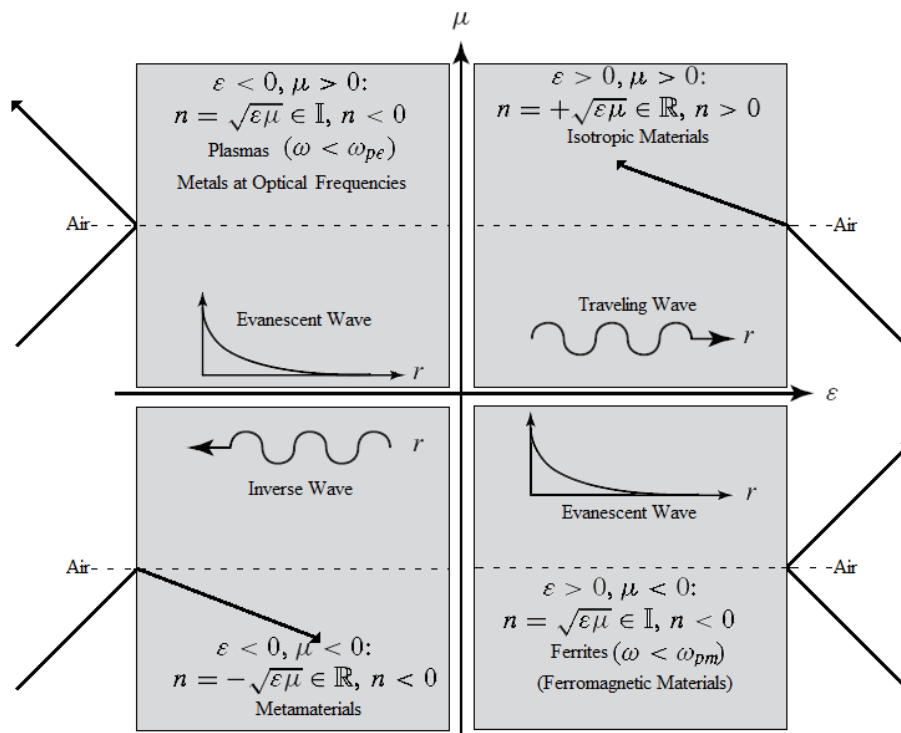
Fig. 2.3 – A diagram showing the possible domains of electromagnetic materials and wave refraction having the same sign. Waves are refracted positively in conventional materials and negatively in LHMs.

The arrows in Fig. 2.3 represent wave vector directions in each medium. There is wave transmission only when both parameters waves in which the phase propagates in a direction opposite to that of the energy flow. The wave propagation directions, using the diagram of

rays for normal materials (isotropic) and metamaterials is shown in Fig. 2.4, when a wave is obliquely incident to the material. It may be noted in the natural materials that have refraction in the first interface is up compared to normal while in the artificial material is down.
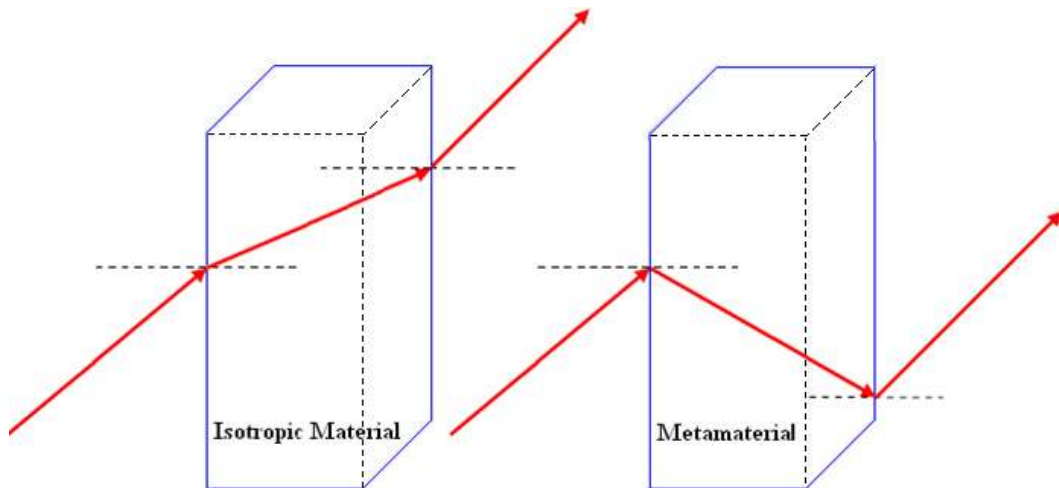
Fig. 2.4 – Ray diagram showing the direction of wave propagation.

Artificial dielectrics, the first known metamaterials, usually consist of artificially created molecules: dielectric or metallic inclusions of a certain shape. These molecules can be distributed and oriented in space, either in a regular lattice or in a random manner one example of such organization is given in Fig. 2.5 [1].
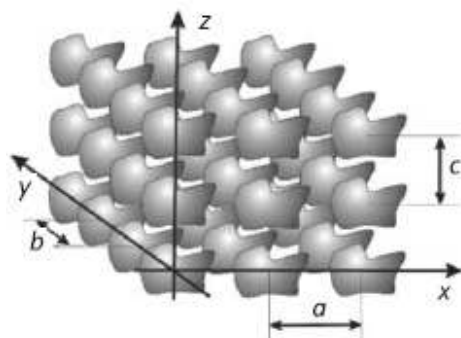
Fig. 2.5 – The geometry of a generic artificial dielectric.

The dimensions of the molecules and the characteristic distance between neighboring molecules are considered very small when compared to the wavelength. However, the size of

a single inclusion is usually much smaller than that of a real molecule in a network of natural crystals. This consideration allows the description of the inclusions in terms of material parameters and the resulting metamaterial can be characterized using Maxwell equations [1].

2.2 Electromagnetic Wave Propagation in a Metamaterial Media

Starting with the Maxwell equations reduced to the wave equation [11]:

$$\left(\nabla^2 - \frac{\eta^2}{c^2}\frac{\partial^2}{\partial t^2}\right)\psi = 0 \tag{2.2}$$

where "η" is the refractive index, "c" is the velocity of light in vacuum, and $n^2/c^2 = \mu\varepsilon$. Knowing that the squared refractive index "η^2" is not affected by a simultaneous change of sign in μ and ε, it can be noted that the low-loss left-handed media must be transparent. Considering the above equation, it can be observed that its solutions will remain unchanged after a simultaneous change of the signs of μ and ε. The general expressions of a plane wave are:

$$\vec{E} = \vec{E_o}e^{-j\vec{k}\vec{r}} \tag{2.3}$$

$$\vec{H} = \vec{H_o}e^{-j\vec{k}\vec{r}} \tag{2.4}$$

where $\vec{E_o}$ and $\vec{H_o}$ are vectors in arbitrary directions, $\vec{k}$ is the vector propagation constant whose magnitude is k and whose direction is the direction of propagation of the wave and $\vec{r}$ is the observation position vector.

$$\vec{k} = k_x\hat{x} + k_y\hat{y} + k_z\hat{z} \tag{2.5}$$

$$k = \sqrt{k_x^2 + k_y^2 + k_z^2} \tag{2.6}$$

$$\vec{r} = x\hat{x} + y\hat{y} + z\hat{z} \tag{2.7}$$

Instead of solving Maxwell's equations directly to obtain wave solutions, we will transform the system of first order partial differential equations into a single second order partial differential equations that is easier to solve. We start with Maxwell's equations in time harmonic form,

$$\nabla \times \vec{E} = -j\omega \vec{B} \tag{2.8}$$

$$\nabla \times \vec{H} = j\omega \vec{D} + \vec{J} \tag{2.9}$$

Knowing that,

$$\nabla \cdot \vec{B} = \nabla \cdot \mu \vec{H} = 0 \tag{2.10}$$

$$\nabla \cdot \vec{D} = \nabla \cdot \varepsilon \vec{E} = \rho_v \tag{2.11}$$

Equations 2.8 and 2.9 can be rewritten as,

$$\nabla \times \vec{E} = -j\omega \mu \vec{H} \tag{2.12}$$

$$\nabla \times \vec{H} = j\omega \varepsilon \vec{E} + \vec{J} \tag{2.13}$$

In order to handle lossy materials, we first rewrite Ampere's Law. If we have a medium which has free charge allowing current flow, then $\vec{J} = \sigma \vec{E}$, and

$$\nabla \times \vec{H} = j\omega \varepsilon \vec{E} + \sigma \vec{E} = j\omega \left[\varepsilon + \frac{\sigma}{j\omega} \right] \vec{E} \tag{2.14}$$

$$\nabla \times \vec{H} = j\omega \varepsilon \vec{E} + \sigma \vec{E} = j\omega \underbrace{\left[\varepsilon - j\frac{\sigma}{\omega} \right]}_{\varepsilon_{ef}} \vec{E} \tag{2.15}$$

This shows that in the phasor domain, the conductivity can be lumped together with the permittivity to produce a new effective complex permittivity:

$$\varepsilon_{ef} = \varepsilon - \frac{j\sigma}{\omega} = \varepsilon_0 \left[\varepsilon_r - j\frac{\sigma}{\omega \varepsilon_0} \right] = \varepsilon_0 \varepsilon_{ref} \tag{2.16}$$

A different notation can be used,

$$\varepsilon_{ef} = \varepsilon' - j\varepsilon' \qquad (2.17)$$

for the real and imaginary parts of the complex permittivity. This reduces Ampere's law for a lossy material into the form

$$\nabla \times \vec{H} = j\varepsilon\omega\vec{E} \qquad (2.18)$$

where ε is complex. It can be shown that we have the following relations for the field vectors and the propagation direction.

$$\vec{E} \perp \vec{H} \perp \vec{k} \qquad (2.19)$$

$$\vec{H} = \frac{1}{\eta}\hat{k}\times\vec{E} \qquad (2.20)$$

$$\vec{E} = \eta\vec{H}\times\hat{k} \qquad (2.21)$$

For the plane-wave fields of the kind $\vec{E} = \vec{E}_0\exp(-j\vec{k}\cdot\vec{r} + j\omega t)$ and $\vec{H} = \vec{H}_0\exp(-j\vec{k}\cdot\vec{r} + j\omega t)$, equations 2.12 and 2.18 can be reduced to:

$$\vec{k}\times\vec{E} = \omega\mu\vec{H} \qquad (2.22)$$

$$\vec{k}\times\vec{H} = -\omega\varepsilon\vec{E} \qquad (2.23)$$

Therefore, for positive μ and ε, $\vec{E}$, $\vec{H}$ and $\vec{k}$ form a right-handed orthogonal system of vectors, Fig 2.1 (a). However, if $\mu < 0$ and $\varepsilon < 0$, equations 2.22 and 2.23 can be rewritten as

$$\vec{k}\times\vec{E} = -\omega|\mu|\vec{H} \qquad (2.24)$$

$$\vec{k}\times\vec{H} = \omega|\varepsilon|\vec{E} \qquad (2.25)$$

In this case it can be shown that $\vec{E}$, $\vec{H}$ and $\vec{k}$ form a left-handed triplet, as illustrated in Figure 2.1. This result mathematically demonstrates the original reason for the denomination of negative μ and ε media as "left-handed" media [6]. The main physical implication of the aforementioned analysis is backward-wave propagation. The direction of the time-averaged flux of energy is determined by the real part of the Poynting vector,

$$\vec{S} = \frac{1}{2}\vec{E}\times\vec{H}^{*} \qquad\qquad (2.26)$$

which is unaffected by a simultaneous change of sign of μ and ε. Thus, $\vec{E}$, $\vec{H}$ and $\vec{S}$ still form a right-handed triplet in a left-handed medium. Therefore, in such media, energy and wavefronts travel in opposite directions (backward propagation). However, backward-wave propagation in unbounded homogeneous isotropic media seems to be a unique property of left-handed media. As it will be shown, most of the unique electromagnetic properties of these media arise from this backward propagation property.

2.3 Artificial Materials

The concept of artificial dielectric materials was first introduced by Kock [12], and used in the design of low-profile dielectric lens at microwave frequencies. An example of artificial dielectric is a wired medium, Fig. 2.6, which was introduced in the 1950s. The permittivity in a medium of wires that has a frequency dependence of the plasma type frequency dependence that is negative below the plasma frequency but small and positive above this frequency. This structure has a negative permittivity and positive permeability.

The first real artificial metamaterial structure was designed and experimentally demonstrated by Smith [13]. This structure was inspired by the work of Pendry [14] who introduced the structure shown in Fig. 2.7b. This structure like the wired medium can be designed to have a plasmatic type frequency dependence in the microwave range. This structure has a negative permeability and positive permittivity.
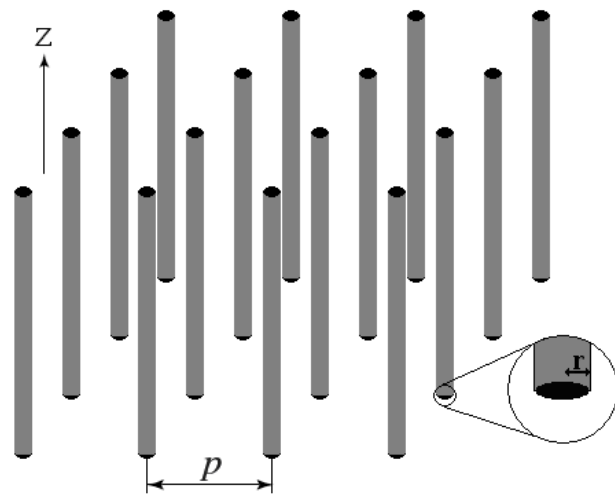
Fig. 2.6 – The geometry of wire medium: a lattice of parallel conducting thin wires.
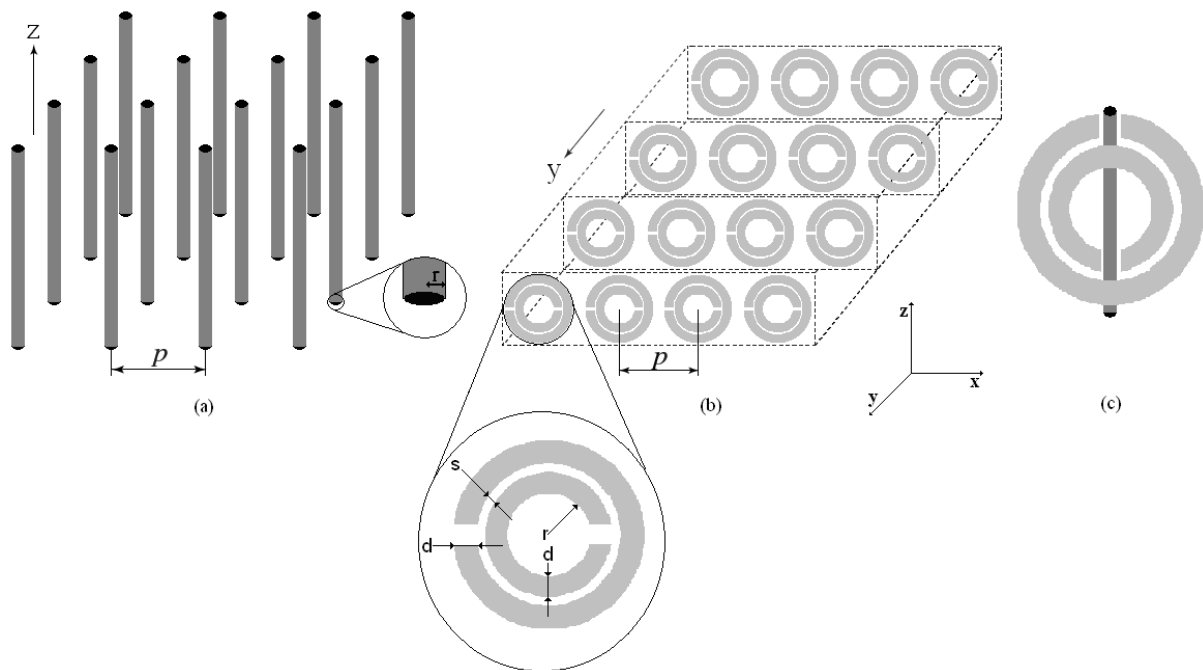
Fig. 2.7 – Metamaterials constructed with common dielectrics and metals: (a) negative permittivity and positive permeability, (b) negative permeability and positive permittivity, and (c) double negative media DNG [15].

In the structure shown in Fig. 2.7a if the excitation electric field $\vec{E}$ is parallel to the axis of the wires $\left(\vec{E} \parallel z\right)$ we have from [15]:

$$\varepsilon_r(\omega) = 1 - \frac{\omega_{pe}^2}{\omega^2 + j\omega\xi} = 1 - \frac{\omega_{pe}^2}{\omega^2 + \zeta^2} + j\frac{\xi\omega_{pe}^2}{\omega(\omega^2 + \zeta^2)} \tag{2.27}$$

where $\omega_{pe}^2 = \sqrt{2\pi c^2/[p^2 \ln(p/r)]}$ (c: speed of light) is the electric plasma frequency, and $\zeta = \varepsilon_0\left(p\omega_{pe}/r\right)^2/\pi\sigma$ (σ: conductivity of the metal) is the damping factor due to metal losses. From [15] we have that:

$$\mathrm{Re}(\varepsilon_r) < 0, \quad \text{for} \quad \omega^2 < \omega_{pe}^2 - \zeta^2 \tag{2.28}$$

if $\zeta = 0$ from [15] we have,

$$\varepsilon_r < 0 \qquad \text{for} \quad \omega < \omega_{pe}. \tag{2.29}$$

The permeability is $\mu = \mu_r$, since there is no magnetic material present ($\mu_r = 1$). The structure shown in Fig. 2.7b if the excitation magnetic field $\vec{H}$ is perpendicular to the plane of the rings $\left(\vec{H} \perp y\right)$ from [15],

$$\mu_r(\omega) = 1 - \frac{F\omega^2}{\omega^2 - \omega_{0m}^2 + j\omega\zeta} = 1 - \frac{F\omega^2(\omega^2 - \omega_{0m}^2)}{\left(\omega^2 - \omega_{0m}^2\right)^2 + (\omega\zeta)^2} + j\frac{F\omega^2\zeta}{\left(\omega^2 - \omega_{0m}^2\right)^2 + (\omega\zeta)^2} \tag{2.30}$$

where $F = \pi(r/p)^2$, $\omega_{0m} = c\sqrt{\frac{3p}{\pi \ln(2dr^3/s)}}$ is a magnetic resonance frequency, and $\zeta = 2pR'$ (R': metal resistance per unit length) is the damping factor due to metal losses. From [15] Equation 2.30 reveals that a frequency range can exist in which $\mathrm{Re}(\mu_r) < 0$ in general ($\zeta \neq 0$). In the lossless case ($\zeta \neq 0$), it appears that [15],

$$\mu_r < 0, \qquad \text{for} \quad \omega_{0m} < \omega < \frac{\omega_{om}}{\sqrt{1-F}} = \omega_{pm} \tag{2.31}$$

where ω_{pm} is the magnetic plasma frequency.

An essential difference between the plasmonic expressions for ε and μ is that the latter is of resonant nature $[\mu(\omega = \omega_{0m}) = \infty]$, whereas the former is a non-resonant expression. The resonance of the structure is due to the resonance of its SRRs, given in [15] by $\omega_{0m}^2 = 3pc^2/[\pi \ln(2d/s)r^3]$.

The pair of concentric rings shown (Fig. 2.7b) is an artificial magnetic material formed by resonant metallic elements. This structure is called Split Ring Resonator (SRR) and due to the small gap between the rings the structure has a larger resonant wavelength then the diameter of the rings. This small space also produces high capacitive values, which reduce the value of the resonance frequency. A magnetic flux penetrating the rings induces a current in the rings that will produce its own current flow that increases or is oppose to the incident field. It results in low radiative losses and in the high value of quality factor. At frequencies below the resonance frequency the real part of the permittivity becomes positive and at frequencies above the resonance becomes negative. This negative permeability along with the negative permittivity of the wire allows the construction of a metamaterial structure shown in Fig. 2.7c.

The equivalent circuit of a SRR is shown in Fig 2.8 [15]. In the double ring configuration (left), capacitive coupling and inductive coupling between the larger and smaller rings are modeled by a coupling capacitance (C_m) and by a transformer (transforming ratio n), respectively. In the single ring configuration (right), the circuit model is that of the simplest RLC resonator with resonant frequency $\omega_0 = 1/\sqrt{LC}$. The double SRR is essentially equivalent to the single SRR if mutual coupling is weak, because the dimensions of the two rings are very close to each other, so that L1 ≈ L2 ≈ L and C1 ≈ C2 ≈ C, resulting in a combined resonance frequency close to that of the single SRR with same dimensions but with a larger magnetic moment due to higher current density.
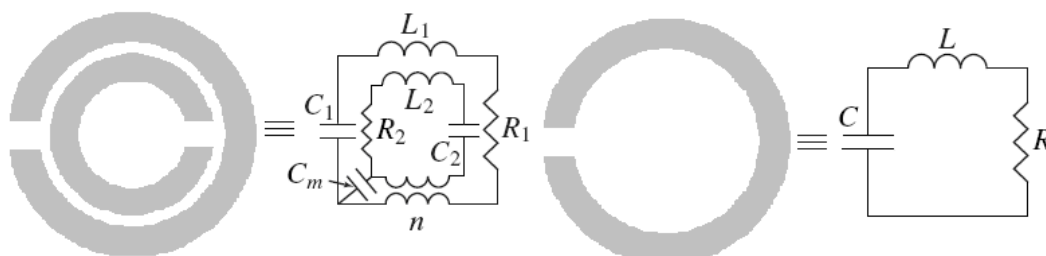
Fig. 2.8 – Equivalent circuit model for the Split Ring Resonator, double and simple rig configurations.

The split-ring resonators are widely used since they can be manufactured using printed circuit technology. The artificial magnetic material with frequency-dependent positive permeability has also been synthesized by using double circular ring resonators. An artificial magnetic material, which is formed by split-ring resonators, exhibits negative permeability within a frequency band (bandwidth is typically narrow) near the resonant frequency of the single split-ring resonator; it is widely used to create LHMs. Theoretical results for the permeability using a thin wire and permittivity using a SRR are shown in Fig. 2.9, the results were obtained from equations 2.27 and 2.30, the substrate material is considered vacuum and a Perfectly Electrically Conducting (PEC) as the material for the CSRR.

(a)

(b)
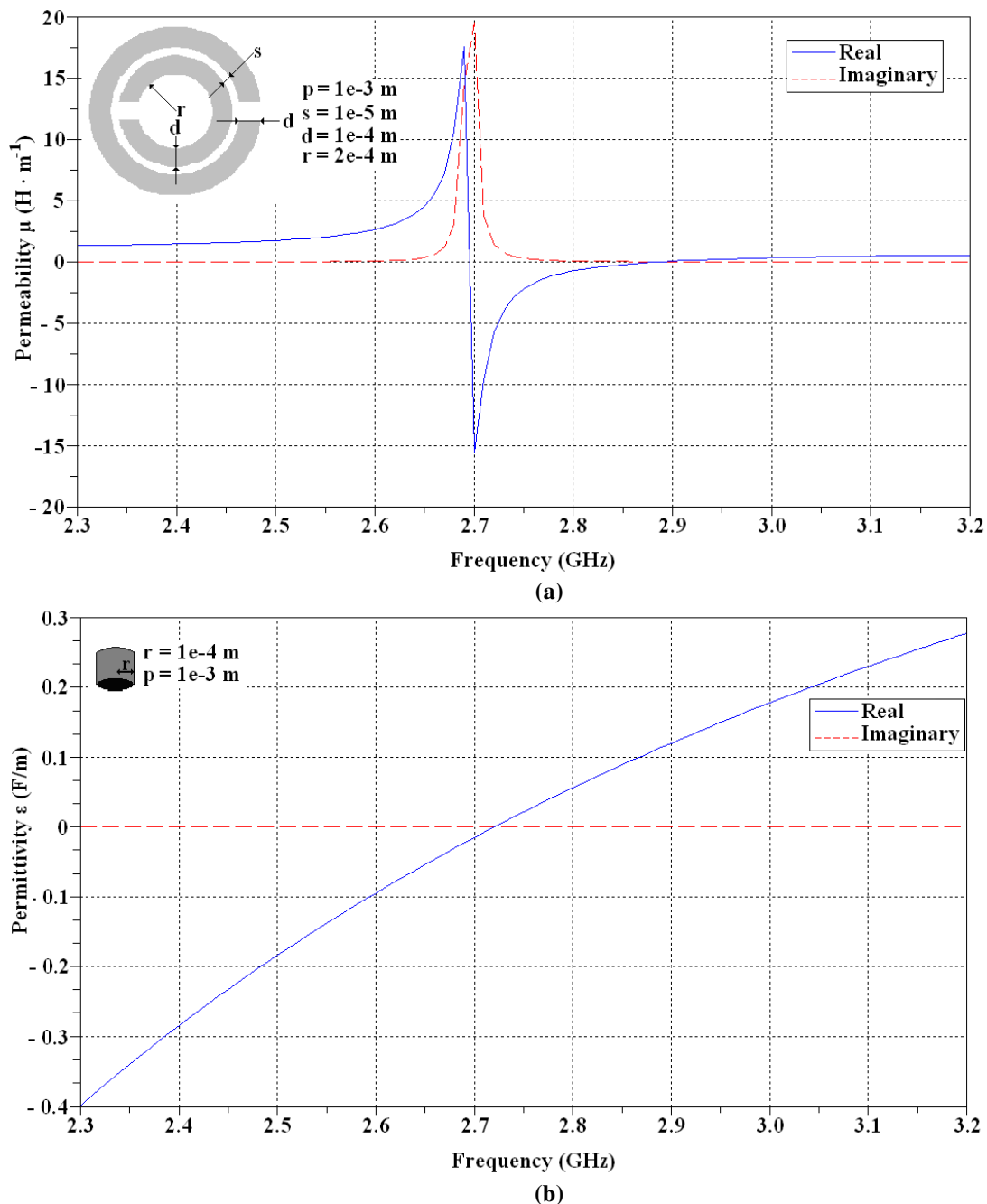
Fig. 2.9 – Theoretical results for: (a) permittivity using a SRR and (b) permeability using a thin wire.

2.4 Bianisotropic Media

Considering the Maxwell's theory of macroscopic electromagnetism, material media are described phenomenologically by constitutive relations. Depending on the particular form of the constitutive relations, a medium can be characterized as linear or nonlinear; conducting or non-conducting; dispersive or non-dispersive; homogeneous or inhomogeneous; isotropic, anisotropic, or bianisotropic. An isotropic medium is characterized by a scalar permittivity that relates $\vec{D}$ to $\vec{E}$, and by a permeability that relates $\vec{H}$ to $\vec{B}$. In an anisotropic medium, either or both of the permittivity and the permeability can assume the form of a three-dimensional tensor. The constitutive relations of a bianisotropic medium relates $\vec{D}$ to both $\vec{E}$ and $\vec{B}$, and $\vec{H}$ to both $\vec{E}$ and $\vec{B}$. Similarly to the anisotropic case, their relationships are provided by three-dimensional tensors [16]. When all four tensors become scalar quantities, the medium may be called bi-isotropic. Just like an isotropic medium or an anisotropic medium, which provides a phenomenological description of many physical media, a bianisotropic medium can also be realized by a large class of material [16].

A generalization of this phenomenon is the bianisotropic which is associated with the simultaneous presence of both anisotropic and magnetoelectric behavior, e.g. particles chiral and omega shown in Fig. 210. The insulation behavior can not be described in terms of permittivity and permeability due to the electromagnetic coupling effects between the sets of inclusions that affect their performance, as a result the electric field not only induces electric polarization, but also magnetic. The same is true for the magnetic field, materials that have this characteristic are called bianisotropic [1].
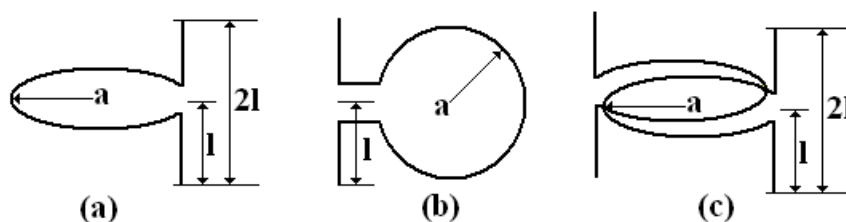
Fig. 2.10 – Bianisotropic particles: (a) chiral, (b) omega, and (c) double chiral.

The bianisotropic medium is the most general type of material that can be described in terms of normal material parameters. They have been used in many applications, such as the design of radar absorbing materials for stealth technology and polarization transformers.

These bianisotropic materials are anisotropic and can be characterized by uniaxial permittivity and permeability tensors [18].

$$\bar{\bar{\varepsilon}} = \varepsilon_0 \begin{pmatrix} \varepsilon_{xx} & 0 & 0 \\ 0 & \varepsilon_{yy} & 0 \\ 0 & 0 & \varepsilon_{zz} \end{pmatrix} \tag{2.32}$$

$$\bar{\bar{\mu}} = \mu_0 \begin{pmatrix} \mu_{xx} & 0 & 0 \\ 0 & \mu_{yy} & 0 \\ 0 & 0 & \mu_{zz} \end{pmatrix} \tag{2.33}$$

2.4.1 Double-Negative and Indefinite Media

A material will be denoted throughout as a double positive (DPS) medium if its relative permittivity $\varepsilon_r = \varepsilon/\varepsilon_0$ and permeability $\mu_r = \mu/\mu_0$ are both positive. On the other hand, the relative permittivity and permeability are both negative in a double negative (DNG) medium [6].

The DNG media, materials with both negative permittivity and permeability, have become almost synonymous with metamaterials. One way to build a uniaxial DNG is to use the structure described in Fig. 2.7c that was suggested by Pendry [13]. This structure can be seen in Fig. 2.11 in three-dimensional form, where the arrangement of wires allows the realization of negative permittivity and the network of SRR the negative permeability.
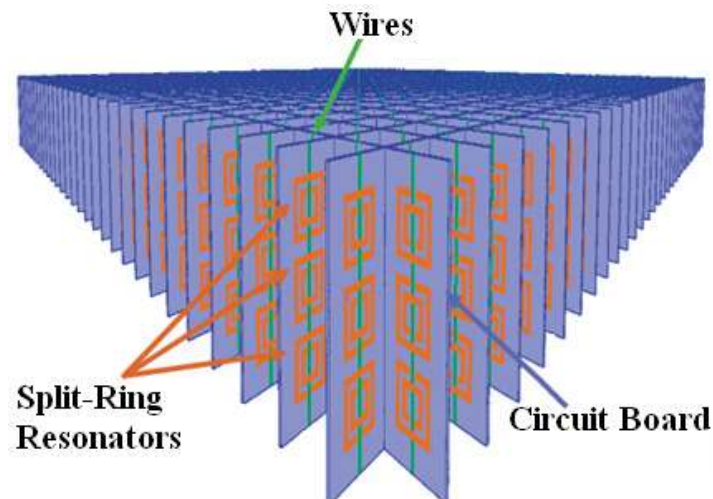
Fig. 2.11 – Realization of DNG material at microwave frequencies.

2.4.2 Photonic and Electromagnetic Band Gaps

The electromagnetic crystals, or photonic crystals, when operating at optical frequencies are often termed electromagnetic band-gap (EBG) or photonic band-gap (PBG) materials. These crystals are structures composed of electromagnetic periodic dielectric or metallo-dielectric, operating at wavelengths that are comparable to the period, and one of its characteristics is that they have passbands and stopbands, which affect the propagation of electromagnetic waves [1].

Basically, these crystals contain regularly repeating internal regions of high and low dielectric constant. Electrons or photons behaving as waves, propagate, or not, through this structure depending on their wavelength. Wavelengths that are allowed to travel are known as modes, and groups of allowed modes form bands. Disallowed bands of wavelengths are called electromagnetic or photonic band gaps.

Moreover, these PBG or EBG occur in natural biological systems, for example the color generating nanoarchitectures in the cover scales of the Morpho butterflies that use multiple layers of cuticle and air to produce striking blue color, as shown in Fig. 2.12.

Courtesy of Prof. Dr. Dacio Rocha Brito from Uneal

Fig. 2.12 – The blue-green color on several species of butterflies is caused by the nanoscale structure of the insects' wings.

The first studies and demonstration of a photonic crystal with a complete bandgap, see Fig. 2.13, were carried out in the early 1990s [19]. Since then, photonic and electromagnetic crystals have found numerous applications in FSSs and as components for waveguide and resonators, both in optical and microwave regimes.
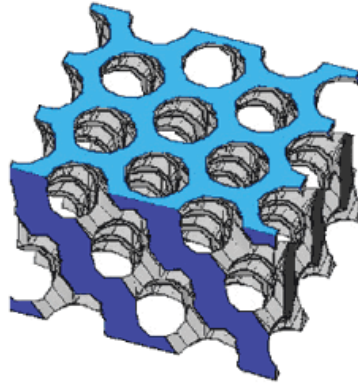
Fig. 2.13 – The first photonic crystal with a complete band gap [19].

Electromagnetic crystals are also classified as electromagnetic bandgap structures and high-impedance surfaces at microwave frequencies. Some practical applications of EBGs include antenna beam narrowing and shaping using Fabry-Perot like EBG cavity [20], mobile antenna efficiency improvement using Mushroom-like EBGs [21] amongst others. Typical HISs are thin composite layers with reflection coefficient +1, and hence, the HIS behaves as though it were a magnetic conductor. For this reason, HIS's are also referred to as artificial magnetic conductors (AMCs). An example of a HIS application is shown in Fig. 2.14 from [22]. In this application a bowtie wideband antenna is place above a HIS substrate.
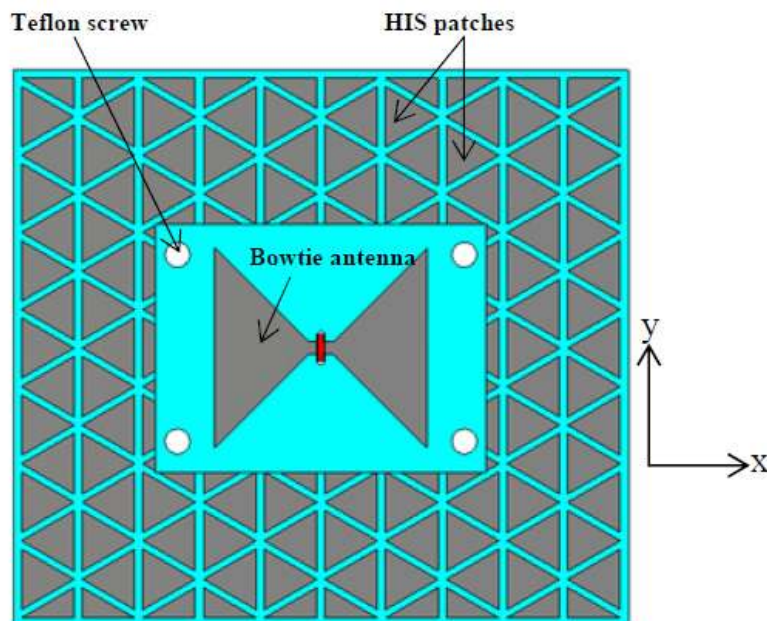
Fig. 2.14 – Ultra wideband Bowtie antenna with HIS substrate.

2.5 Summary

In this chapter a detailed discussion about the theoretical background of metamaterials was presented. We provided theoretical information about the components of a left-handed material, negative permittivity and negative permeability structures. We also showed that the simultaneous negative values for permittivity and permeability results in negative refraction. In this review we have stressed the novelty of electromagnetic metamaterials and shown the great flexibility that we now have to design materials with the power to control electromagnetic radiation.

Chapter 3

Frequency Selective Surfaces

This section provides the necessary Frequency Selective Surface (FSS) knowledge to understand and design these structures. The theory governing the use of FSSs have evolved directly from the diffraction grating used in optics. David Rittenhouse discovered the filtering properties of a frequency selective surface in 1786 [23], He noted that some colors of a light spectrum are suppressed when he observed a lamp through a silk scarf. Due to the simplicity of the filtering process achieved by these structures, they are used in many areas of engineering. This simplicity is the reason why the FSSs receive great attention in many areas of electromagnetic centuries after Rittenhouse discovery.

Frequency Selective surfaces are planar periodic structures that behave like inductance and capacitance towards incident waves and hence behave as spatial filters to electromagnetic energy. The surface is assembled with identical patch or aperture conducting elements repeating periodically in either a one or two-dimensional array [24-26]. Frequency selective surfaces can be fabricated as planar 2-dimensional periodic arrays of metallic elements with specific geometrical shapes, or can be periodic apertures in a metallic screen. The transmission and reflection coefficients for these surfaces are dependent on the frequency of operation and may also depend on the polarization and the angle of incidence. The versatility of these structures are shown when having frequency bands at which a given FSS is completely opaque (stop-bands) and other bands at which the same surface allows wave transmission [24].

In optics spatial filter is a beam converging device coupled with a filter that uses the principles of Fourier optics to alter the structure of a beam of coherent light or other electromagnetic radiation. The filter, is used to remove interference patterns in a in the out put of a laser beam. In spatial filtering, a lens is used to focus the beam. Because of diffraction, a beam that is not a perfect plane wave will not focus to a single spot, but rather will produce a

pattern of light and dark regions in the focal plane. The interference is removed from the beam in the following manner the laser output appears as a point source at infinity and the interference producing sources are at finite distance from the filter, due to the difference in the point of origin, focusing the beam will produce an image of the source with all the interference defocused in an annulus around the focused beam at the filter. The focused beam will pass through the filter and the interference will be severely attenuated.

To understand the concept of spatial filtering, consider an incident wave striking a metal surface as shown in Fig. 3.1. Imagine a single electron in the surface plane with a direction vector perpendicular to the plane. The E-vector of the incident wave is parallel to the metallic surface. Therefore, when the incident wave strikes the metal surface, it exerts a force on the electron causing it to accelerate in the direction of E-vector. In order to keep the electron in a continuous oscillating state, some portion of energy must therefore be converted into the kinetic energy of the electron. This will result in the absorption of most of the incident energy by the electron and its reflection by the electron aceleration (Low Transmittance). The transmission through the filter will be zero if all the energy of incident wave is converted to the kinetic energy for the electron.
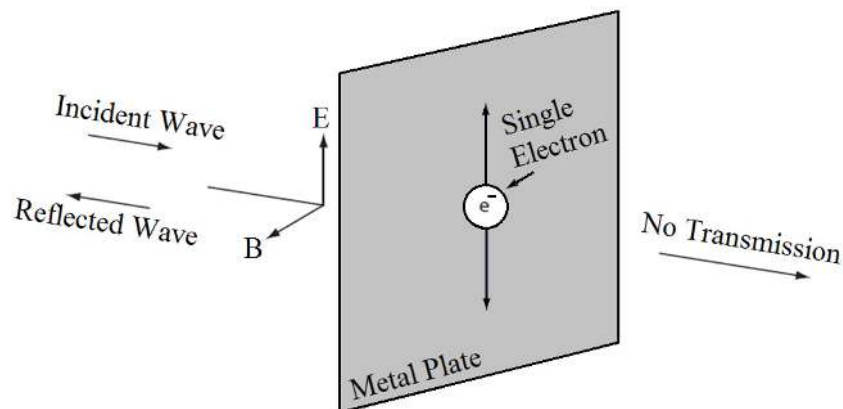
3.1 – Electron in the plane oscillates due to the force exerted by incident wave resulting in low transmittance.
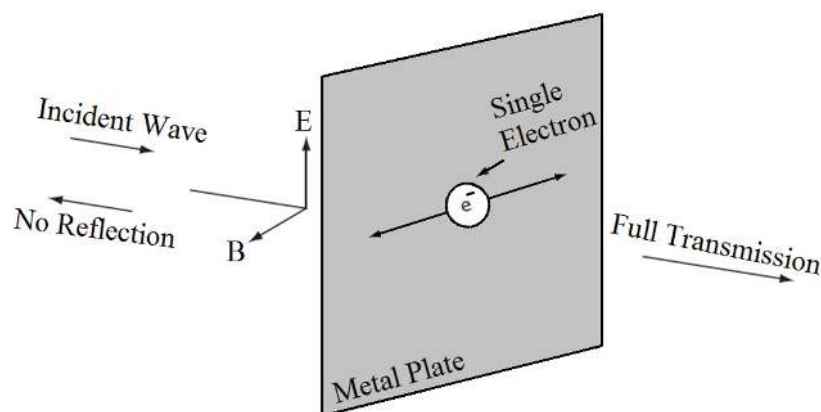
3.2 – Electron is constrained to move and hence unable to absorb energy resulting in high transmittance.

Referring to Fig. 3.2, in which the direction vector of the electron is perpendicular to the E-vector of incident wave. In this case, despite of force exerted by the E-vector, the electron is constrained to move along the direction vector. Hence the electron is unable to absorb the kinetic energy of incident wave. Therefore, the wave is not absorbed and a high transmittance occurs.

3.1 FSS Elements

A periodic surface is basically a set of identical elements arranged in a two-dimensional or infinite arrays. Considering the structure shown in Fig. 3.3. The incident field $\vec{E}^i$ is given by [25],

$$\vec{E}^i = \vec{u}e^{-jkz}, \qquad \text{for} \qquad z < 0 \qquad (3.1)$$

where the time factor exp $(+j\omega t)$ has been suppressed, and $k = 2\pi/\lambda = \omega/c$ is the wave number. The unitary vector $\vec{u}$ satisfies the relation $\vec{u} \cdot \vec{u}^* = 1$ and $\vec{u} \cdot \vec{z} = 0$. It defines the polarization of the incident field, e.g., $\vec{u} = \hat{x}$ for a linearly polarized field, and $\vec{u} = (x \pm jy)/\sqrt{2}$ for a circularly polarized field [25].
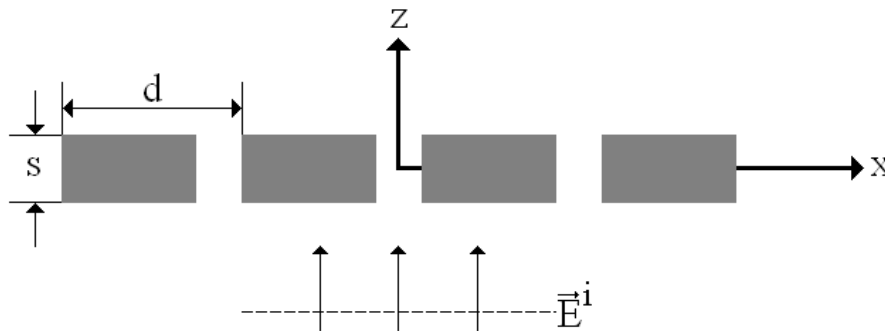
Fig. 3.3 – Metal screen irradiated by a normally incident plane wave [1].

This frequency selective property described by Rittenhouse proved the fact that surfaces can exhibit different transmission properties for different frequencies of incident wave. Hence, such surfaces are now called frequency selective surfaces (FSSs). As mentioned before an FSS can be considered as a free-space filter, which could be used to pass certain

frequencies and stop others. Therefore, an FSS either blocks or passes waves of certain frequencies in free space [27]. A FSS comprises a bi-dimensional periodic array of elements patches or apertures in a conducting screen, which must be either freestanding or etched on supporting dielectric substrates. Based on the element geometry, FSSs can be classified into two categories as shown in Fig. 3.4 [24].

Fig. 3.4 – Basic FSS geometries: The patch-array produces a capacitive response, whereas the array of slots is inductive.

The main difference between this two cases is that we excite electric currents on the squares while we excite "magnetic currents" in the slot square case (i.e., there is a voltage distribution in the slots). The two cases become quite similar and symmetric if we compare the electric field in the square case and the magnetic field in the slot square case. Following this principle a Frequency Selective Surface is a periodic array of either radiating or non-radiating elements or slots, which effectively act as a band stop or band, pass filter respectively to electromagnetic waves. There are a wide variety of possible elements, which can be used to realize FSS arrays.

3.2 Different FSS Element Types

As mentioned before FSSs can be seen as electromagnetic filters that are normally realized using periodic structures formed by arrays of conducting elements on a dielectric substrate or by periodic aperture elements in a conducting sheet.

The basic types of frequency selective surfaces elements are: center linked or N-pole, type of loop, interior solid or plate type and combinations of the others elements. Fig. 3.6 shows examples of FSSs elements [25].
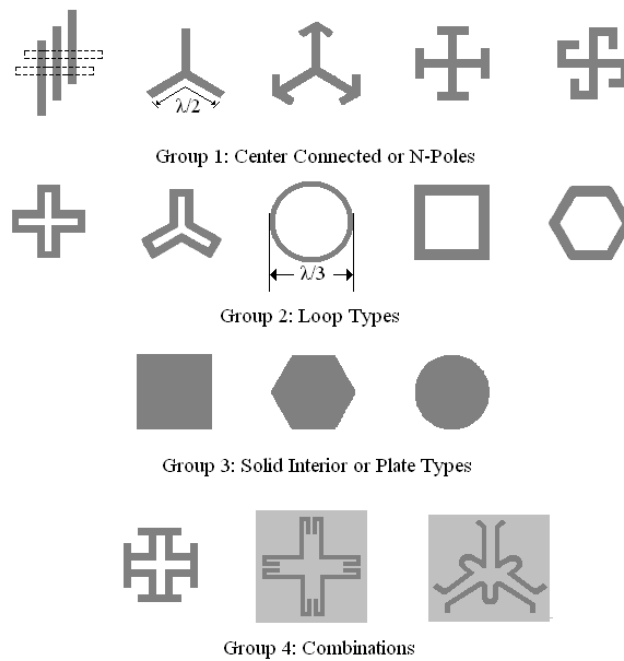
Fig 3.5 – The four major groups of FSS elements. These elements may be used to construct band stop filter type FSS arrays. Elements are ordered from most narrowbanded on the left to most wide-banded on the right [25].

3.2.1 Infinite FSS Arrays

Considering the periodicity a true frequency selective surface is infinite. Thus, the concept of starting to discuss the properties of infinite arrays and apply that knowledge for a finite array design as in practice [24].

3.2.2 Finite FSS Array

Although only finite ones can be fabricated, the infinite FSS periodical structures are useful to identify many of its properties. Two main considerations must be made in the design of a finite array, i.e., edge diffraction and surface waves radiating. The edge diffraction causes the stopband bandwidth to rise. Surface waves appear about 20-30 per cent below the resonance, when the spacing between elements is less than 0.5λ [25]. Surface waves can be a problem when using FSSs.

The electromagnetic band-gap structures have been employed in different to reduce the effects of surface wave. An example is the use of a high impedance surface, a

metamaterial with dispersive permeability on top of a FSS array. The HIS has a high-impedance frequency regime and the surface wave suppression in the high impedance band gap is a consequence of the FSS connected to its ground plane using a metallic via.

3.3 Metamaterial FSSs

The most common FSSs types take the form of planar, periodic metal or dielectric arrays in 2D space. Frequency behavior of an FSS is determined by the geometry of the surface unit cell provided that the surface size is infinite. As mentioned before FSSs were originally introduced as spatial filters and since that they have been employed in a variety of other applications including most recently metamaterial applications.

Metamaterial frequency selective surfaces can be used in designing reactive impedance surfaces in a form of an artificial magnetic conductor (AMC) and electromagnetic band-gap (EBG). The FSS are an alternative to fixed frequency metamaterial where static geometry and spacing of unit cells to determine its frequency response. FSSs have reflective characteristics with a certain phase and amplitude that allow frequency changes in a single medium and are not restricted to a fixed frequency response.

The classic example of AMC is the high impedance surface described in [33]. This high impedance surface is a periodic array printed in a dielectric substrate where each element of the array is connected to the ground plane. This array is called mushroom. In a normal electric conductor electric current flow is allowed, in an AMC currents will not be allowed to travel through the medium, which in turn bans the propagation of surface waves inside the substrate.

This metamaterial FSS will be used as a ground plane for antennas in order to effectively suppress undesirable wave fluctuations, i.e., surface waves inside the substrate, while producing good radiation patterns. The type of high impedance surface used in this work is show in Fig. 3.6. The square metal patches are raised above the surface, and points at the center are the vias of vertical connection.
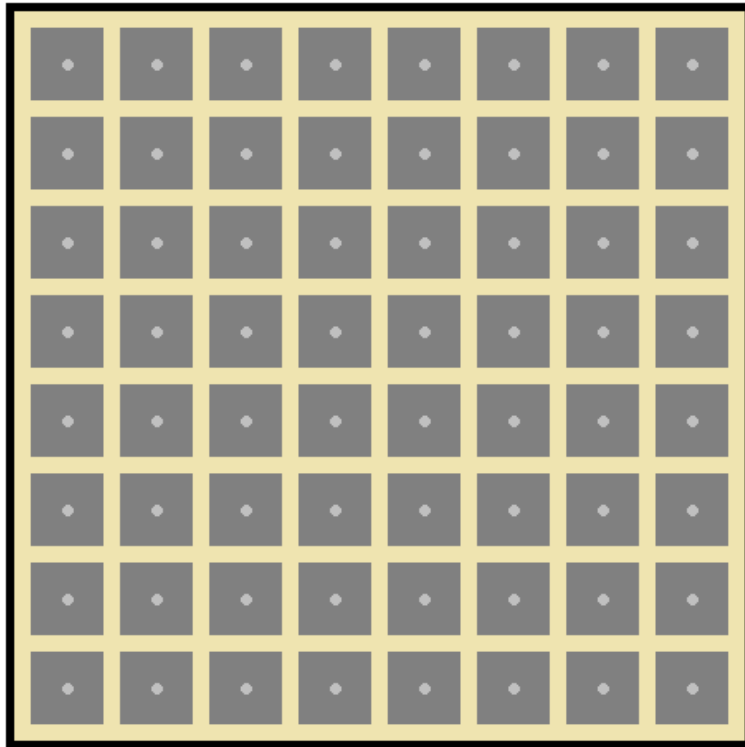
Fig. 3.6 – Superior view of a high impedance surface, patches connected to the ground plane with metal cylinders.

An AMC can be seen as a surface with increased surface impedance. Ideally the transverse wave impedance at the surface is infinite (for an incident plane). The transverse impedance is defined as the ratio of the transverse electric field over the transverse magnetic field, E_t/H_t. In this case an infinite impedance corresponds to $H_t \approx 0$, meaning that the surface cannot bear a tangential magnetic field and hence the name magnetic conductor. The AMC properties can the explained by the transmission line theory. Considering a $\lambda=4$ impedance inverter, a short impedance is transformed to an open impedance. This idea is used in design of corrugated surfaces behaving as an open circuit in terms of wave impedance, Fig. 3.7.
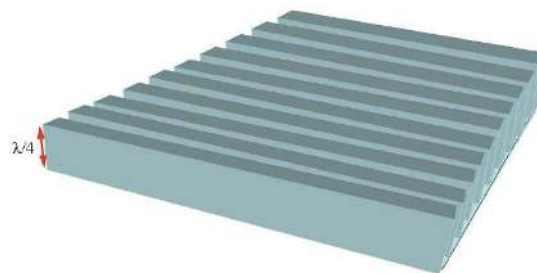
Fig. 3.7 – A corrugated reactive surface acting as an AMC.

The HIS can be viewed as a network of parallel LC resonant circuits, which acts as a 2D electric filter to block the flow of currents and consequently suppresses the surface waves along the sheet. When the patches are connected to the ground plane its impedance changes and the surface waves properties are altered. The HIS equivalent LC circuit from [33] is shown in Fig. 3.8. The capacitance occurs due to the proximity of the top metal patches, while the inductance originates from current loops within the structure. In the LC resonance frequency the surface impedance is high and an electromagnetic band gap is formed so waves are not bound to the surface and the radiate into surrounding areas.
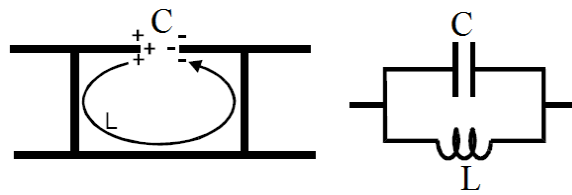
Fig. 3.8 – Origin of the equivalent circuit elements left and equivalent circuit model for the high-impedance surface right [33].

3.4 Antenna Bandwidth Augmentation

Frequency selective surfaces can be used as a superstrate to enhance the performance of a number of antennas [34-36]. These superstrates offer the advantage of ease of fabrication with microstrip technology and reduced thickness as compared with those of the dielectric type superstrates. The FSS can suppress its grating lobes and as a result a high gain antenna can be obtained.

Another way to achieve a broader bandwidth is the use of a Fabry-Pérot (FP) [37-42] configuration. Antenna applications that require high directivity need the use of array designs with complex feed network to comply with the directivity specifications using conventional technology. A FP configuration uses a single radiating element instead of a array that can simplify considerably the complexity of receivers and transmitters, reducing the size and the mass of the conventional configurations. The FP medium consists of a capacitive-type frequency selective surface array that is used as superstrate and an artificial magnetic conductor as ground plane. The realized gain and the bandwidth of the antenna can be simultaneously improved by using the tapered artificial magnetic conductor. As a result the

maximum gain is increased and the bandwidth is improved when compared to the single uniform antenna. In Chapter 6 this phenomenon will be described.

3.5 Summary

This chapter has presented a historic background and a review of literature on FSSs. Particular emphasis has been placed on factors, which influence the FSS response, including the element geometry, the element conductivities, the dielectric loading, and the signal incident angles. Studies have indicated that the fundamental frequency characteristics of an FSS are mainly governed by the element geometry, including element dimensions and shapes. With a proper choice of element dimensions and shapes, an FSS could, to some extent, be insensitive to incident angles and signal polarizations. Some metamaterial like FSSs were also described.

Chapter 4

Microstrip Antennas and Filters with CSRR Parasitic Structures

Interference is a big issue for UWB communication systems. Since the UWB spectrum is so large (3.1-10.6 GHz) the entire U-NII (Unlicensed National Information Infrastructure) band (5.15-5.825 GHz) overlaps with its spectrum. Fig. 4.1 shows the U-NII spectrum inserted in the UWB spectrum. As UWB transmitters must not cause electromagnetic interference on any nearby communication systems, a solution to notch this band is needed. In this chapter two solutions to archive a band notched function are presented.
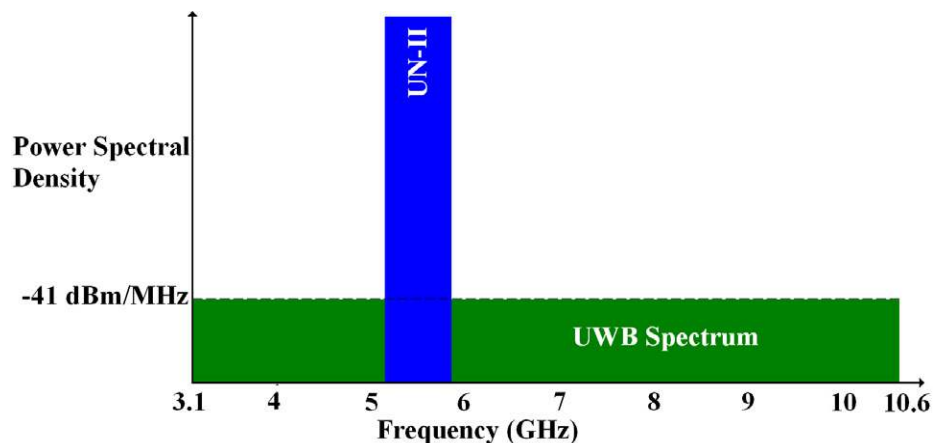
Fig. 4.1 – Ultra wideband and UN-II spectrums.

As a first solution, a parasite metamaterial structure is inserted directly in the antennas patch. Many UWB antennas designers have been working on several alternative solutions to achieve band rejected function. Some of the approaches proposed in literature are embedding

slots (arc-slot) [43], double U-slots [44], stubs or spurlines [45], square-slot [46], V-slot [47], and attaching bar [48]. In these classical solutions the band-notched characteristic comes with many problems mainly due to the difficulty in controlling the band-notch width in a limited space. Some designs occupy wider band-notch (more than 2 GHz) or have only single band-notched characteristic. The solution proposed in this work to block this band was found by introducing a metamaterials SRR structure in the antenna's patch for notching the entire U-NII band. As mentioned before, a SRR is a pair of concentric annular rings splited at opposite ends. There are two types of SRR: one were the rings are made of metal like copper and the other is a slot-type SRR where the rings are slots on a nonmagnetic metal, which are etched in the foursquare patch. These structures are also called Complementary Split Ring Resonator (CSRR) where both rings have small gap between them. Different from classical solutions the band-notch of the CSRR can be easily tunable by changing is dimensions and also have a tunable dual band-notched characteristic.

The second solution is a microstrip UWB filter with the same goal as the first solution, i.e., notch the UN-II band. There are many classical methods for designing such filters some examples are the stepped-impedance resonator (SIR) [49], the spurline [50], and the defect ground-structure [50]. The filter solutions proposed in this work consist of a simple microstrip line backed by the CSRR placed on its ground plane. This structure present, many advantages like a tunable band-notch by simple changing its physical dimensions, band-notch augmentation by increasing the number of CSRRs in the ground plane and easy design and fabrication when compared to some classic solutions

The CSRR-based medium has the property of negative effective permittivity and can be used to reject unwanted frequency band. Due to the relatively high insertion loss for CSRR slots, the CSRR has a band-stop filtering property. Moreover, the band-notched frequencies can be varied by adjusting the length of C-shaped slot and the dimensions of CSRR independently. Simulated and measured results of the proposed prototypes are provided.

4.1 – Ultra Wideband Monopole Antenna with Split Ring Resonator as Filter

In the last years a special attention has been devoted to the development of Ultra Wideband (UWB) monopole antennas [51 - 53]. The UWB is a short-range wireless technology for transmitting large amounts of data at very high-speed with very low power,

generally the effective isotropic radiated power (EIRP) is -41.3 dBm/MHz. The bandwidth of the UWB signal is at least 25% of the center frequency, and the unlicensed use of UWB is in the range of 3.1 to 10.6 GHz [54]. The use of UWB systems needs efficient antennas to provide acceptable bandwidth requirements, and radiation pattern characteristics throughout the designated UWB spectrum. It is generally accepted that for antennas to be classified as ultra-wideband, the requirement will be to satisfy minimum fractional bandwidths of at least 20 % or 500 MHz or more [55].

There are many theories to explain the operation of UWB antennas. In the 1950s Rumsey's principle [56] was introduced to explain a family of that he called frequency-independent antennas. This principle suggests that the impedance and pattern properties of an antenna will be frequency independent if the antenna shape is specified only in terms of angles. To satisfy the equal-angle requirement, the antenna configuration needs to be infinite in principle, but is usually truncated in size in practice. This requirement makes frequency-independent antennas quite large in terms of wavelength. It has been verified that for spiral antennas, conic spiral antennas and some log-periodic antennas the principle can be applied.

The Rumsey's principle was, probably, inspired by Mushiake and Uda work in the 1940s on the constant independent of self-complementary antennas for all frequencies, half the intrinsic impedance of free space [57], which were invented by Runge in the 1930s [58]. They discovered that the product of input impedances of a planar electric current antenna (plate) and its corresponding 'magnetic current' antenna (slot) was a real constant. Therefore, an antenna built in a complementary structure of electric and magnetic currents exhibits a real constant impedance. This theory, referred as 'Mushiake's relation', has led to the development of a large family of self-complementary antennas with constant input impedance. Mushiake's relation has relaxed the condition for achieving ultra wide impedance bandwidth. However, it doesn't guarantee constant radiation patterns over the operation bandwidth [55]. Incidentally, an infinitely long biconic antenna was also demonstrated to exhibit constant impedance, although it is not a self-complementary structure.

Lately, many researchers have started to look into UWB with the development of the latest communication systems, and a surge of research interest into small UWB antennas has been raised. Such antennas have to be small enough to be compatible to the UWB unit and omnidirectional radiation patterns are often required for UWB terminal antennas. Finally, a good time-domain characteristic, i.e., a good impulse response with minimal distortion is also required for transmitting and receiving antennas. For these tasks two families of compact antennas have emerged to provide solutions. The first family is originated from biconal

antennas, but in a compact planar configuration, such as bowtie, diamond, circular and elliptical disc dipoles. They provide UWB characteristics and also satisfy other requirements imposed by commercial UWB systems. The second family is due to further developments on broadband monopole antennas, in which planar elements, such as circular, square, elliptical, pentagonal and hexagonal discs appear.

For this investigation, a circular monopole antenna was chosen as a starting point. A monopole antenna is a type of radio antenna formed by replacing one half of a dipole antenna with a ground plane at right angles to the remaining half. If the ground plane is large enough, the monopole behaves like a dipole, as the reflection in the ground plane behave as the missing half of the dipole, except that the radiation from the reflected half is added to that of the real half (see image antenna). However, a monopole will have a directive gain of 5.19 dB (gain is twice, 3 dB over) that for a half-wave dipole antenna, and a lower input resistance [50]. In general, these antennas are built into microstrip structures with limited ground plane, in the microstrip monopole form. For this reason, they have small dimensions and weight, and easy construction, which are some of its main advantages. The geometry of the antenna considered as a starting point is shown in Fig. 4.2 [65].
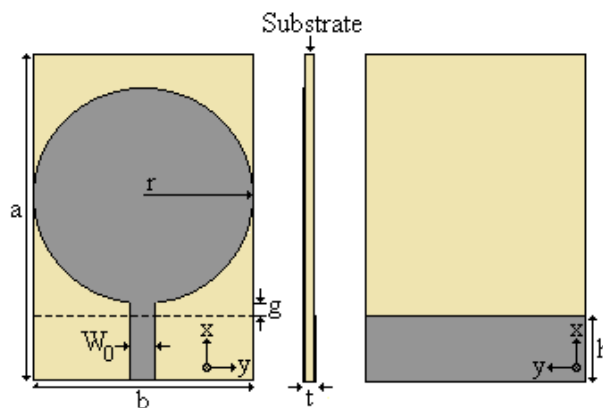
Fig. 4.2 – Circular microstrip monopole antenna, the gray region denotes a conductor material.

The self-resonant antenna consists of a circular monopole disc with a radius "r" and is fed by a 50Ω microstrip line, printed on a dielectric substrate with dimensions "a-b" and thickness "t", backed by a ground plane of height "h". The feeding line width is represented by W_0 and "g" is the gap between the disc and the ground plane. The structure shown above was considered to start the experimental research implementation, performed with the construction and measurement, while the Computer Simulation Technology: Microwave Studio (CST MWS[TM]) was used as an auxiliary tool in the simulation process. The simulated

S11 return loss and Smith Chart results for this monopole antenna are shown in Fig. 4.3. In the computer aid simulation an Arlon DiClad 880^{TM} substrate with coppered plates on both sides was used. The thickness of the dielectric layer, "t" is 0.768 mm, the inherent dissipation of electromagnetic energy (dielectric loss tangent) is 0.0009, the permeability is 1, and the permittivity ε_r is 2.17. Once the antenna was adapted the following dimensions were determined (see Fig. 5.1) a = 30 mm, b = 20 mm, r = 10 mm, h = 6 mm, g = 1 mm, W_0 = 2.4 mm.
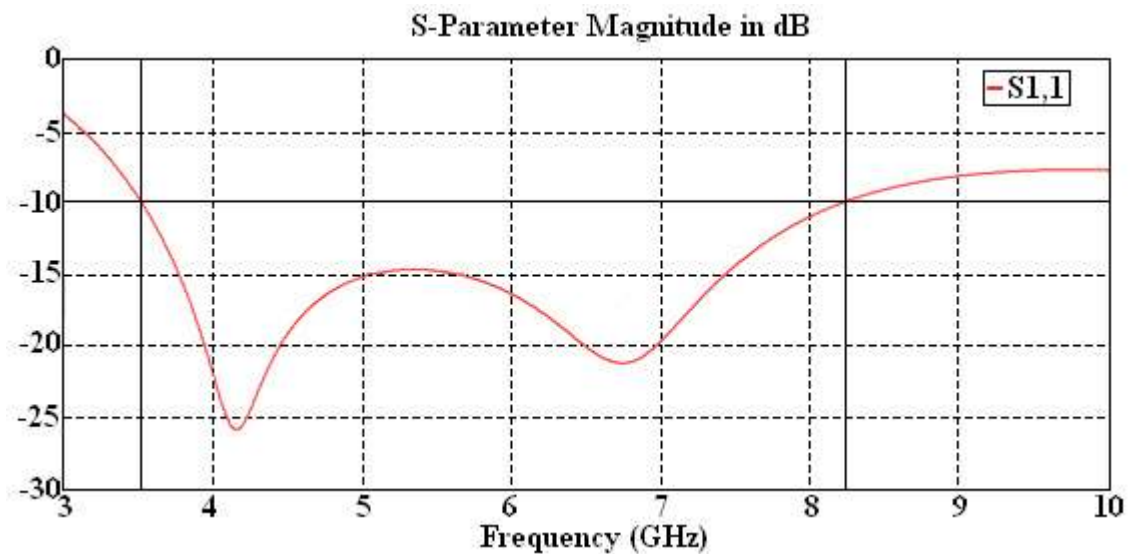
(a)
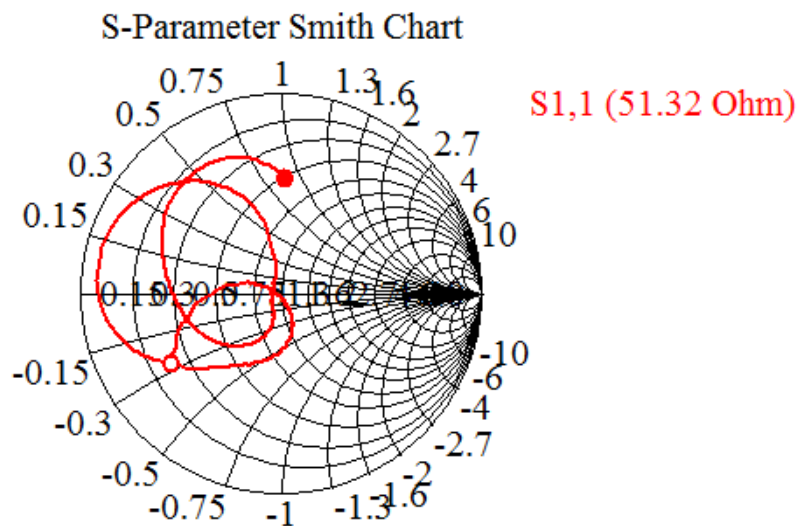
(b)

Fig. 4.3 – (a) Return loss and (b) Smith Chart results for the microstrip circular monopole antenna.

The bandwidth is recommended to guarantee an S11 of –10dB over the frequency band of interest and Fig. 4.3 (a) show that the antenna has a large bandwidth, i.e. the S11 is below −10 dB in the extension from 3.7 GHz to 8.2 GHz. The antenna has also a good matching to the 50Ω microstrip line. To optimize the antenna for a bandwidth augmentation the ground plane is truncated with a rectangular cut introduction of width "l", which consists in reducing the capacitance in the microstrip line connection region with the circular conductor patch, to improve the impedance matching. Fig. 4.4 shows the improved design.
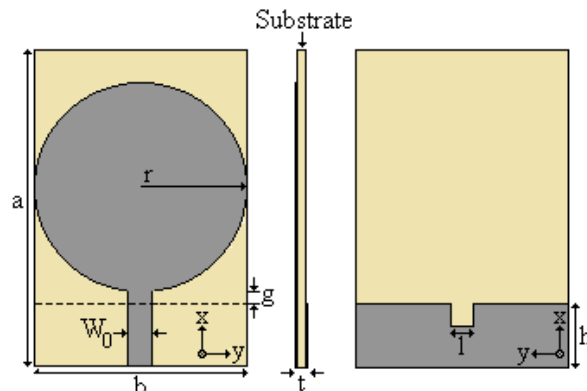
Fig. 4.4 – Circular microstrip monopole antenna with improved ground plane, where the gray region denotes a conductor material.

The return loss for the improved antenna is shown in Fig. 4.5. The new design has the same dimensions as the first one and the rectangular cut has the width l = 2.4 mm which is equal to the microstrip feeding line W_0. It can be seen that with the rectangular cut introduction the bandwidth is increased by about 17%, in the improved bandwidth the S11 is below −10 dB form 3.8 GHz to 8.9 GHz.
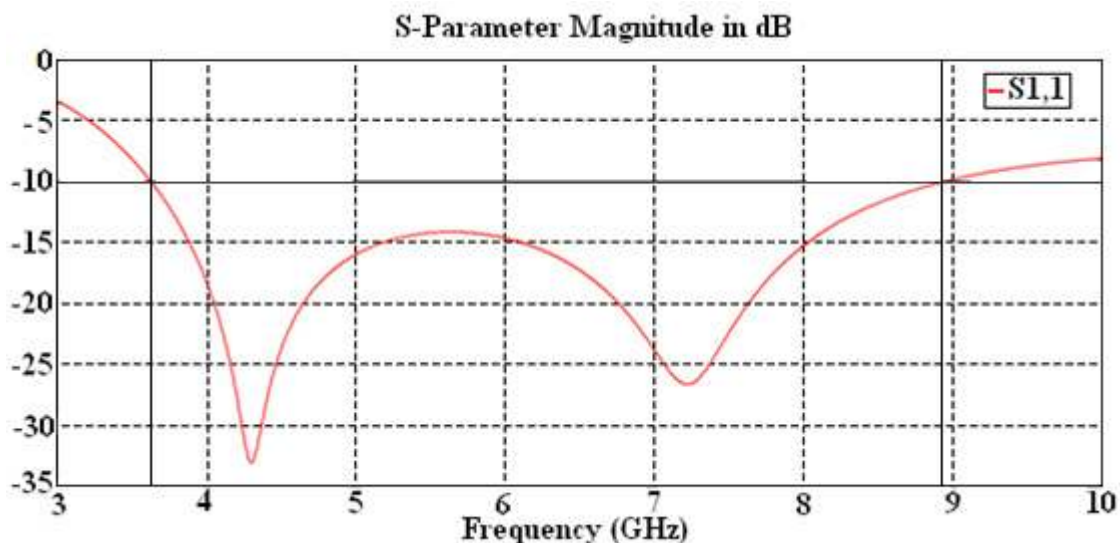
Fig. 4.5 – Return loss for the improved microstrip circular monopole antenna.

Based on the obtained results it can be said that, according to the antenna theory [59], the maximum available power W_m of a receiving antenna for a matched load is proportional to the product of λ^2, $|E|^2$, and D.

W_m: Maximum available power of receiving antenna with a matched load.

λ: Wavelength.

E: Electric field.

D : Directivity (Directive gain) of the receiving antenna.

The received power "W_m" decreases to smaller values with increasing frequencies in inverse proportion to the square of the frequency when its directivity "D" remains unchanged [60]. The term frequency-independent is reserved for antennas that have no theoretical limitation on the bandwidth of operation. Such a property is really unimaginable from its nomenclature. In Practicte, however, the performance cannot be even approximately constant for all frequencies. There are physical bounds that limit the band over which the performance can be held almost constant. Between the band limits the performance varies in a manner that is periodic with the logarithm of the frequency. The monopole antenna describe in this section exhibits decreasing resonant frequency independent of its geometric shape

4.1.1 – Complementary Split Ring Resonator Structure

The SRR was first introduced in [61] as a new method for the design of metamaterials structures. If the excitation magnetic field $\vec{H}$ is perpendicular to the plane of the rings$(\vec{H} \perp \hat{y})$, so as to induce resonating currents in the loop and generate equivalent magnetic dipole moments. This metamaterial exhibits a plasmonic-type permeability frequency function that in the lossless case it appears that [61],

$$\mu_r < 0 \qquad\qquad\qquad\qquad (4.1)$$

This investigation was carried out considering a CSRR structure and its stop band characteristics. A SRR can be mainly considered as a resonant magnetic dipole, with very high Q, that can be excited by an axial magnetic field, while the CSRR essentially behaves as an electric dipole (with the same frequency of resonance) that can be excited by an axial electric field [62]. As mentioned in Chapter 2 the SRRs behave as an LC resonator that can be excited by an external magnetic flux, exhibiting a strong diamagnetism above their first

resonance. The SRRs also exhibit cross-polarization effects, so that excitation by a properly polarized time-varying external electric field is also possible. The basic topology and the equivalent circuit of a SRR and a CSRR are shown in Fig. 4.6 [62].
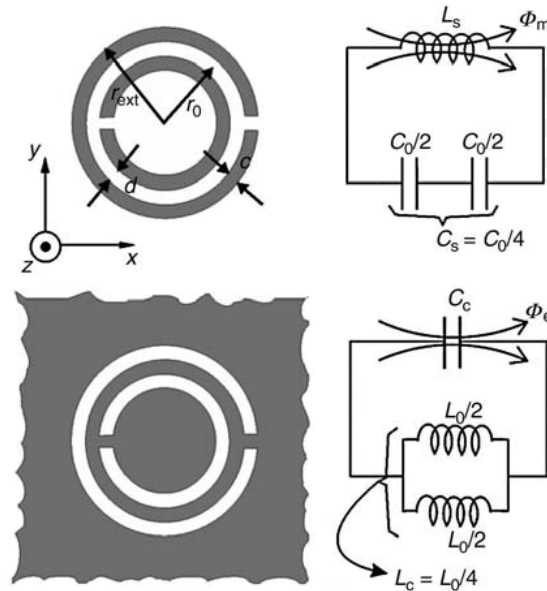
Fig. 4.6 – Geometries and equivalent circuit of a SRR and a CSRR, where the gray region denotes a conductor material.

In this diagram, C_0 indicates the total capacitance between the rings, that is $C_0 = 2\pi r_0 C_{pul}$, where C_{pul} is the per-unit-length edge capacitance. The CSRR-based medium exhibits the property of a negative effective permeability, introduced by these new elements, electrically coupled to the host transmission line and can be used to reject unwanted frequencies in the designed UWB antenna. In contrast to the usual half-wavelength resonators, the dimensions of the CSRR are typically one-tenth of the guided wavelength or less at the resonant frequency [61]. The complementary Split Ring Resonator can create the strongest resonance when parallel polarization occurs, where the parallel polarization means that the $\vec{E}$-field is aligned parallel with the x–y plane and the $\vec{H}$-field is aligned with the center axis z of the CSRR.

4.1.2 – Simulation and Experimental Results

The monopole antenna with the slot-type SRR consist of a conductor patch, with circular form, printed on a dielectric material, which is mounted on a ground plane. Once the

CSRR resonance frequency was determined the following dimensions where obtained r_2 = 3.3 mm, r_1 = 2.4 mm, d_1 = d_2 = 0.5 mm, s = 0.4 mm and g_1 = g_2 = 1.2 mm (see Fig. 4.7).
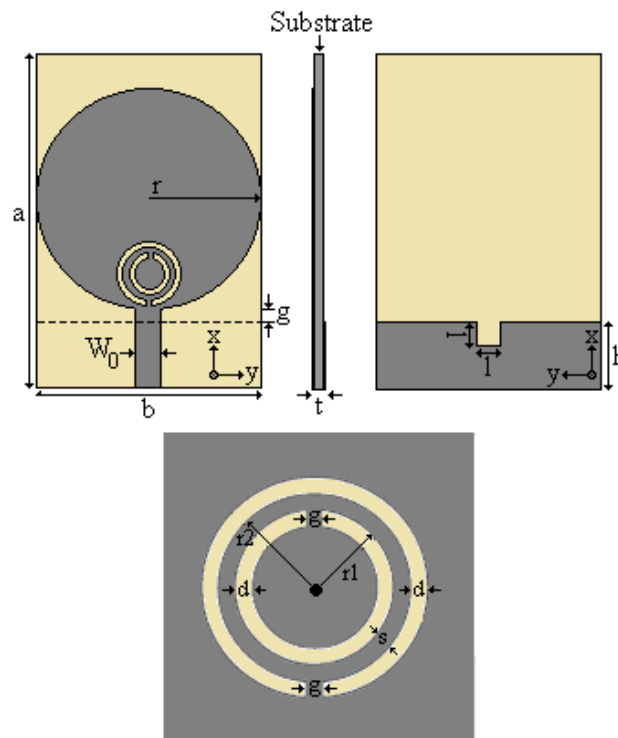
Fig. 4.7 – UWB antenna with CSRR top view and the CRSS structure bottom view; the gray region denotes a conductor material.

To optimize the antenna, three different CSRR positions were tested (Fig. 4.8): one in the patch's center, a second on top of the microstrip line and a third on the right center of the patch.
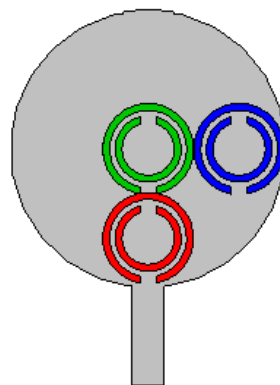
Fig. 4.8 – Monopole antenna with different CSRR configurations.

Fig. 4.9 shows the S11 return loss for the three configurations. The best result was obtained for the CSRR inserted on top of the microstrip line where currents are important so that the CSRR presents a better stop band response. The electromagnetic performance of the antenna was simulated on CST MWS^{TM} by considering the dimensions shown in Fig. 4.7 and an Arlon Diclad 880 isotropic substrate.
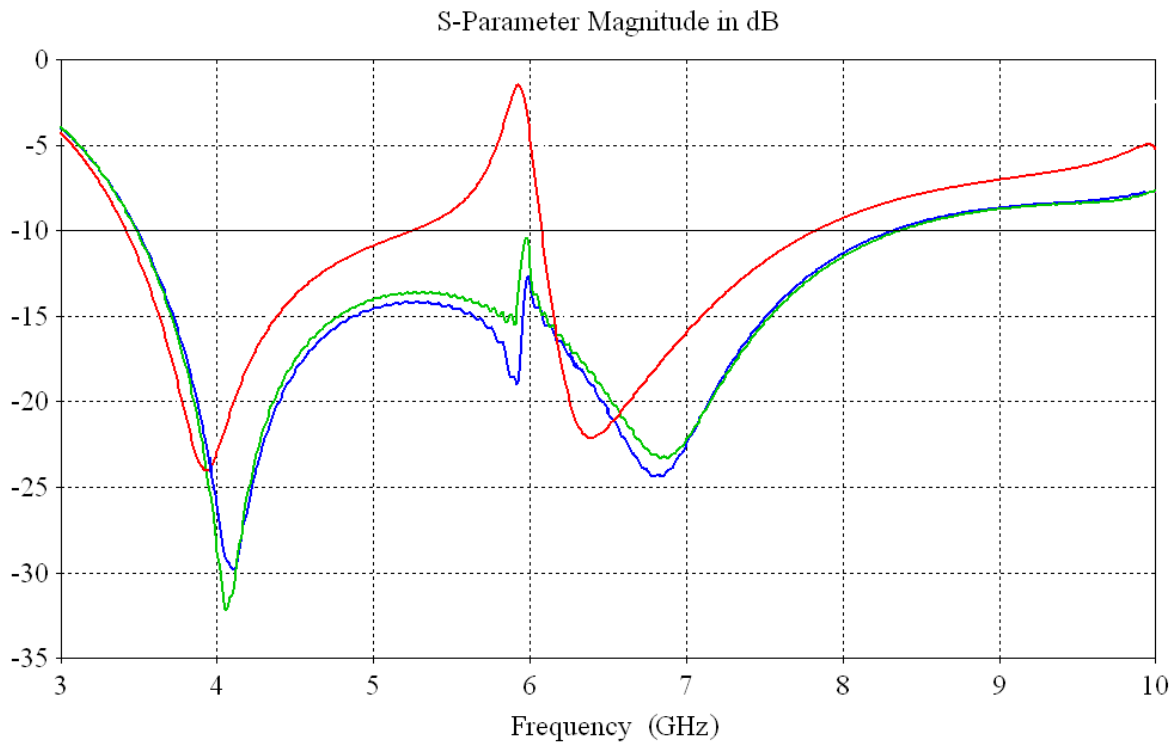
Fig. 4.9 – Simulated Return loss for different CSRR configurations, red microstrip line top center, green patch's center and blue patch's right center.

In the simulation for the final design the losses, both dielectric and conductive, were considered. On the other hand, the conducting patch thickness was considered negligible as it does not affect the results, although the computational time greatly increases when it is considered. The simulation was made in the CST MWS^{TM} where a full wave method was used in the simulation in this case the Transient Solver. The Transient Solver uses an explicit time integration scheme, which implies that the solution is derived by simple matrix vector multiplications. This results in a linear scaling of the numerical effort with the number of mesh points.

The time domain integration calculates the development of fields through time at discrete locations and at discrete time samples. It calculates the transmission of energy between various ports and/or open space of the investigated structure. The fields are calculated step by step through time by the Leapfrog updating scheme. It is proven that this

method remains stable if the step width for the integration does not overcome a known limit. This value of the maximum usable time step is directly related to the minimum mesh step width used in the discretization of the structure. Therefore, the denser the chosen grid, the smaller the usable time step width. This means that a high mesh resolution of a small detail inside a given structure possibly determine the global time step and therefore the total simulation time. Fig. 4.10 shows the constructed structure that was feed by a Jyebao[TM] 50 Ohm SMA8401D-0000 connector.
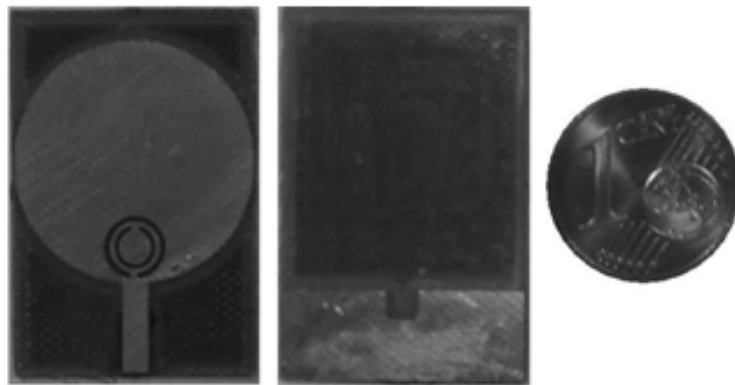
Fig 4.10 – Constructed antenna.

This and all the other prototypes in this thesis were build using a LPKF ProtoMat® S100, Fig. 4.11, high performance printed circuit board prototyping machine for all applications. The ProtoMat® S100 delivers unmatched precision with system resolution as fine as 0.25 µm. Each system was carefully calibrated for unsurpassed overall accuracy. As a result, the plotter can mill and drill all types of PCBs with extremely fine traces, specializing in the precision trace geometries required for the applications in this thesis by RF and microwave boards. Its milling head travel speed of 150 mm per second and high-performance 100,000 RPM spindle motor makes it the premiere high-speed performer for producing the PCBs in-house with clean, nearly perfect traces. A standard RS-232 cable connects the machine to the computer and transfers the design made in the CST MWS[TM].

In the full wave simulation the Transient Solver operates with time pulses, which can be easily transformed into the frequency domain via a Fast Fourier Transformation (FFT). The S-parameters can then be derived from the resulting frequency domain spectra. For a division of the reflected signal by the input signal in the frequency domain yields the reflection factor S11. Within just one simulation run in time domain, the full broadband information for the frequency band of interest can be extracted without the risk of missing any

sharp resonance peaks. For this simulation and the others during this thesis a computer with a 2.53 GHz Intel® Core™ 2 Duo processor, a graphics card with 512MB GDR 5 and 4GB DDR 3 of RAM Memory was used.

Fig. 4.11 – LPKF ProtoMat® S100 printed circuit board prototyping machine.

In order to verify the antenna's performance the structure was measured and simulated and the obtained results were compared. The S11 return loss for both measured and simulated antennas are shown in Fig. 4.12. The antenna return loss is a measure of the amount of power reflected by the antenna toward the generator. A low return loss suggests that the antenna is radiating. It can be observed a good agreement between the simulation and the experimental results. The measurement shows that the antenna has a bandwidth of 4.75 GHz were S11 is below −10 dB.

In addition the three dimensional simulated farfield radiation patterns were calculated for the realized gain at 4 GHz, 5.9 GHz (maximum rejection peak) and 7 GHz, Fig. 4.13. A closer look in Fig. 4.13 (b) shows that the antenna has no gain at 5.9 GHz. This remark proves the efficacy of introducing the CRSS in the antenna's conducting patch.
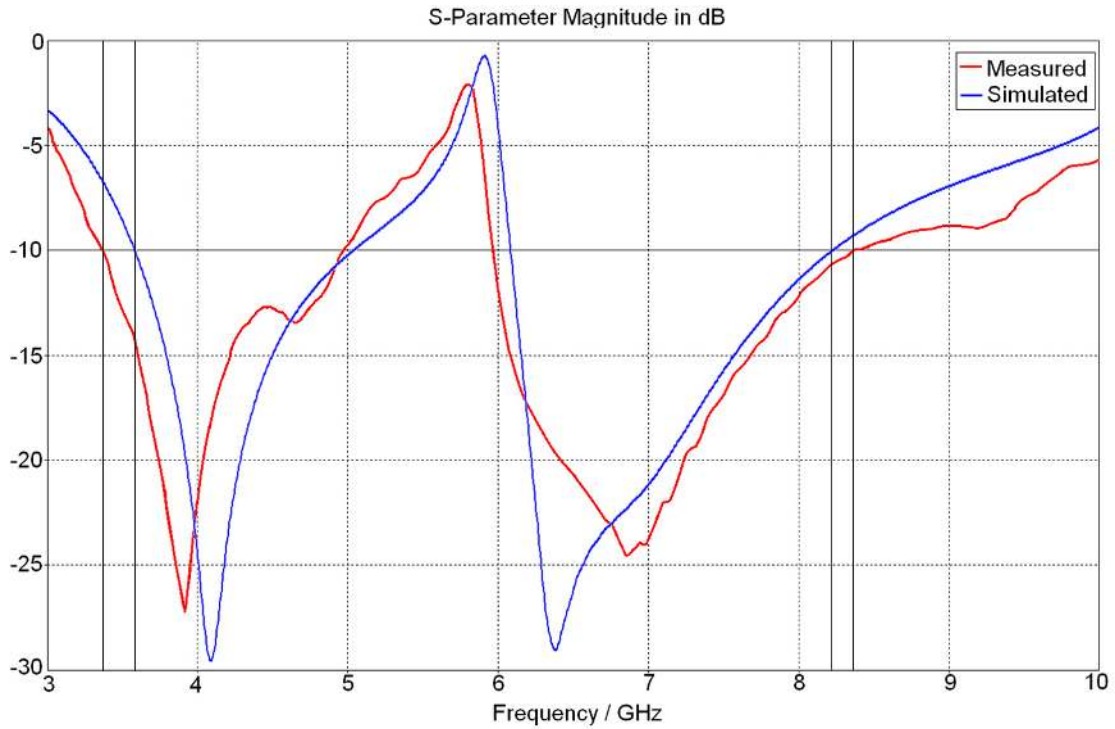
Fig 4.12 – Return loss for the microstrip circular monopole antenna, red measured and blue simulated results.

(a)   (b)   (c)
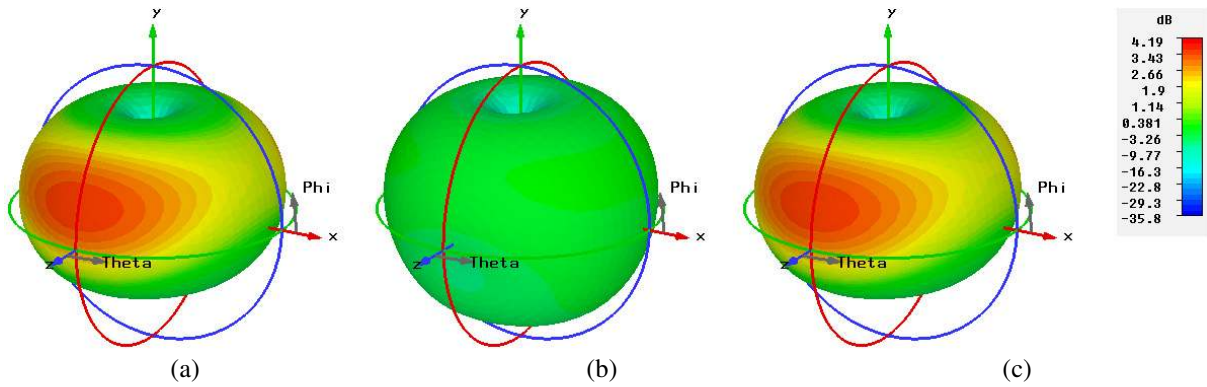
Fig. 4.13 – Realized gain 3D pattern at (a) 4GHz, (b) 5.9GHZ and 6.5 GHz

The far field gain radiation patterns for the H and E planes were measured in an anechoic chamber at Telecom PatisTech and then compared with the ones obtained in the simulation process, see Fig. 4.14. The radiation pattern refers to the directional (angular) dependence of radiation from the antenna or other source. The E-plane for a linearly polarized antenna is the plane containing the electric field vector and the direction of maximum radiation. The E-plane determines the polarization or orientation of the radio wave. For a vertically polarized antenna, the E-plane usually coincides with the vertical/elevation plane. For a horizontally polarized antenna, the E-Plane usually coincides with the horizontal/azimuth plane.

In the case of the same linearly polarized antenna, the H-plane contains the magnetic field vector and the direction of maximum radiation. The magnetizing field (H-plane) lies at a right angle to the E-plane. For a vertically polarized antenna, the H-plane usually coincides with the horizontal/azimuth plane. For a horizontally polarized antenna, the H-plane usually coincides with the vertical/elevation plane. The diagrams were determined according the schema shown in Fig. 4.15, and then the data was processed with the help of the Mathcad^{TM} computer program.

Fig 4.16 presents the simulated and measured radiation patterns for the microstrip monopole antenna with CSRR. The diagrams show a good agreement between the measured and simulated results. Table 4.1 shows the realized gains. It can be noted that at 5.9 GHz (maximum rejection) the antenna has no gain proving the CSRR simulated results. A theoretical and experimental investigation of the microstrip circular patch antenna with CSRR (for nothing the UN-II band) on isotropic dielectric substrate was performed. The prototype was built and measured. The effects of changes in the ground plane in the return loss and the input impedance were investigated. It was observed that the proposed antenna structure led to an excellent bandwidth, greater than 25:1, when calculated for a return loss of less than -10 dB, which makes it suitable for use in several wireless communication systems.

Fig. 4.14 – Anechoic chamber utilized in the measurements.
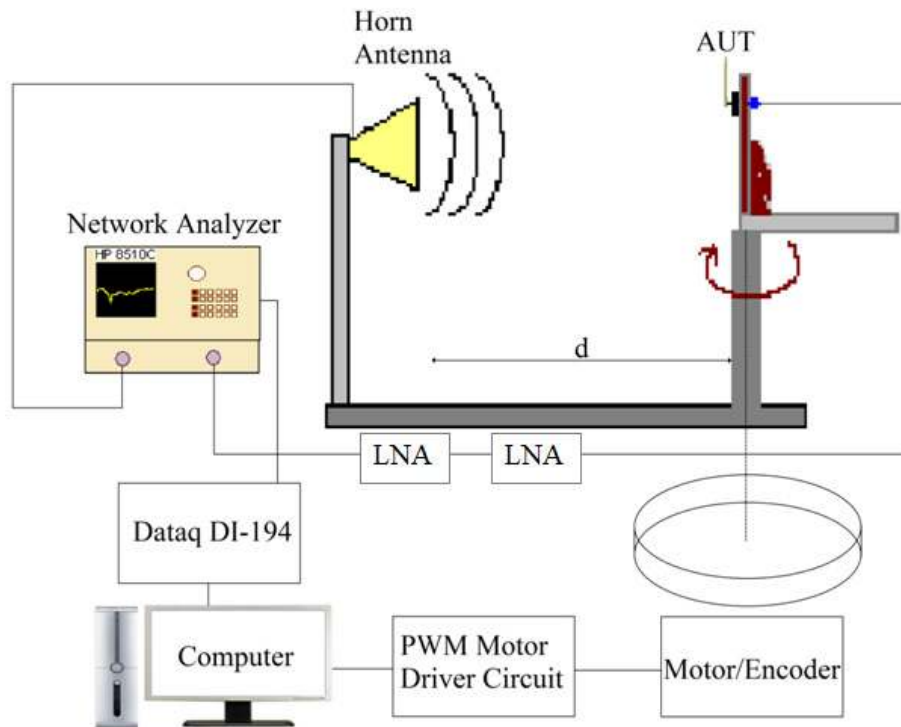
Fig. 4.15 – Measurement schema to determine the radiation pattern.

Antenna design in ultra-wideband systems is a major challenge. For, in contrast to conventional systems, wherein waveform distortion by the antenna is negligible, there is potentially significant waveform distortion by UWB antennas. A further challenge to UWB system design is posed by limits on power spectrum density, such as the FCC emission mask.

The circular monopole is a very broadband antenna. It is not known if the antenna is ideal, i.e., an ideal UWB antenna would have a flat amplitude and a linear phase response over all frequencies. However, the low-frequency falloff of actual antennas is more consistent with meeting the spectral constraints of the FCC mask (Fig. 4.17).

Table. 4.1 – Realized Gain for the microstrip monopole antenna

Frequency	Simulated	Measured
4 GHz	2.72 dB	2.12 dB
5.9 GHz	-2.32 dB	-4.12 dB
6.5 GHz	4.15 dB	3.74 dB
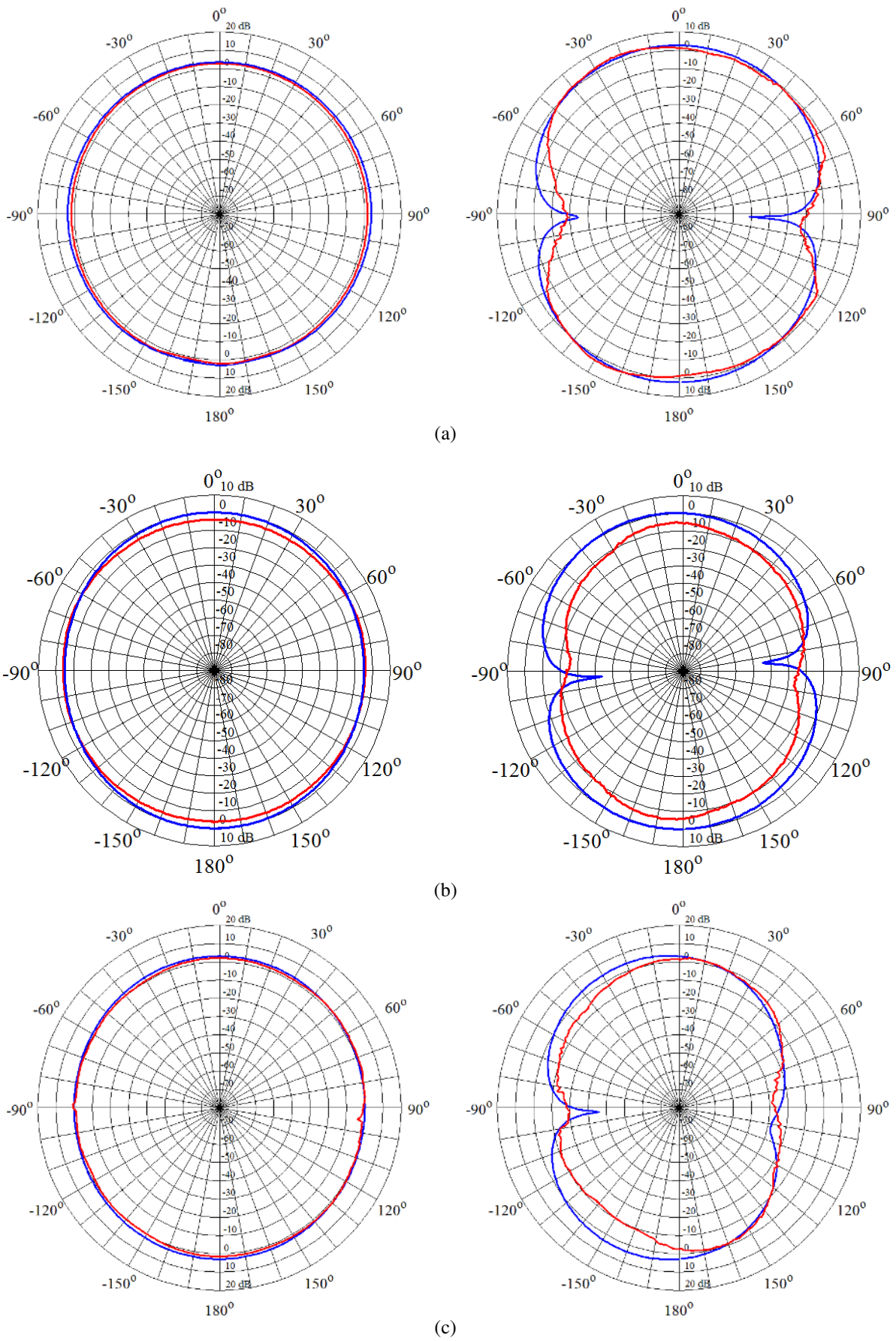
Fig. 4.16 – Farfield radiation patterns, E-plane, on left, results and H-plane, on right, results:(a) 4GHz, (b) 5.9 GHZ and (c) 6.5GHz, blue simulated and red measured.
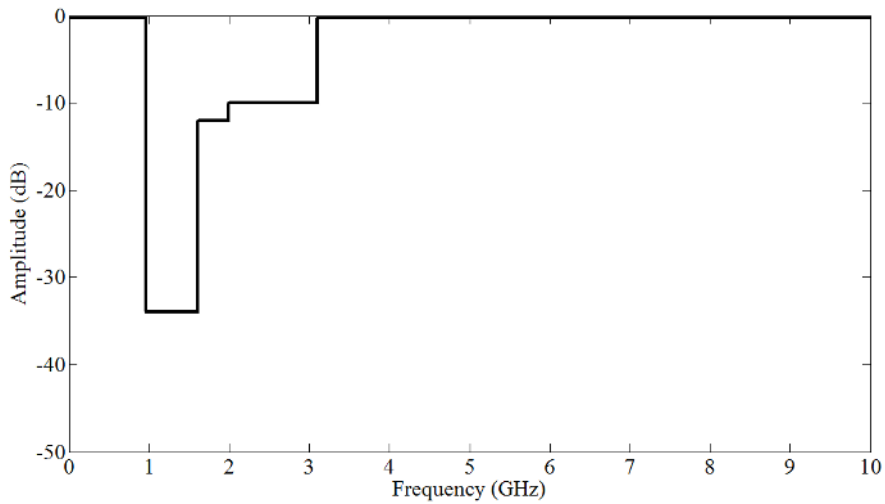
Fig. 4.17 – FCC mask.

The mask encourages UWB operation in the high frequency range, where the antenna is more efficient. The ideal UWB transmission consists of sending a pulse stream, which has exactly the same power spectrum density as the FCC mask, because this would yield the maximum allowable power. Fig. 4.18 shows the FCC pulse. This pulse $fcc(t)$ is a linear combination of sines functions. Thus,

$$\text{fcc(t)} = \sum_{i=1}^{n} a_i \frac{\sin(2\pi f_i t)}{\pi f_i t}, \qquad i = 1,2, \dots n \qquad (4.5)$$

where the a_i coefficients are chosen so that $|Fcc(f)|^2$, where $Fcc(f)$ is the Fourier transform of $fcc(t)$, and has the same shape as the FCC mask in Fig. 4.17. We call $fcc(t)$ the FCC pulse that is based on the FCC mask as the ideal pulse shape to transmit over the air keeping the power spectrum density.
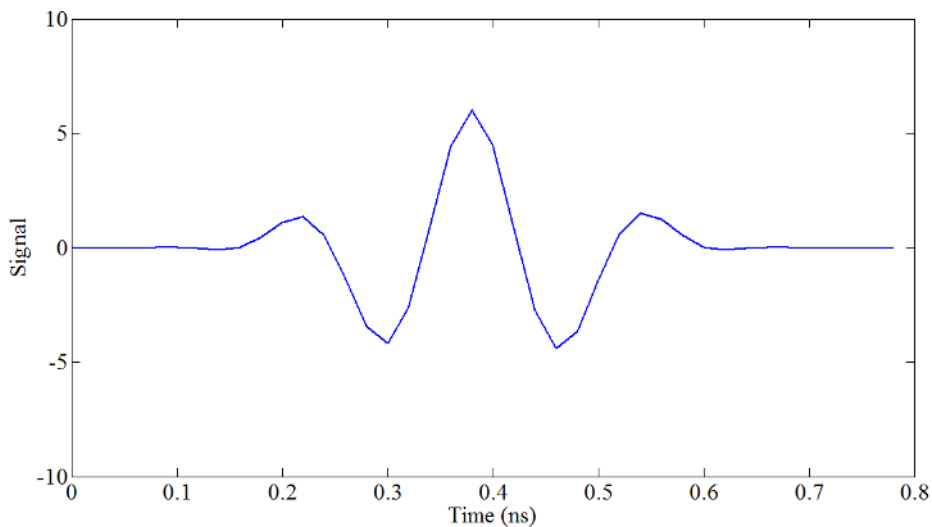
Fig. 4.18 – FCC pulse.

The analysis was made by changing the reference Gaussian pulse by the FCC UWB pulse in the CST MWS™. Fig. 4.19 shows the obtained return loss for the monopole antenna with CSRR inserted in the conductor patch. The results are compared with those obtained for the antenna excited with the Gaussian pulse. It can be noted that the results are very similar and the UWB does not change the antennas matching condition.
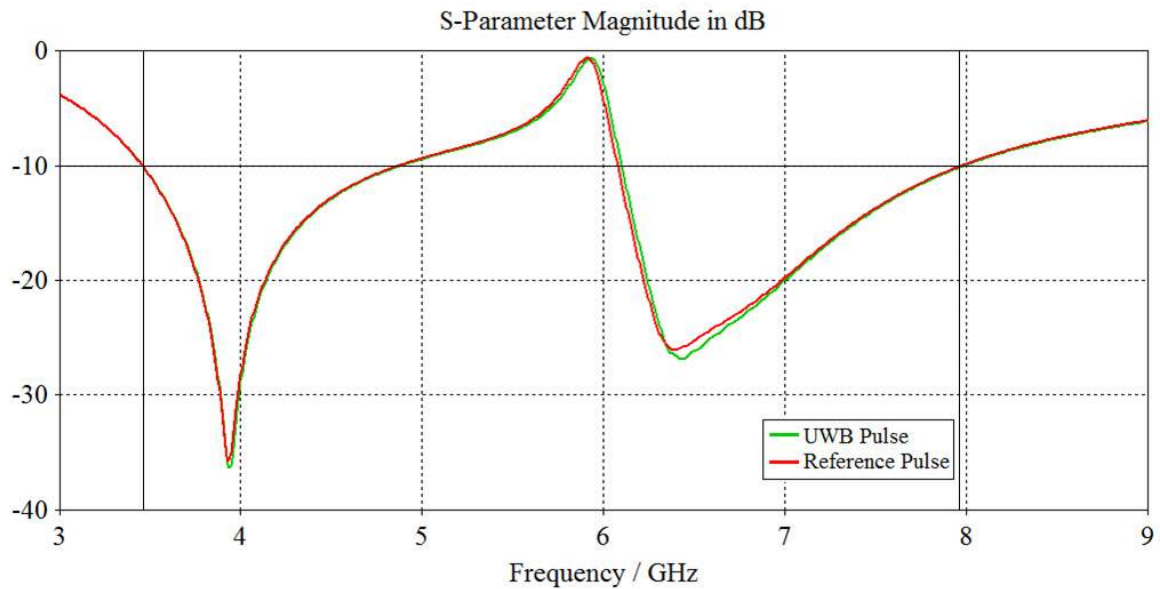
Fig. 4.19 – Return loss for the microstrip monopole antenna with CSRR filter inserted in the conductor patch, green curve antenna exited with UWB pulse and red curve Gaussian pulse.

The next step in the investigation was to simulate two identical antennas excited by the UWB pulse like the result from Fig. 4.19. Fig. 4.20 shows the results from the ground delay from antenna 1 and antenna 2 that are placed 300 away from each other.
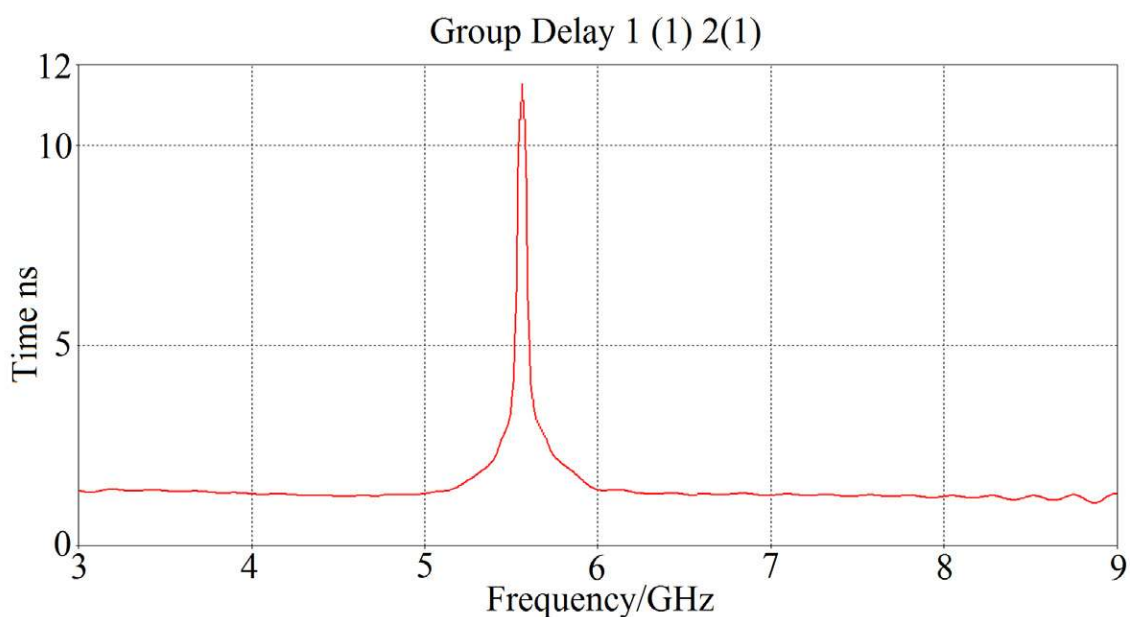
Fig. 4.20 – Group delay from two microstrip monopole antenna with CSRR filter inserted in the conductor patch.

Apart from the frequencies were the CSRR blocks the signal, the group delay is very smooth in the rest of the band, knowing that UWB systems transmit very short duration pulses a smooth ground delay is desirable, so the proposed antenna is suitable for UWB systems.

4.2 – CSRR Stop Band Filter

The frequency selectivity that characterizes the response of resonant-type metamaterial transmission lines lend themselves to their applications in filtering devices. In this section, it is demonstrated that CSRRs can be used for the design of metamaterial transmission lines. From duality, it follows that whereas the dominant mode of excitation of SRRs is, by applying an axial time-varying magnetic field, for CSRRs the main driving mechanism is electric coupling, and a significant component of the electric field parallel to the axis of the rings is required [2]. Thus, by etching the CSRRs in the ground plane in close proximity to the conductor strip, or directly in the conductor strip, the required conditions for CSRR excitation are fulfilled in most common transmission lines.

In summary, filtering characteristics of the CSSR can be analyzed using the LC equivalent circuit model Fig. 4.6. When time varying magnetic field penetrates the CSRR specifically, a current can be induced along the CSRR. Then a distributed inductance is generated in proportion to the length of the CSRR, and a mutual inductance is also generated between the lines of CSRR.

The most common host transmission line for the implementation of one-dimensional metamaterials using CSRRs is the microstrip configuration. By etching the complementary rings in the ground plane, under the signal strip, a significant component of the electric line field results parallel to the rings axis. These structures can design filters with improved filter characteristics with reduced size, due to their size much smaller than the wavelength. As mentioned and demonstrated in the last sections the CSRR has stop band characteristics, so that to start the investigation a single CRSS is etched in the ground plane, Fig 4.21.
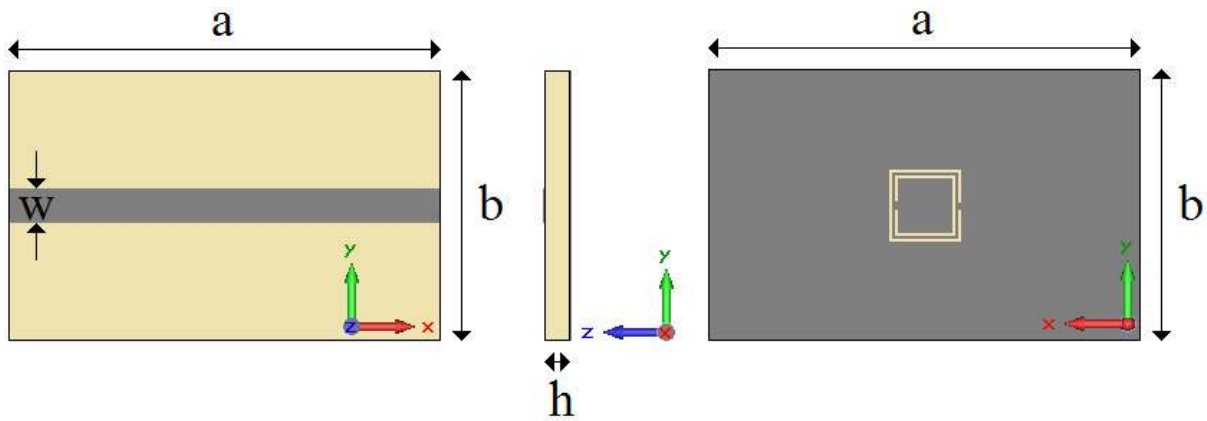
Fig. 4.21 – CSRR stop band filter top. The gray region denotes a conductor material.

Once again the goal is blocking the UN-II band, knowing that the resonance frequency can be tuned changing the CSRR dimensions and number of unit cells the initial design was projected to have stop band characteristics in between 5 GHz to 6 GHz. The simulations was carried out in the CST-MWS using a FR-4 dielectric substrate (permittivity ε_r is 4.15) with a = 30 mm, b 25 = mm, h = 1.58 mm of width. Fig. 4.22 shows the CSRR geometry.
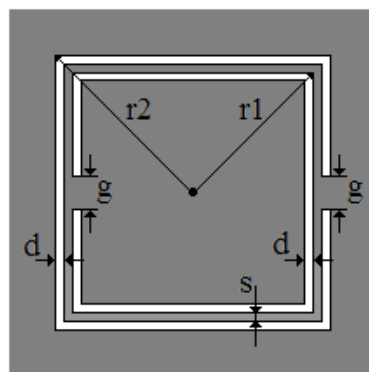
Fig. 4.22 – CSRR geometries. The gray region denotes a conductor material.

Different from the monopole antenna the full wave method used in the simulation processes for the CSRR based filter is the Frequency Domain Solver. In this solver when a time-harmonic dependence of the fields and the excitation is assumed, Maxwell's equations may be transformed into the frequency domain. The fields are then described by phasors that are related to the transient fields by multiplying the phasor with the time factor and taking the real part:

$$\vec{E}(t) = \Re\{\vec{\underline{E}}(\omega) \cdot \exp(i\omega t)\} \tag{4.6}$$

The general purpose Frequency Domain Solver solves the problem for a single frequency at a time, and for a number of adaptively chosen frequency samples in the course of a frequency sweep. For each frequency sample, the linear equation system will be solved by an iterative (e.g., conjugate gradient) or sparse direct solver. The solution comprises the field distribution as well as the S-parameters at the given frequency.

The simulated S-parameters for the structure are shown in Fig. 4.23. The physical dimensions shown in Fig. 4.24 are $r_1 = 4.02$ mm, $r_2 = 4.59$ mm, d = 0.2 mm, g = 0.8 mm, s = 0.2 mm. The upper plane conductor strip has a width w = 3.18 mm, corresponding to a characteristic impedance of 50 Ohms. Due to the negative effective permittivity in the vicinity of CSRR's resonance, the signal is inhibited in a narrow band.
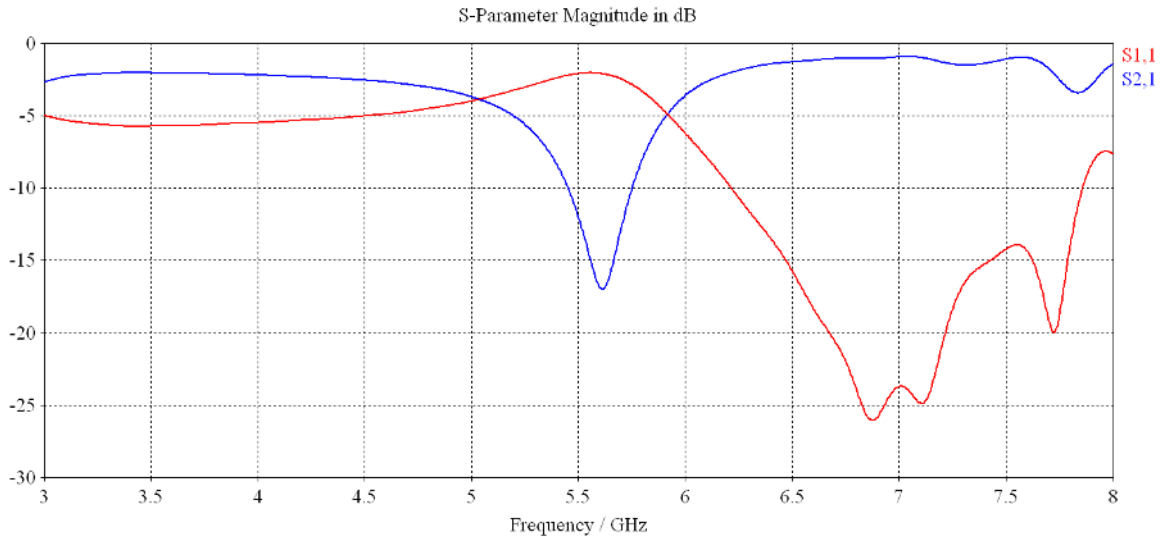
Fig. 4.23 – Simulated S11 and S21 parameters for the metamaterial based stop band with single CSRR.

A solution to increase the bandwidth was found by adding others metamaterial structures in the ground plane. The three-period structure can be seen in Fig. 4.24, the CSRRs are separated by a distance c = 1 mm. The substrate and its dimensions are the same as the ones used in the structure with a single CSRR and the microstrip line has 50 ohm characteristic impedance once again.
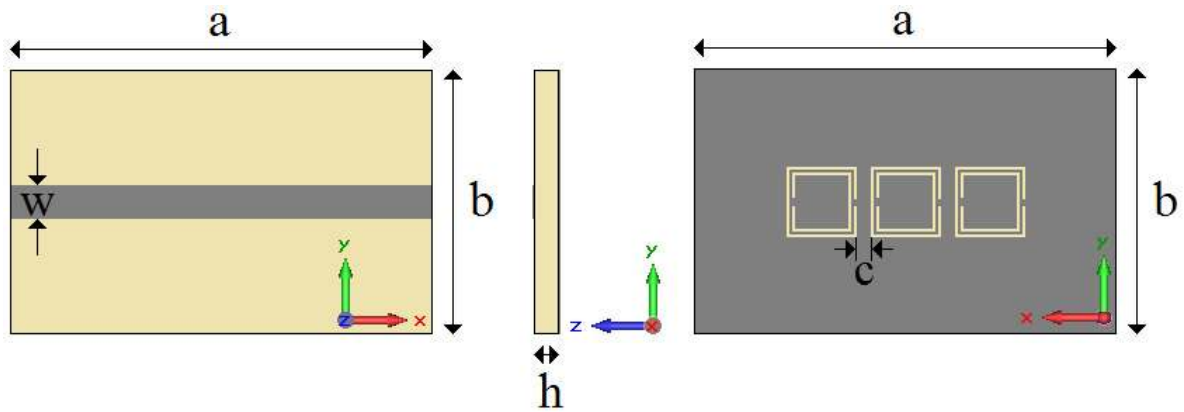
Fig. 4.24 – Three-period CSRR stop band filter, the gray region denotes a conductor material.

The constructed prototype can be seen in Fig. 4.25. The filter was fed by two Jyebao 50 ohm SMA864A-0000 connectors that were also designed in CST MWS^{TM} eviroment for the simulations process. The S-parameters for the three-period CSRR based filter are shown in Fig. 4.26. It can be noted that a deep rejection band is obtained around the design frequency maximum rejection almost 40 dB, and low return losses blocking the all the UN-II band the filter rejection goes from 4.8 GHz to 6.2 Ghz. Below and above the rejection frequency band a flat and matched passband is present with low insertion losses and nearly linear phase variation.
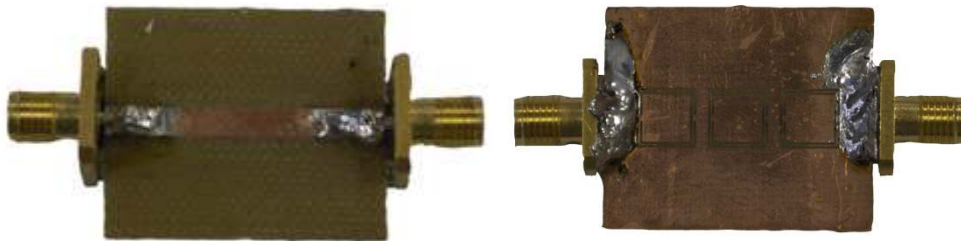
Fig. 4.25 – CSRR based filter prototype.

4.3 – Summary

In this chapter we have described the stopband characteristics of the Complementary Split Ring Resonator. We have presented the design of a small size ultra wide band monopole antenna that exhibits a band-notched characteristic to block for the UN-II band. The antenna consists of a ring structure as the primary radiation element, a CSRR element with a high quality factor to reject the UN-II band and a rectangular cut in the ground plane to improve

the impedance matching. The dimensions of these elements have been examined and optimized using computer simulation. Simulated and measured results are in good agreement.
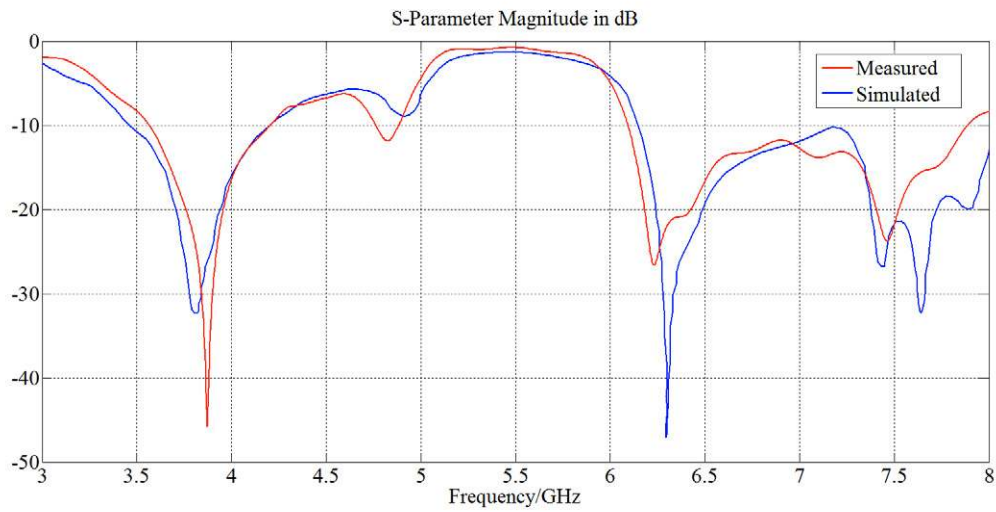
(a)
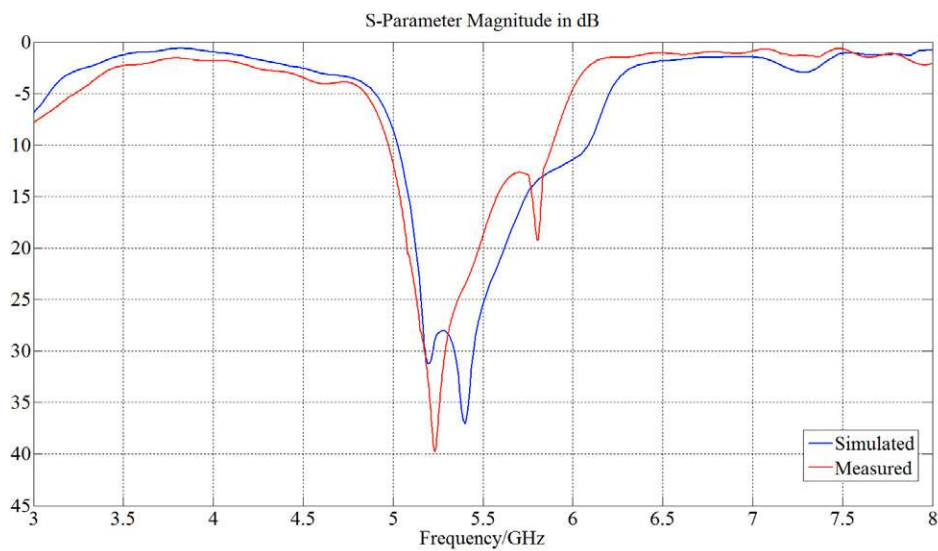
(b)

Fig. 4.26 – S11 (a) and S21 (b) parameters for the metamaterial-based stop band filter with three CSRRs etched do the ground plane: blue simulated and red measured.

Chapter 5

Microstrip Antennas with HIS Ground Plane

Electromagnetic bandgap structures have been widely studied for their behavior as High Impedance Surface. The high-impedance surface has proven to be very useful in a large variety of antennas as a ground plane [67-68]. Antennas have been demonstrated that take advantage of the suppression of surface waves, stop band frequencies in which the tangential magnetic fields are considerably reduced and its unusual reflection phase. At low and high frequencies, the structure behaves as a simple classic ground plane since the reflected waves are in opposition of phase ($\pm 180°$). Around the resonance frequency, the reflected waves are in phase. The structure acts as a magnetic conductor (High Impedance Surface). As a result of the suppression of surface waves, an antenna on a HIS ground plane produces a radiation profile smoother than a similar antenna on a conventional metal ground plane, with less power wasted in the backward direction. The Artificial Magnetic Conductor (AMC) or HIS is a structure designed to imitate the behavior of a perfect magnetic conductor (PMC). In fact, the AMC condition is characterized by the frequencies where the phase of the reflection coefficient is zero, i.e., $\Gamma = +1$.

This can be applied to a variety of antenna designs, including patch antennas, which often suffer from the effects of surface waves. For phase-arrays, the suppression of surface waves can reduce inter-element coupling, and help to eliminate blind angles. The unique reflection phase properties of the high-impedance surface allow the design of new low-profile antenna, with radiating elements lying flat against the ground plane. These antennas can take on a variety of forms, including straight wires to produce linear polarization, or various other shapes to generate circular polarization. The high-impedance surface is particularly applicable to the field of portable hand-held communications, in which the interaction between the

antenna and the user can have a significant impact on antenna performance. Using this new ground plane as a shield between the antenna and the user in portable communications equipment can lead to higher antenna efficiency, longer battery life, and lower weight.

5.1 – High Impedance Surface

To understand the behavior of a High Impedance Surface let's first consider an electric conductor. While a conductive surface is a good reflector, it has the unfortunate property of reversing the phase of reflected waves.

The electromagnetic surface properties of a conductor can be changed incorporating a special texture to it. A flat sheet driving surface has a low impedance, while with a specially designed geometry, the textured surface can have high surface impedance. A high-impedance surface, shown in cross section in Fig. 5.1, consists of an array of metal protrusions on a flat metal sheet.

Fig. 5.1 Cross-section of a high-impedance surface

The HIS is arranged in a two-dimensional structure formed with metal plates on top, attached to the conductor ground plane with metallic vias. As mentioned before the HIS can be visualized as mushrooms protruding from the surface. The high impedance surface electromagnetic properties can be described using lumped circuit elements see the LC circuit describe in Fig. 3.7.

In this thesis the high impedance surface is used as an antenna ground plane. To explain how a HIS changes an antenna characteristics let us consider a microstrip patch antenna. A patch antenna is a simple antenna example that consists of single conductor patch element printed in a dielectric substrate backed by a conductor ground plane. A patch antenna has a length of microstrip transmission line of approximately one-half wavelength. The radiation mechanism arises from discontinuities at each truncated edge of the microstrip transmission line. This kind of antenna is low profile and the radiation at the edges causes the antenna to be larger than its physical dimension and they are also narrowband. Fig. 5.2 shows

a patch antenna fed by a coaxial probe. Ideally a patch antenna should be placed on a infinitely large ground plane and a smooth radiation pattern and no backward radiation. But in practice the ground plane is finite and its edges will affect the radiation pattern. The surface waves formed by the antenna will interact with the edges and combine with the radiation from the ground plane. The substrate edges will form a series of multipath lobs that will cause a waste of the radiated power and alter the radiation pattern.
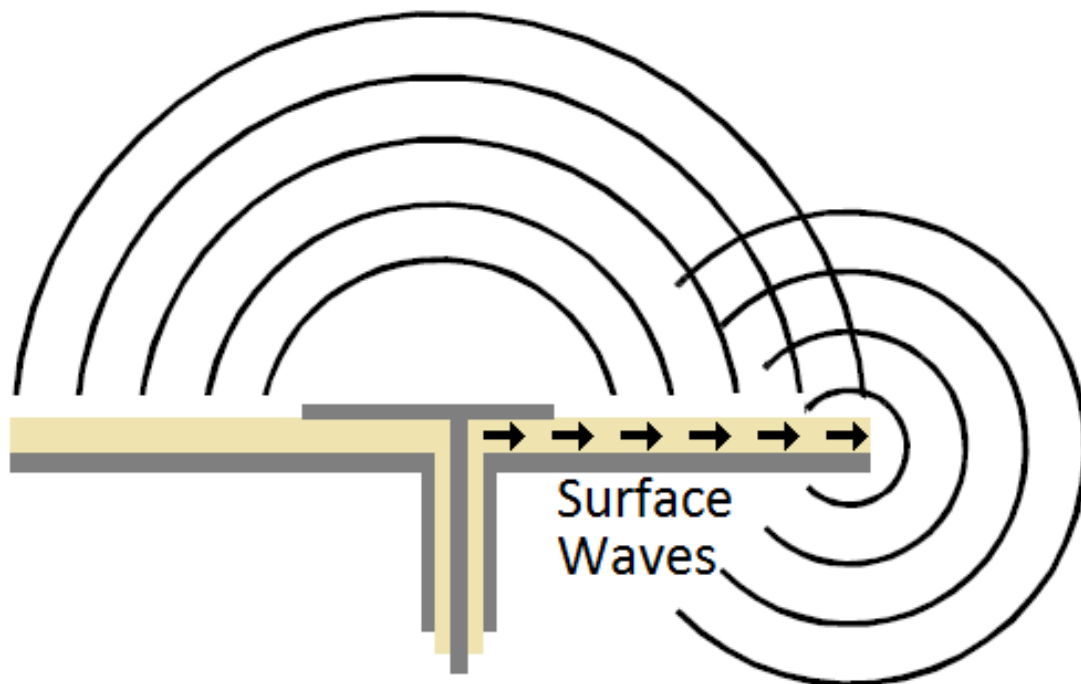
Fig. 5.2 – A patch antenna on a metal ground plane.

Surface waves radiate from the edges of the ground plane, causing ripples in the antenna pattern and radiation in the backward direction. If the substrate is thick, or it has a high dielectric constant, the surface wave problem is increased. If the metal ground plane is replaced with a high-impedance ground plane, as shown in Fig. 5.3, the surface waves are suppressed.

While driven currents exist on any conductive surface, they do not propagate on a high impedance ground plane. The surface currents are kept to a region around the patch, and never reach the ground plane edges. The absence of multipath interference results in a smoother radiation pattern, resulting in less wasted power in the backward hemisphere. The surface current in the HIS flow around a long path through the vias and the bottom plate.
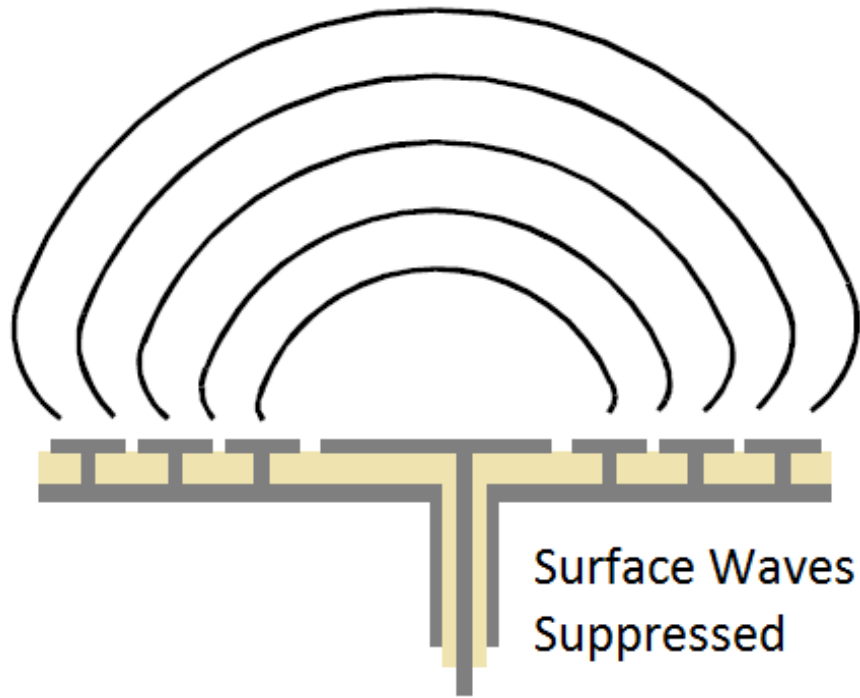
Fig. 5.3 – A patch antenna embedded in a high-impedance ground plane.

5.2 – Microstrip Patch Antenna with HIS Substrate

To construct the antenna ground plane a mushroom like HIS is used. The HIS consists of square elements that can be placed in a planar two-dimensional array. The unit cell and its dimensions are shown in Fig. 5.4. To evaluate the scattering properties of this array, that is infinitely extent in its plane, the CST MWS^{TM} was utilized. The structure was modeled in an Arlon DiClad 880^{TM} ε_r = 2.17 substrate and the mushroom like unit HIS cell has the following dimensions (see Fig. 5.4) a = 5.06 mm, and b = 4.74 mm. The square patch is connected to the ground by a metallic wire whit radius r = 0.5 mm and the height is the same of the dielectric substrate h = 0.768 mm. The HIS can be fabricated using printed circuit board technology.
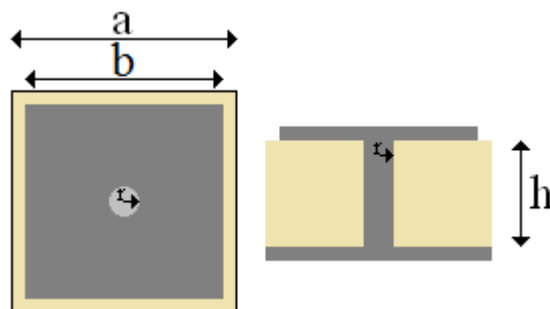
Fig. 5.4 – HIS superior view on the left and transversal cut on the right.

Fig. 5.5 shows the simulated magnitude and phase of the reflection coefficient, versus frequency. The Frequency Domain Method is used in this analysis. It should be noted here that all losses in the metals present in our numerical simulations are considered. Considering the periodicity, the simulation of an entire array would be prohibitively time and memory consuming. The use of CST MWS^{TM} unit cell boundary conditions in the directions of periodicity allows a rapid but no less accurate simulation of large surfaces. Setting up the simulation by using the "FSS - Unit Cell (FD)" template, which applies unit cell boundary conditions in the x- and y-directions and sets up Floquet port excitations in the positive and negative z-directions. There is no need to define master and slave boundary conditions, the phase relation of the opposing boundaries is set by specifying the incident angle of the inward travelling plane wave. It is only necessary to construct a single patch on its backing substrate.

Using the Floquet theorem an arbitrary field can be represented by an infinite summation of plane waves so the single cell is in turn embedded in the scattered field region with connection walls in the propagation z direction [68]. The other boundaries are truncated by absorbing boundary walls.

In Fig. 5.5, the phase of the reflection coefficient at 12.25 GHz is shown to be approximately 90 degrees. As the frequency increases, this phase passes through 0 degrees and goes towards to - 90 degrees. At the frequency where the phase is 0 degrees (13.63 GHz), the surface above the ground plane achieves an overall reflection coefficient of +1 and therefore acts as a high impedance surface (i.e., artificial magnetic conductor). Far away from this resonance denoted by HIS, this surface has an overall reflection coefficient of -1, and thus acts as a traditional electric conducting ground plane. The bandwidths here are defined by the frequency values where the reflection coefficient phase falls between ± 90 degrees.

Although the surface exhibits high impedance, it is not actually unprovided of current. If there were no current, electromagnetic waves would be transmitted right through the ground plane. However, the resonant structure provides a phase shift, thus, the image currents in the surface reinforce the currents in the antenna, instead of canceling them.

At very low frequencies, the reflection phase is π, and the structure behaves like an ordinary flat metal surface. The reflection phase slopes downward, and eventually crosses through zero at the resonance frequency. Above the resonance frequency, the phase returns to $-\pi$. The phase falls within $\pi/2$ and $-\pi/2$ when the magnitude of the surface impedance exceeds the impedance of free space. Within this range, image currents are in-phase, rather than out-of-phase, and antenna elements may lie directly adjacent to the surface without being shorted out. The surface impedance is modeled as a parallel resonant circuit, which can be tuned to

exhibit high impedance over a predetermined frequency band. The high-impedance surface can be considered as a kind of two-dimensional photonic crystal that prevents the propagation of radio-frequency surface currents within the bandgap. As the structure illustrated in Fig. 3.7 interacts with electromagnetic waves, currents are induced in the top metal plates. A voltage applied parallel to the top surface causes charges to build up on the ends of the plates, which can be described as a capacitance. As the charges slosh back and forth, they flow around a long path through the vias and bottom plate. Associated with these currents is a magnetic field and, thus, an inductance.
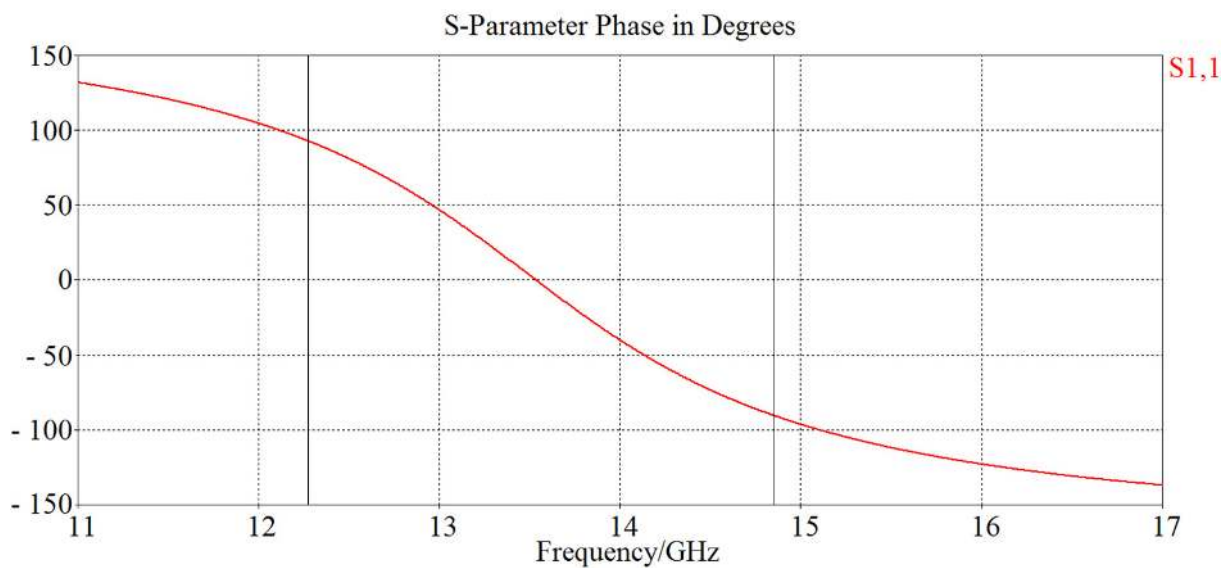
Fig. 5.5 – Reflection coefficient for the mushroom type HIS.

Once the HIS band was defined the next step was insert an antenna inside the HIS medium in this case a square patch was used. The antenna dimensions are L = 6.4 mm, Fig. 5.6. The footprint dimensions are (80 x 80 mm). The HIS and the antenna are backed by a complete ground plane. The HIS array was placed around the antenna and the antenna was out centered in 1 mm for matching proposes. The surface current suppression are shown in Fig. 5.7 where it can be seen that the surface current in the HIS is very week and the minor interactions are kept in the antennas nearby surroundings.
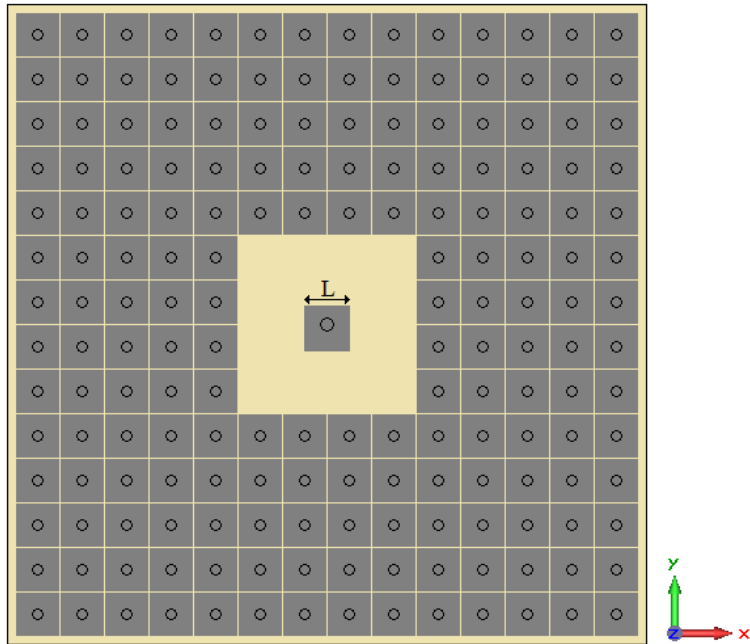
Fig. 5.6– Patch antenna inserted in the HIS medium.
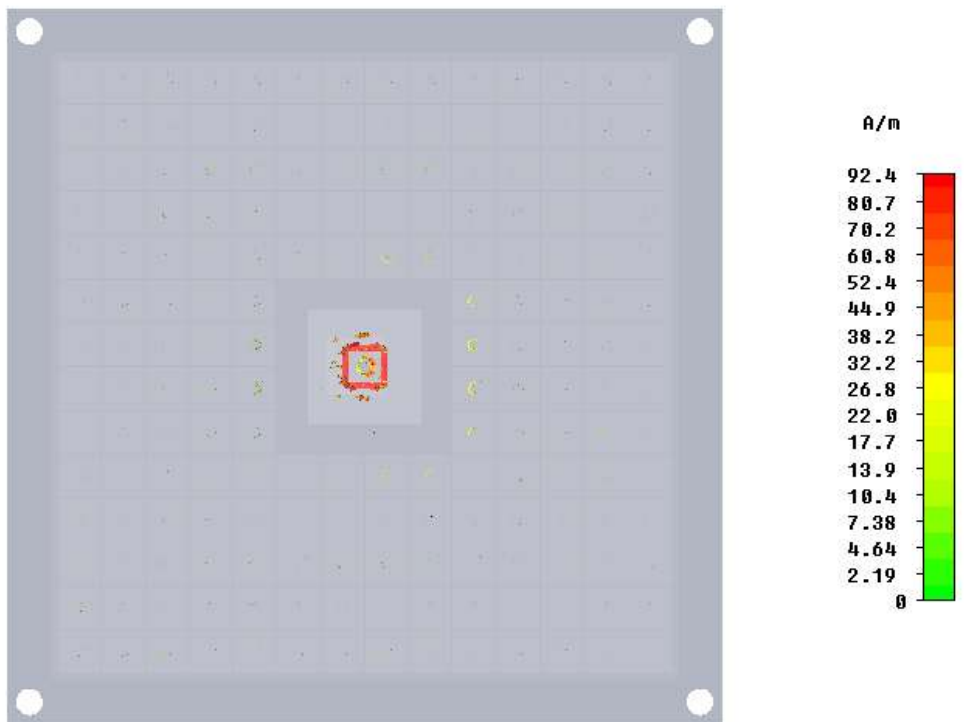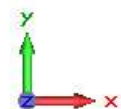
Fig. 5.7 – Surface current at the bandgap frequency center 13.23 GHz, yellow circles surrounding the patch.

The presence of the square patch's surrounding the antenna tends to change its resonance frequency, since the effective cavity volume is reduced. This can be reduced by leaving a small guard ring of bare substrate around the patch antenna. Fig. 5.8 shows the S11 simulation of two patch antennas, one on an ordinary, dielectric substrate backed by a metal ground plane, and one on a high-impedance ground plane. In both antennas, the substrate has an Arlon DiClad 880^{TM} with dielectric constant of 2.17, a thickness of 0.768 mm and size 80 mm X 80 mm. The antennas are a square patch, with diameter of 6.4 mm. Both patches are out centered in 1 mm for matching purposes. The antennas are fed by a Jyebao^{TM} 50 Ohm SMA864A-0000 connector placed in the center of the dielectric. The SMA connector was designed in the simulation software. The patch antenna on the high impedance impedance ground plane was surrounded by a guard ring consisting of 7 mm of bare dielectric. The presence of the surrounding metal patches in the HIS medium tends to confine the electromagnetic fields and slightly alter the resonance frequency. It can also be shown that the antenna on the HIS ground plane has a larger bandwidth and a deeper return loss. The bandwidth were S11 is below – 10 dB for the antenna with HIS is 440 MHz and for the antenna without HIS the bandwidth is 390 MHz.
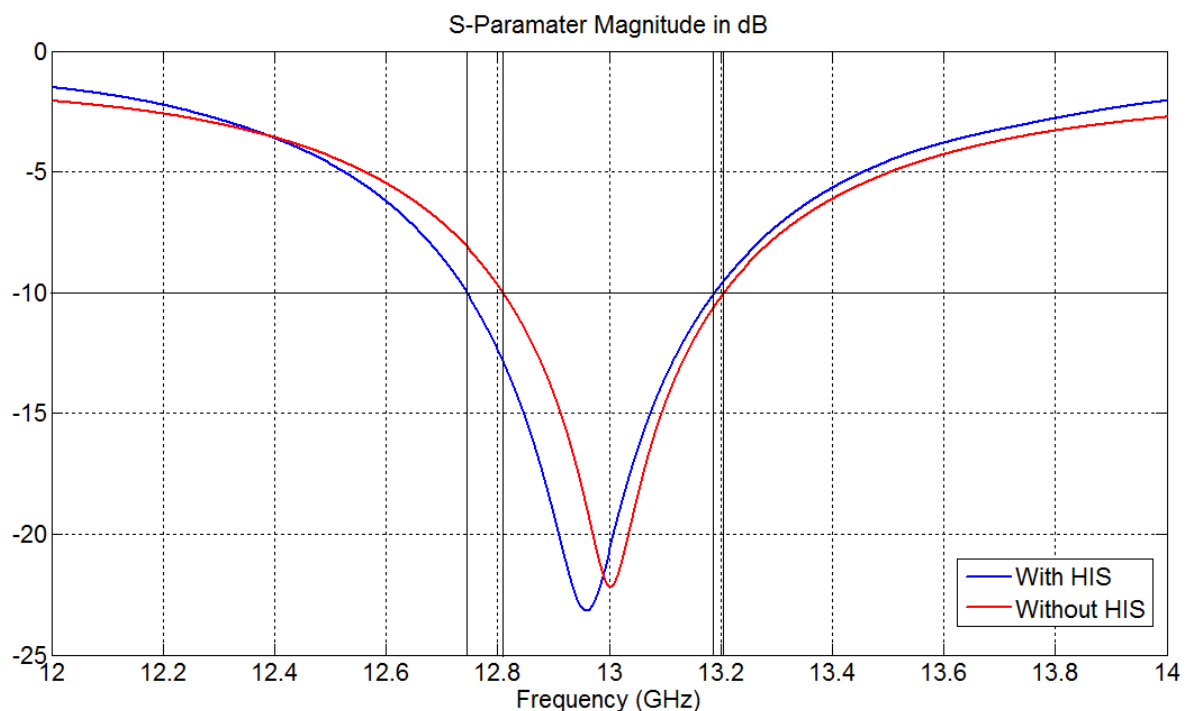
Fig. 5.8 – S11simulation for patch antennas on two different ground planes

The constructed prototype is shown in Fig. 5.9. The antenna is feed by a Jyebao[TM] 50 Ohm SMA864A-0000 and is mounted on a Arlon DiClad 880[TM] dielectric substrate with dielectric constant 2.17.
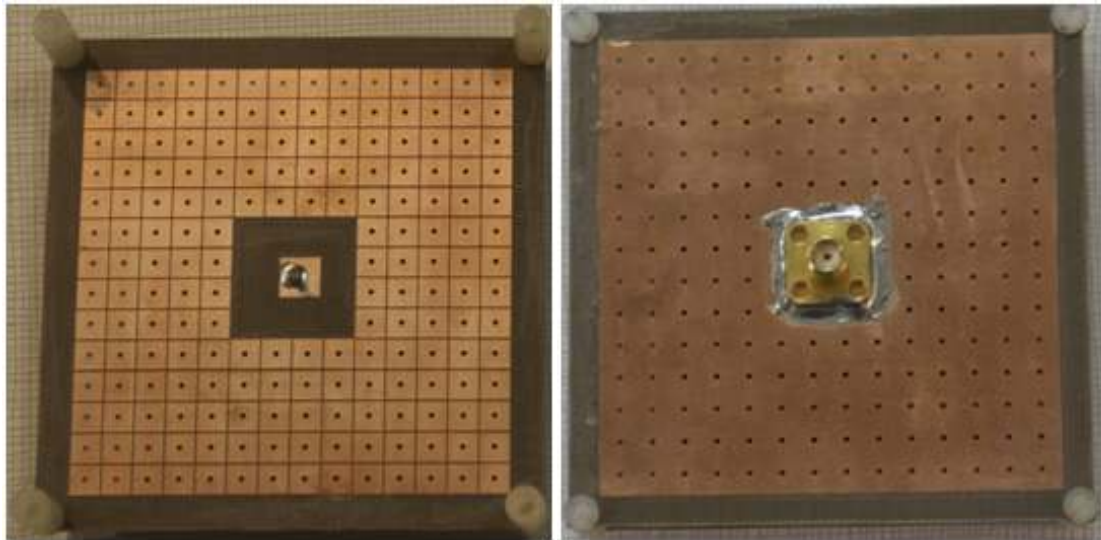
Fig. 5.9 – Constructed structure right superior front view and left superior back view.

The LPKF ProtoMat® S100 was used do make the structure an drill the roles. Then the LPKF MiniContac RS, Fig. 5.10, was used for the metallization process to connect the patches to the ground plane. The system use switchable reverse pulse plating, producing uniform copper plating for difficult aspect ratios and smaller holes. Reverse pulse plating uses precisely controlled reverse pulses to remove excess material during the plating process. The through-hole plating process starts with the cleaning of the circuit boards. The PBCs are degreased, then pre-treated, then activated. A galvanic bath adds the copper coat.

Courtesy LPKF Laser & Electronics, 12555 SW Leveton Dr. Tualatin, OR 97062, copyright.

Fig. 5.10 – LPKF MiniContac RS.

The next step in the investigation is to obtain the return loss for the patch antenna with HIS ground plane. Fig. 5.11 shows the obtained results in the simulation that are compared to the measured. Differently from the simulation for the HIS phase the return loss is obtained with the Transient Solver. Fig. 5.11 shows that the simulated and measured results are in good agreement.

An antenna lying parallel to the metamaterial surface will see the impedance of free space on one side, and the impedance of the ground plane on the other side. Where the metamaterial surface has low impedance, far from the resonance frequency, the antenna current is mirrored by an opposing current in the surface. Since the antenna is short circuited by the nearby conductor, the radiation efficiency is very low. Within the forbidden bandgap near resonance, the metamaterial surface has much higher impedance than in free space. Therefor the antenna is not shorted out. In the bandgap range of frequencies, the radiation efficiency is high.
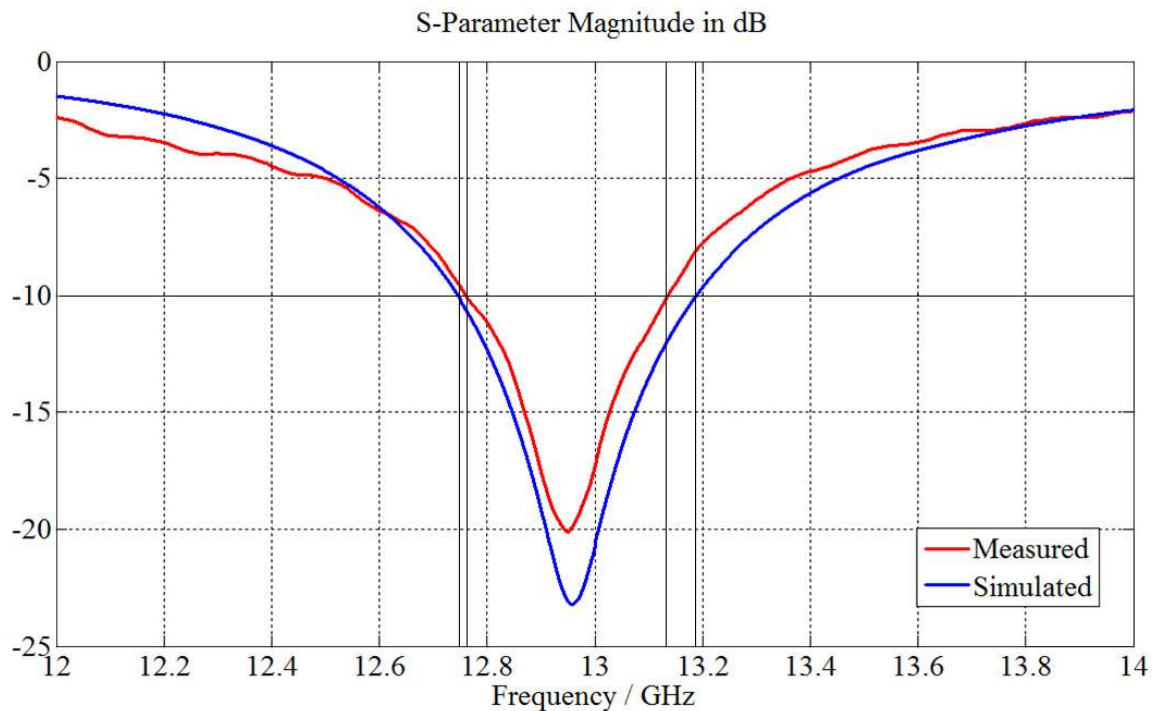
Fig. 5.11 – Return loss simulated and measured for the patch antenna on a high-impedance ground plane.

Following, the realized gain radiation patterns are determined for this antenna, Fig. 5.12 show the obtained results for (a) 12.75 GHz, (b) 12.95 GHz, and (c) 13.15 GHz. It can be noted a good agreement between the simulated and measured results. A closer look to the radiation patterns proves that the back radiation is suppressed, i.e., the backward ripples have gains around -10 dB. The noise in the measured results can be attributed to losses in the cables used in to obtain the measurements.
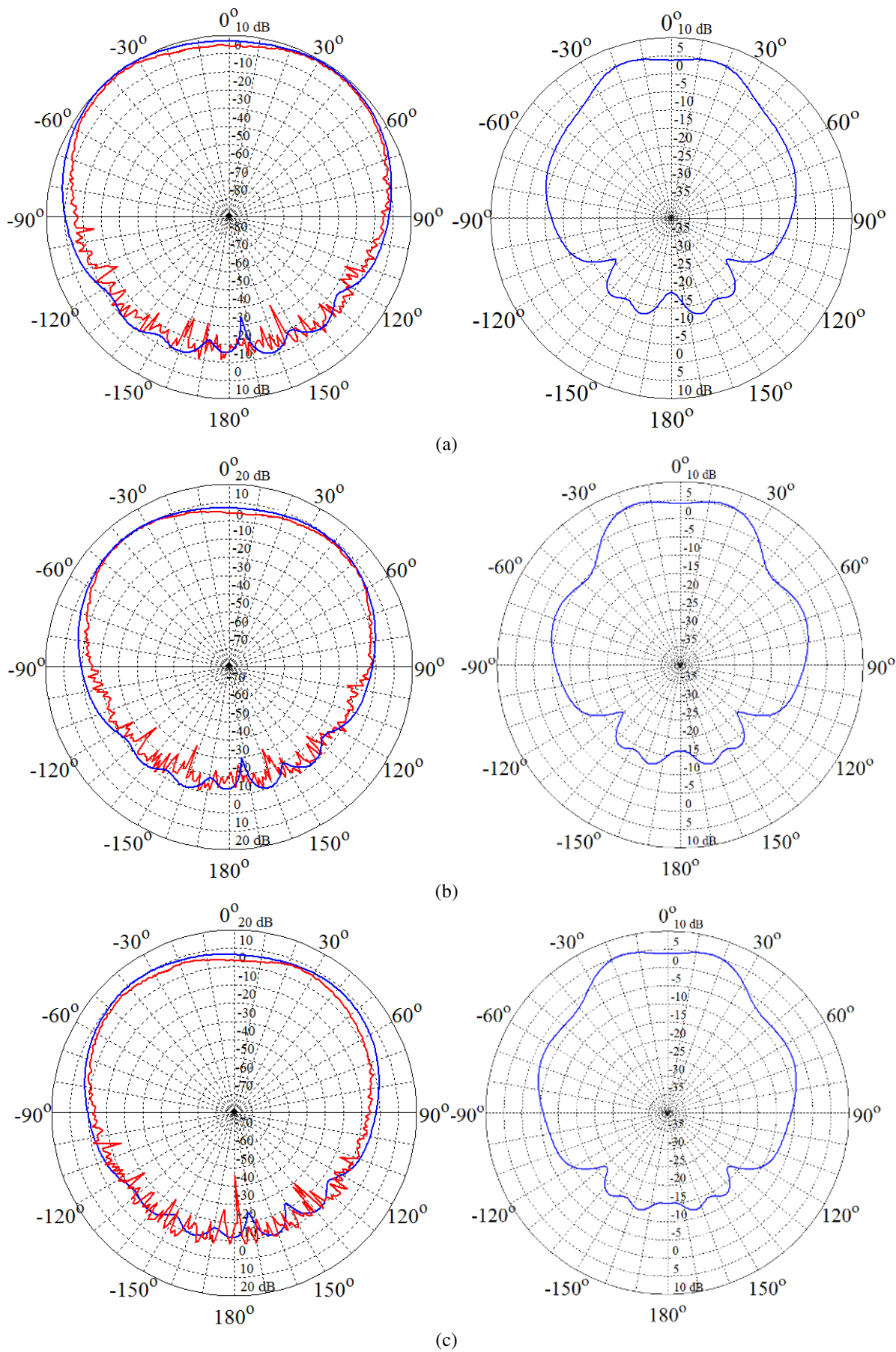
Fig. 5.12 – Farfield realized gain radiation patterns for the, E-plane on the left and H-plane on the left, blue simulated and red measured results: (a) 12.75 GHz, (b) 12.95 GHz and (c) 13.15 GHz.

5.3 – Suspended U-Slot Antenna on HIS Substrate

A low profile broadband antenna is presented in this section. A suspended U-slot antenna is investigated as an alternative for the patch antenna. In general, the plate of this type of antenna is suspended over a ground plane, in this case a HIS, at a height of ± 0.1 times the operating wavelength in free space. The medium between the plate and ground plane is basically air or a substrate of very low relative permittivity. In contrary to other existing feeding structures, such as a direct microstrip line feed, an aperture in the ground plane is made with proximity coupling, a long and isolated coaxial probe feed is the chosen option for this antenna because of the large spacing and the very low relative permittivity in between the antenna and the ground plane. Furthermore, to compensate the large reactance due to the long probe in a broad frequency range the antenna is off centered by 1.1 mm for matching purposes.

The antenna operating frequency was determined in the CST MWS^{TM}. The scattering properties of the HIS were determined following the same method used in the patch antenna. The ground plane structure was modeled in an FR-4 $\varepsilon_r = 4.19$ substrate and the mushroom like unit HIS cell has the following dimensions (see Fig. 5.4) a = 10.6 mm, and b = 10.32 mm. Again the square patch is connected to the ground by a metallic wire whit radius r = 0.75 mm and the height is the same as the dielectric substrate, h = 1.58 mm. Fig. 5.13 shows the obtained phase.
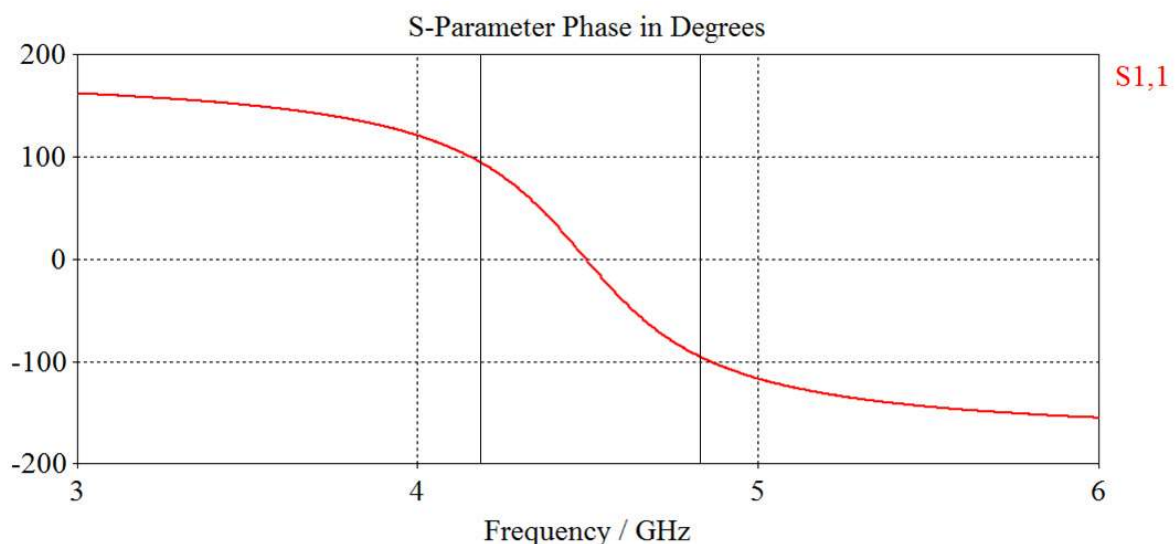
Fig. 5.13 – Reflection coefficient for the mushroom type HIS.

Based on this idea, a suspended rectangular U-Slot antenna backed by a HIS substrate is designed and shown in Fig. 5.14. Essentially, the use of thin low-permittivity substrates (Arlon DiClad 880[TM] ε_r = 2.17 and width 0.768) is a key ingredient to attain the broad impedance bandwidth of a single-element single-layer antenna. So, in this design a conducting plate of length L = 35.5 mm and width W = 24 mm. The other conducting patch dimensions are W_1 = 2.1 mm, L_1 = 1.8 mm, L_2 = 5.35 mm and L_3 = 2.7 mm.
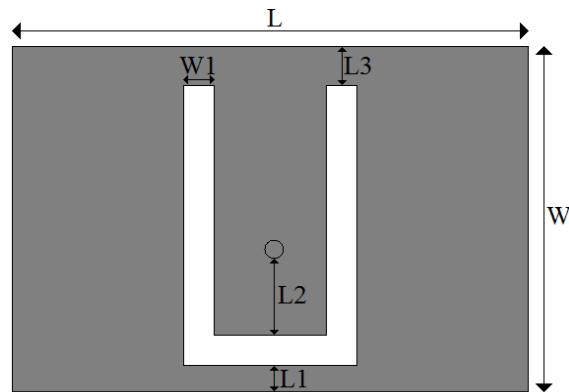
Fig. 5.14 – U-slot antenna and its dimensions.

The antenna was suspended parallel to the ground plane at a height h = 5 mm. A rectangular FR-4 plate measuring 180 mm x 180 mm was used instead of the infinite ground plane. The operating frequency is around 4.5 GHz. The plate will centrally be fed to keep the overall configuration symmetrical. A Jyebao[TM] 50 Ohm SMA864L-0000 connector is used to feed the antenna. The antenna was simulated following the same process used in the patch antenna study. The designed antenna is shown in Fig. 5.15 and the constructed antenna in Fig. 5.16. The same manufacturing process used for the patch antenna is used in the suspended U-slot antenna.
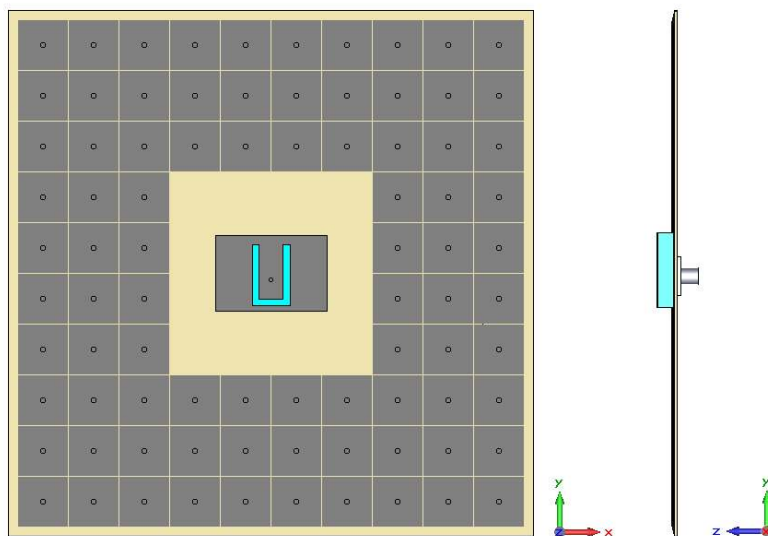
Fig. 5.15 – Suspended U-Slot antenna backed by a HIS medium.
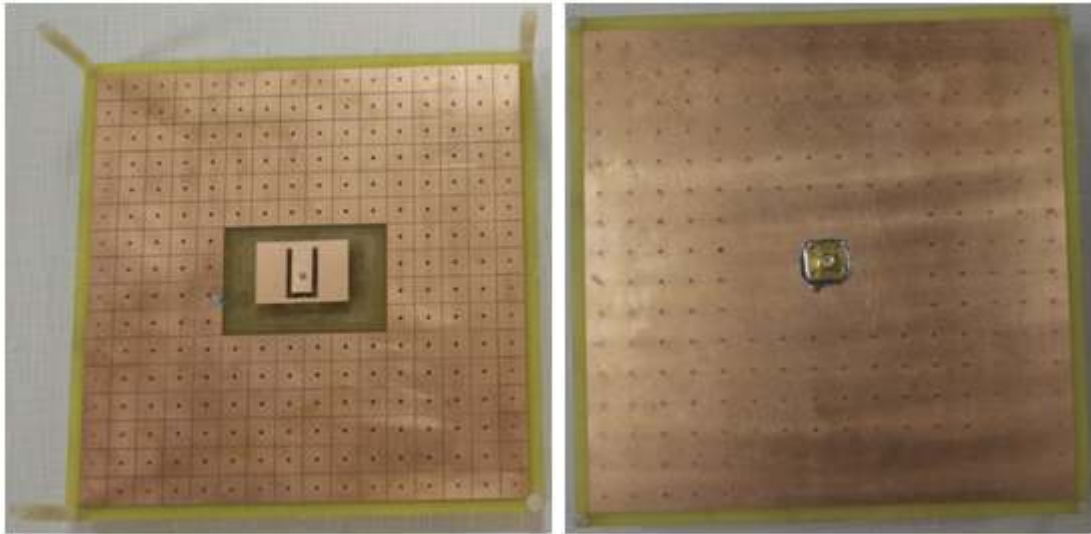
Fig. 5.16 – Constructed prototype right superior front view and left superior back view.

Fig. 5.17 shows the return loss versus frequency for the suspended U-slot antenna with HIS ground plane. The full wave method and the simulation process are the same as the ones used for the patch antenna analysis.
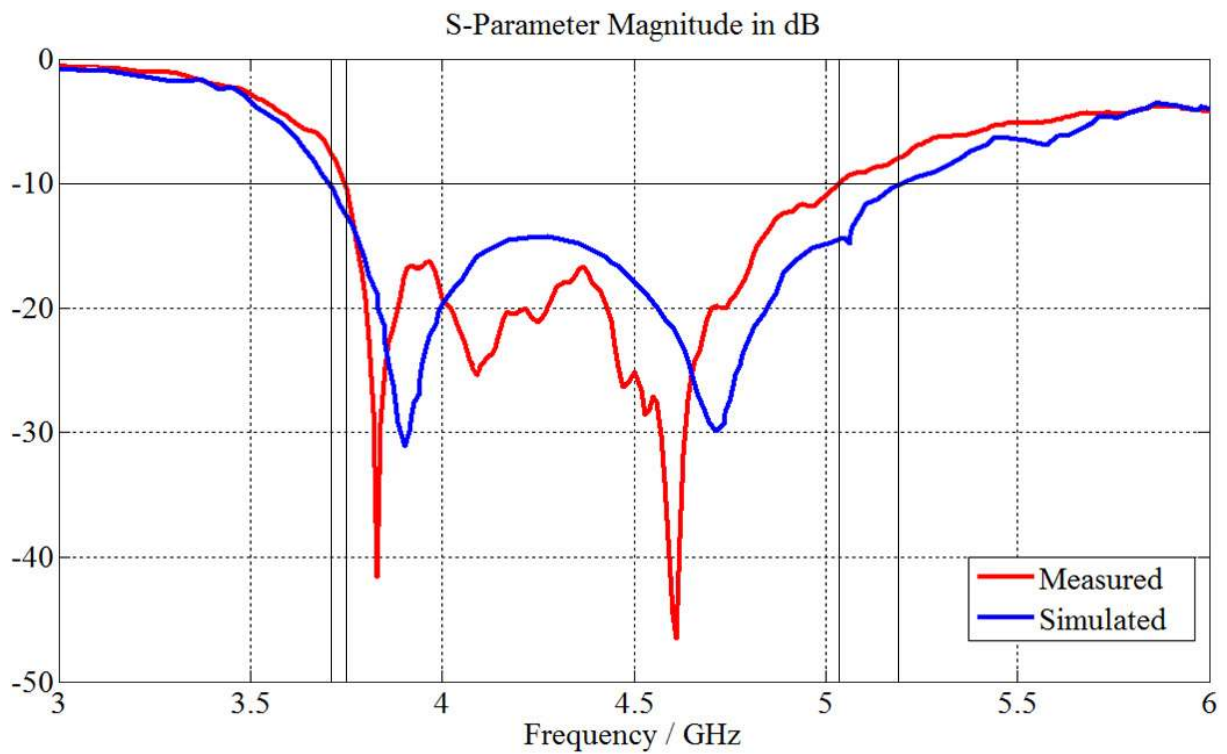
Fig. 5.17– Simulated and measured return loss for the suspended U-slot antenna on a HIS ground plane.

Fig. 5.18 shows that, at the bandgap, any induced currents are restricted to a localized region around the antenna, and never reaches the edges of the ground plane. The realized gain radiation patterns for the suspended U-slot antenna with HIS ground plane are shown in Fig. 5.19, the simulated and measured results are presented. These results were obtained for (a) 3.75 GHz, (b) 4.66 GHz (b) and (c) 5.1 GHz.

5.4 – Summary

Photonic bandgap materials and more recently high impedance ground planes have found most of their radio-frequency applications in the antenna field. High impedance ground planes are particularly interesting as they offer planar solutions. While a conductive sheet is useful as a reflector, it also has several drawbacks such as permitting the propagation of surface waves, and a phase reversal for reflected plane waves. The presence of surface waves has been investigated through analytical modeling and computational analysis. These surface waves have been identified as the normal current that occur on any electrical conductor. The HIS electromagnetic characteristics allow reducing the interactions between the antenna and its backward environment.

	A/m
	34.7
	32.5
	30.4
	28.2
	26.0
	23.8
	21.7
	19.5
	17.3
	15.2
	13.0
	10.8
	8.67
	6.50
	4.34
	2.17
	0

```
Type         Surface Current (peak)
Monitor      h-field (f=4.60) [1]
Maximum-3d   34.6861 A/m at -0.3175 / -0.549926 / -7.4
Frequency    4.60
Phase        320 degrees
```
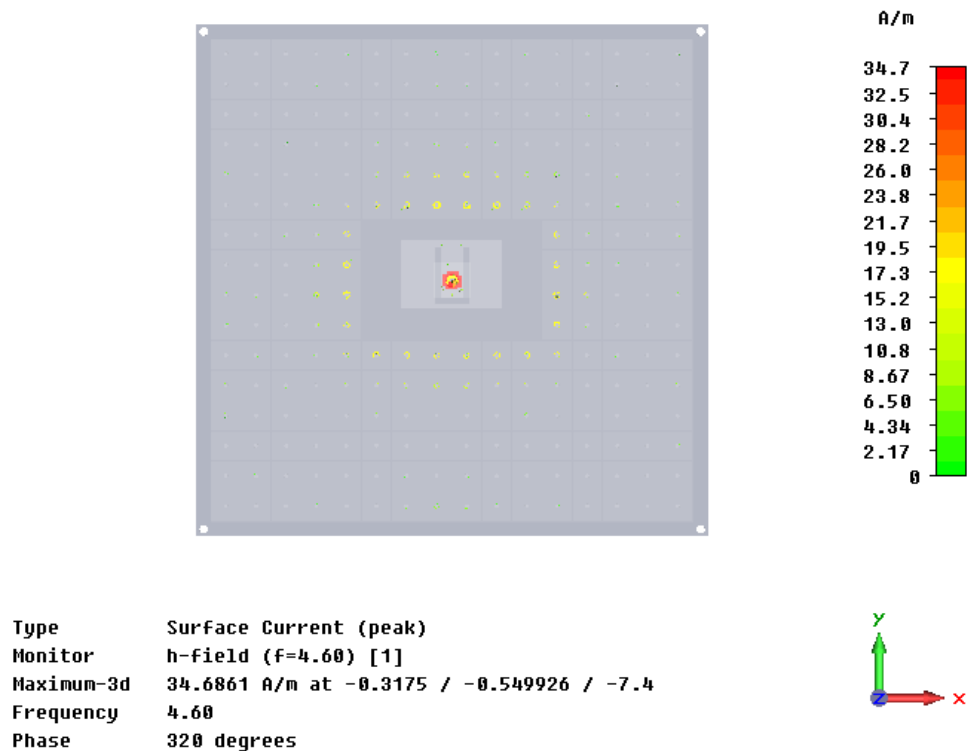
Fig. 5.18 – Surface current at the bandgap frequency center 4.6 GHz, yellow circles surrounding the antenna.
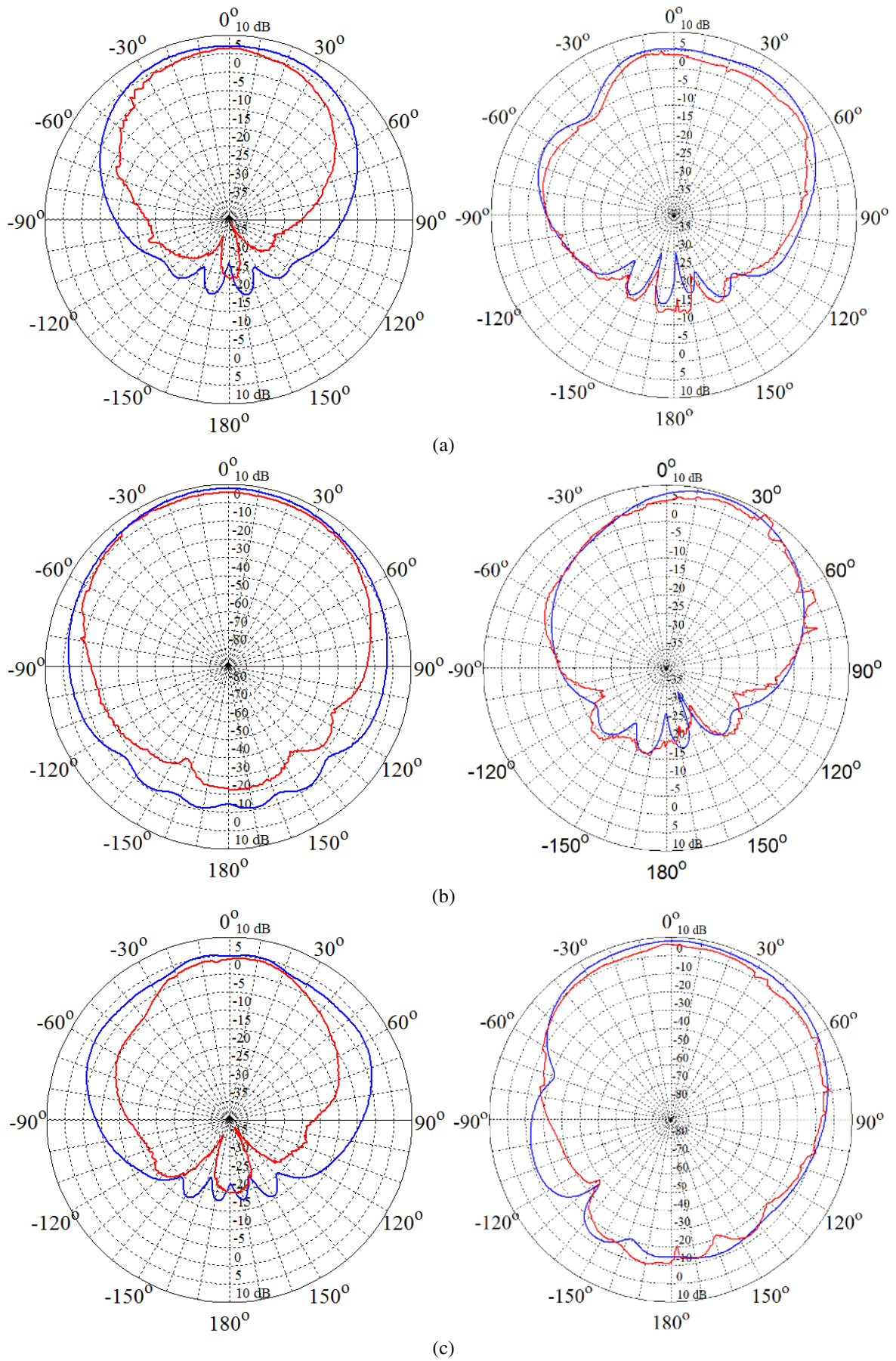
Fig. 5.19 – Farfield realized gain radiation patterns for the, E-plane on the left and H-plane on the left, blue simulated and red measured results: (a) 3.75 GHz, (b) 4.66 GHz and (c) 5.1 GHz.

Chapter 6

Fabry-Pérot Antennas

Another aspect in this investigation is the introduction of a frequency selective surface as a superstrate [70-71]. It is known that high directivity is often achieved by array techniques, while introduction of power dividers inevitably brings in some losses in the design of feeding network. So the FSS superstrate has shown its predominance and is a good candidate to replace the array antenna for achieving high directivity. So, achieving a high directivity with a low-profile antenna, that utilizes a single antenna element opposed to an array, is always a desired design goal. The Fabry-Pérot optical concept is introduced to design this antenna [72-76]. A Fabry-Pérot antenna is formed when a radiated element is placed between two highly reflecting surfaces Fig. 6.1. In its basic configuration, a FP medium consists of two highly reflecting mirrors and is excited by an electromagnetic source located inside or outside the medium. The details of the proposed design are present in this chapter.
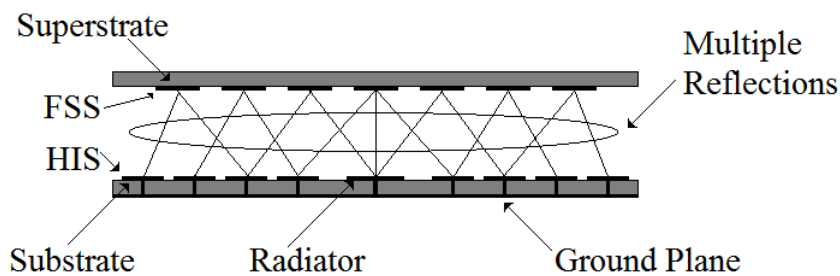
Fig. 6.1 – Illustration of the phenomenon due to the multiple reflections and leaky waves.

6.1 – Fabry-Pérot Interferometer

In 1894, Charles Fabry, a great scientist entered the University of Marseille taking the place of Alfred Pérot in certain academic activities. Since then, the two began to have strong links and by the vast knowledge in electromagnetic theory that Fabry had, together with the

great skills of designing and building instruments that Pérot had, a new equipment was developed [77]. The first official publication regarding this new interferometer occurred in 1897 [78]. Since then the use of the interferometer, called by its original developers etalon meaning "measuring gauge" or "standard". In literature, the etalon is more known as a filter or Fabry-Pérot interferometer.

Fabry-Pérot's are interferometers that consist of two glass plates parallel to each other and arranged coaxially within a short distance forming a kind of optical cavity. The surfaces facing the region between the plates get special treatment so they have a high index of reflection. Thus, a light beam enters the cavity and suffers multiple reflections so that the light rays that escape at each reflection interfere with each other causing the assembly to act as a spectral filter with high resolution.

A way to treat analytically the behavior of a Fabry-Perot's is to consider the FP as an infinite plate with flat surfaces and parallel with thickness "d" the index of refraction n' surrounded on two sides by a medium with index of refraction (Fig 6.2).
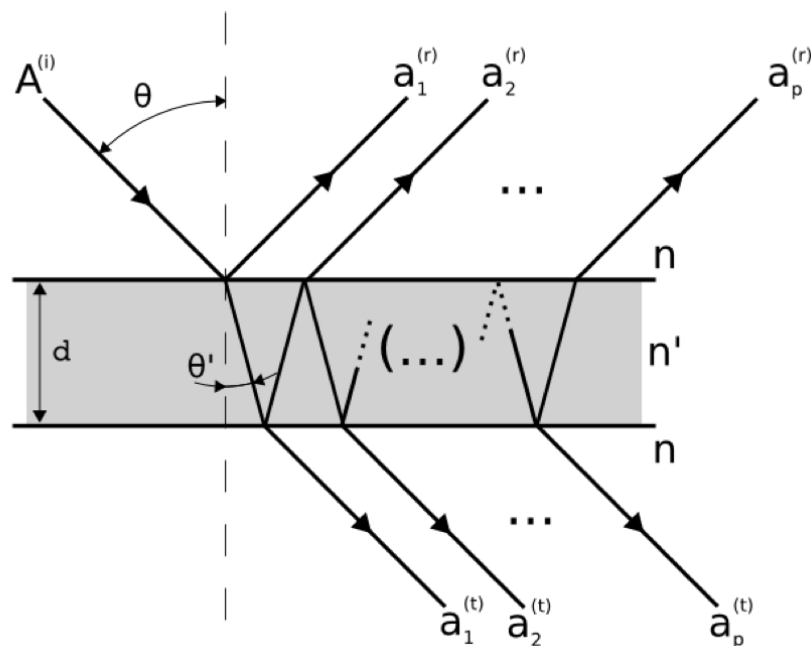
Fig. 6.2 – Graphical representation of a plane light wave with amplitude $A^{(i)}$ focusing on a plate with flat and parallel surfaces. The nth reflected beam is represented by $a_p^{(r)}$ while the nth transmitted beam is represented by $a_p^{(t)}$.

A practical example of how FPs are usually arranged in the space of a collimated telescope medium is shown in Fig. 6.3. In the illustration each point in space of the source

will be represented by a light beam parallel with itself and with a certain angle focusing on the interferometer. The better position to the FP filter is just over the pupil of the system, since that is the point where most light rays passes so the light will be focused.
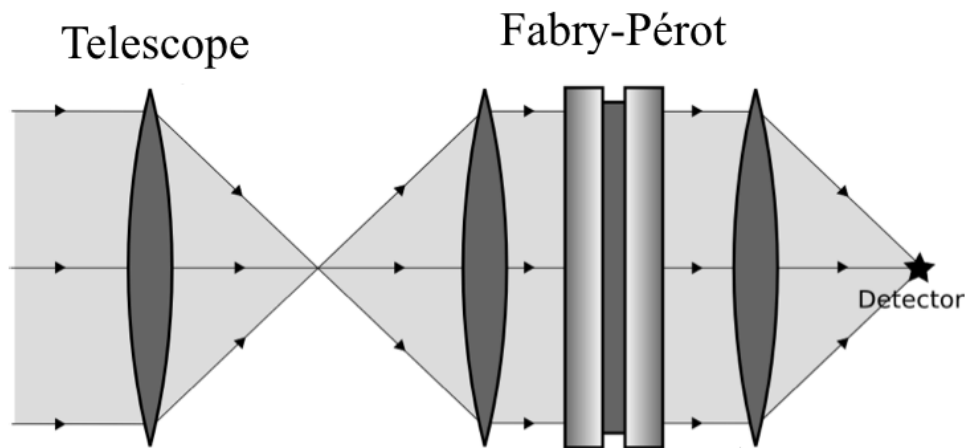
Fig. 6.3 – Positioning of the Fabry-Perot when allocated in a collimated space.

6.2 – The Fabry-Pérot Antenna

The Fabry-Pérot interferometer plays a fundamental role in increasing the phase response of the antenna. The need to increase the phase shift is dictated by the existence of noise, which affects only the phase of the beam without creating a real displacements of the mirror. A way to improve the phase response is to increase length of the beams by bouncing the ray back and forth several times along the medium before it propagates. In such a way the phase difference induced in a single round trip is multiplied by the number of cycles the electromagnetic wave does in the medium.

Many authors [72-76] use a Fabry-Pérot medium to obtain highly directive antennas. The performance improvement is made by placing a resonator inside the FP medium. Two antennas based on a metamaterial ground plane were proposed in chapter 5. The antenna consists of a resonator backed by an EBG material.

Another way for producing a high-directive antenna has been demonstrated in [67-68]. This technique uses a Partially Reflecting Surface to introduce leaky waves and beamforming effects when placed in front of a grounded resonator. A ray theory has been proposed, showing that the directivity of the antenna increases when the reflectivity of the PRS

increases. In this kind of antenna the PRS has been optimized to enlarge the antenna bandwidth. A PRS is a Frequency Selective Surface realized by a periodic distribution of metallic elements printed on a dielectric slab. It can almost entirely reflect incident waves. Inserting a source (i.e., a patch antenna) between the ground plane and the PRS, a highly directive antenna can be obtained. The advantage of such a configuration consists in the possibility of employing a single low-profile radiating element with high gain and low losses in the feeding network for good matching for operating at different frequency bands.

The Fabry-Pérot antennas were realized by employing a Partially Reflective Surface, with suitable frequency selective properties, placed at an adequate distance from a perfect electric ground plane. In our case the ground plane is a High Impedance Surface described in the last section. To demonstrate the proposed approach, two antenna prototypes were built and measured, and the experimental results showed a good agreement with the predicted ones. The PRS is used to introduce leaky waves and beamforming effects when placed in front of a grounded resonator.

The square patches are used as the FSS element type for the superstrate for weakening the polarization sensitivity. FSS is a good candidate as alternatives to dielectric cover for directivity enhancement because they provide higher reflection coefficient and are easy to fabricate. In addition, it makes the antenna composite compact. The FSS array was designed in a square shaped Arlon Diclad 880^{TM} dielectric substrate with the same dimensions as the antenna's substrate (180 mm x 180 mm). Fig. 6.4 shows the square FSS and its dimensions.
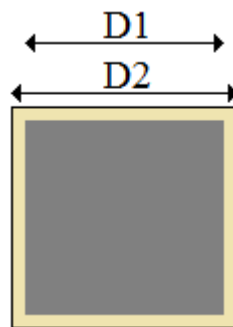
Fig. 6.4 – Square FSS used as the antenna superstrate.

6.2.1 – Fabry-Pérot Patch Antenna

In this section we present a novel design for a low-profile Fabry-Perot antenna, which achieves a high directivity combined with excellent aperture efficiency. The used antenna is the one described in section 5.2. The constructed antenna prototype is presented in Fig. 6.5. The FP antenna is comprised of a single-layer dielectric superstrate backed by a HIS ground

plane. We set the height of the FSS, to be $\lambda_0/2$ in order to achieve the maximum directivity value, where λ_0 is the free-space wavelength at the operating frequency of 12.95 GHz. The design parameters are the same as used in the last chapter. The antenna and the FSS has the following dimensions (Fig. 6.4) $D_1 = 6$ mm and $D_2 = 10$ mm.
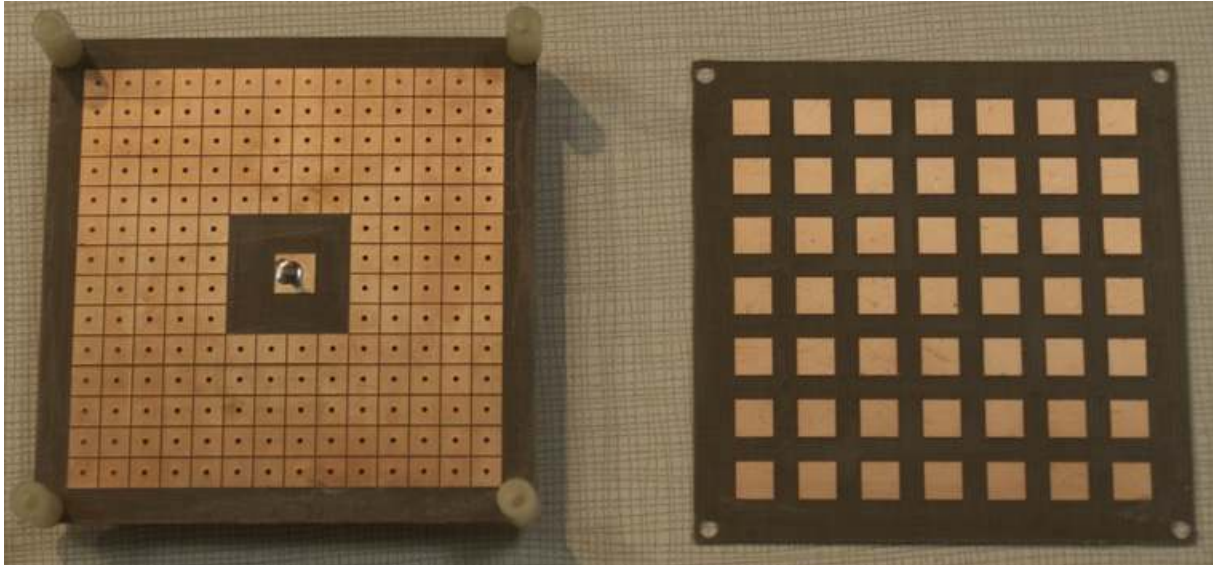
Fig. 6.5 – Fabry-Pérot patch antenna prototype.

To simulate the antenna we used the CST MWS^{TM} and the same full wave solver used before. We compute the return loss characteristics of the antenna considering all conducting and dielectric losses. The proposed design leads itself to a convenient optimization of the return loss, using the FSS, and we are successful in achieving a deeper S11 compared to the antenna without superstrate.
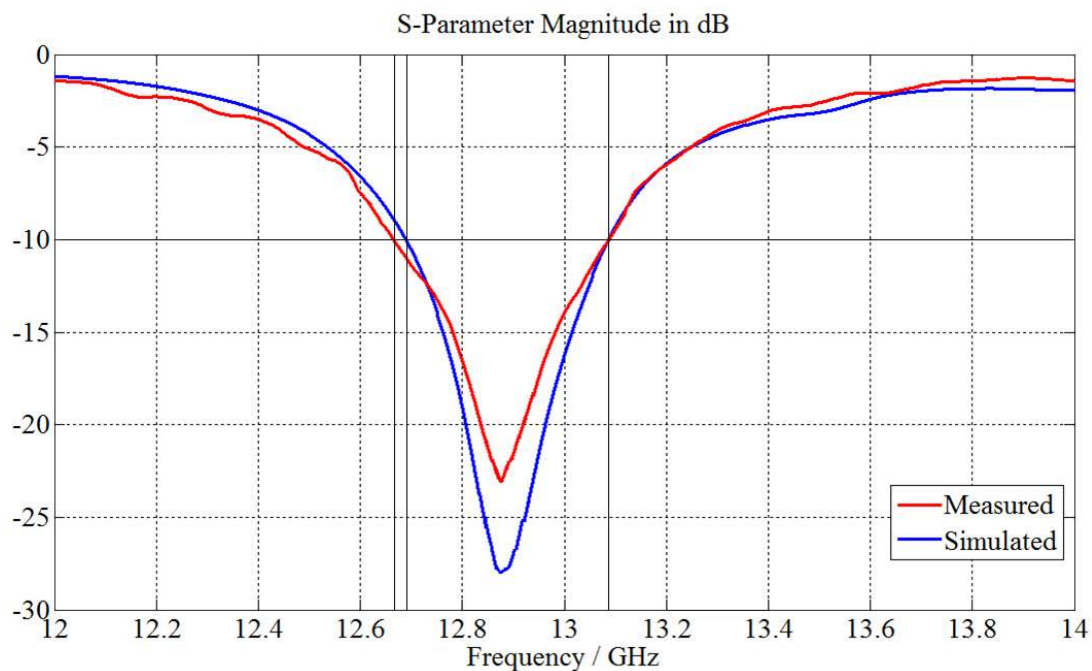
Fig. 6.6 – Return loss for the Fabry-Pérot patch antenna.

The antenna mounted in the anechoic chamber can be shown in Fig. 6.7. The major advantage of the proposed antenna, compared to the antenna without superstrate, is the ability of use only one antenna to increase the antenna directivity.

The radiation patterns of the proposed antenna were measured in an anechoic chamber. The measured radiation patterns of the antenna E-plane are shown in Fig. 6.8 for: (a) 12.7 GHz, (b) 12.9 GHz, and (c) 13.1 GHz. The results for the E-plane are compared to the simulated ones. The H-plane simulated results are also presented. The realized gain pattern reveals a sharp main beam together with low sidelobes. There is a good standard of agreement between simulated and measured results for the E-plane.
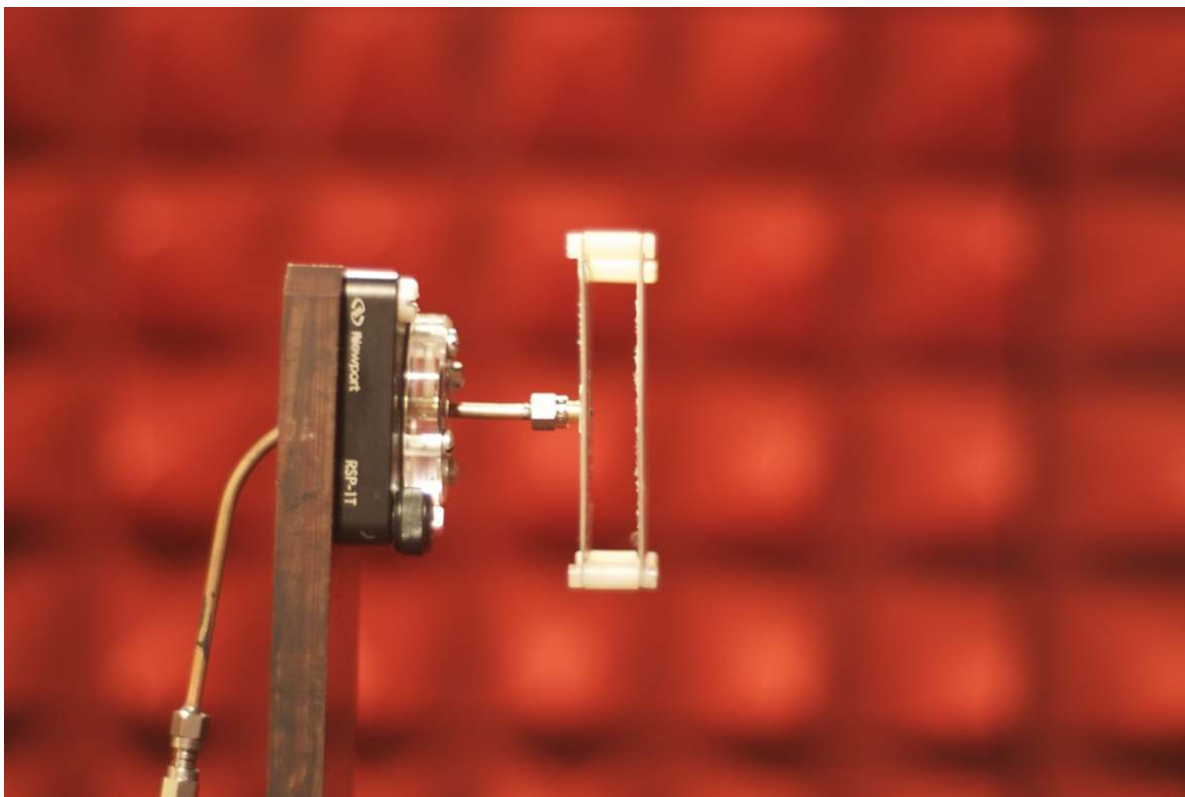
Fig. 6.7 – Fabry-Pérot antenna mounted in the anechoic chamber.

Observing of Fig. 6.8 and Fig. 5.12, it is clear that the use of the FSS superstrate reduces the amplitude of the sidelobes. This agrees well with the trends observed in the simulations. The presence of the FSS superstrate also reduces the level of the E-plane and H-plane beamwidth. The difference (noise) in the radiation patterns can be explain by the losses introduced by cables in the measurements.
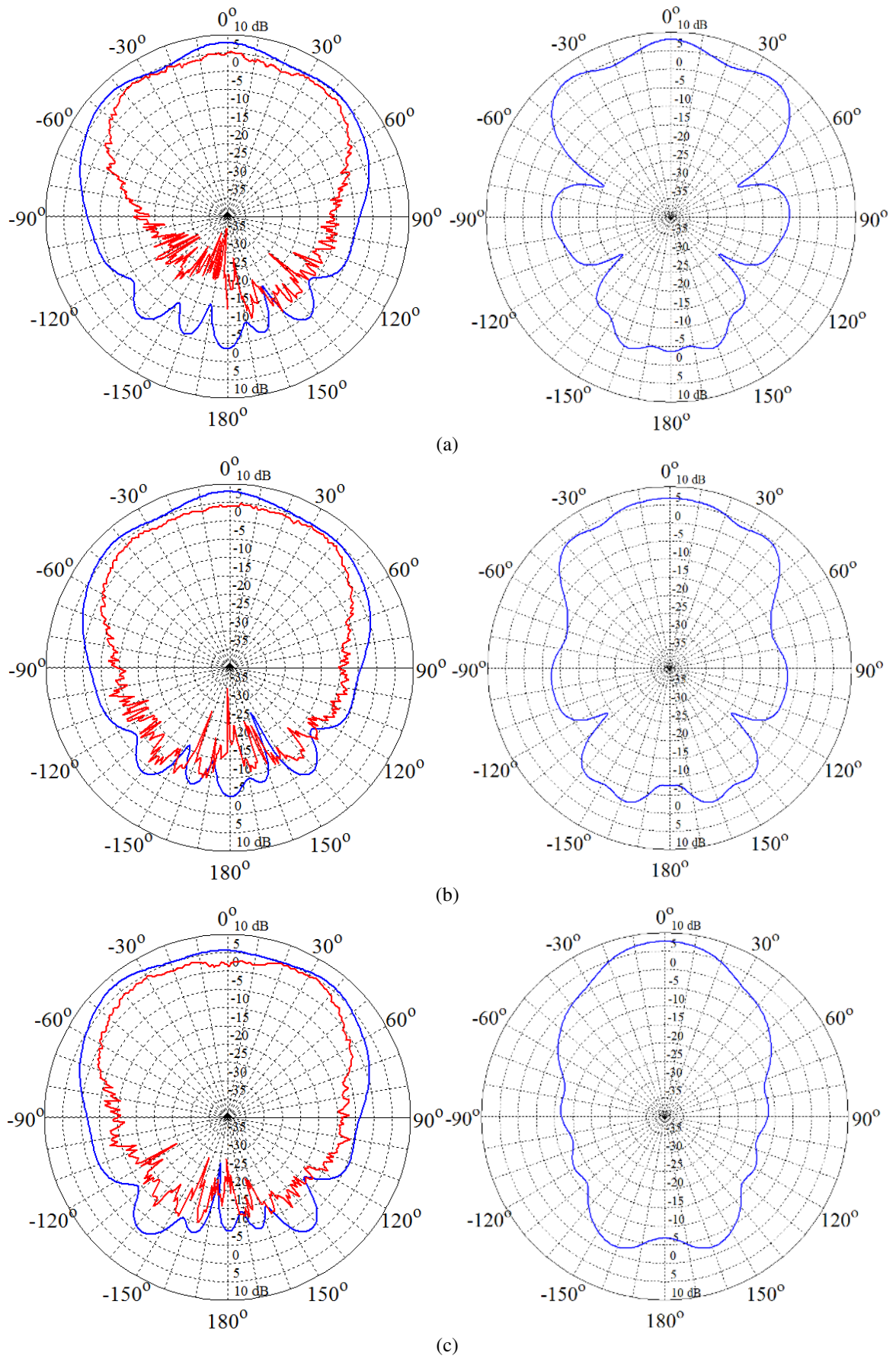
Fig. 6.8 – Realized gain for the Fabry-Pérot patch antenna E-plane on the left and H-plane on the right: (a) 12.7 GHz, (b) 12.9 GHz and (c) 13.1. Blue simulated and red measured results.

6.2.2 – Fabry-Pérot Suspended U-slot Antenna

The proposed scheme in this section is to enlarge the product of directivity and bandwidth by means of a flat gain-frequency response, in which the gain is stable with small ripple within the operation band but abruptly slope-down outside the band. A combined technique is employed to choose a proper FSS-cover with stable frequency responses of reflectivity and reflection phase for minimizing the gain deterioration caused by the variations of reflectivity and phase and to replace the simple patch by mushroom as element of HIS-base, for suppressing the lateral waves including both surface wave and parallel guided wave. These techniques provide the possibility to obtain an optimal compromise between gain and bandwidth due to maximal utilization of the directivity-bandwidth product, and to keep the features of low-profile, high efficiency and single feeding.

The adopted antenna is the one considered in section 5.3 and the FSS superstrate has the following dimensions (Fig. 6.4) $D_1 = 10$ mm, and $D_2 = 17$ mm. Footprint dimensions are the same as the HIS medium 180 mm x 180 mm. The used dielectric substrate for the FSS superstrate is the same Arlon DiClad 880^{TM} used in this thesis. The prototype can be seen in Fig. 6.9 and the antenna mounted in the anechoic chamber in shown in Fig. 6.10.
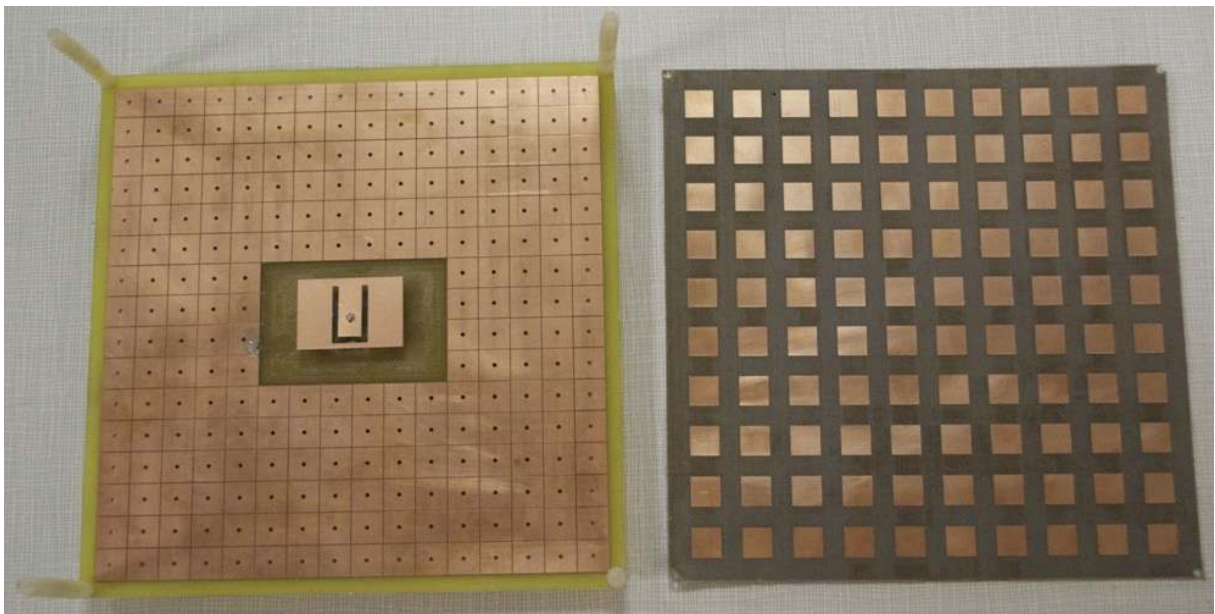
Fig. 6.9 – Constructed suspended U-slot Fabry-Pérot antenna.
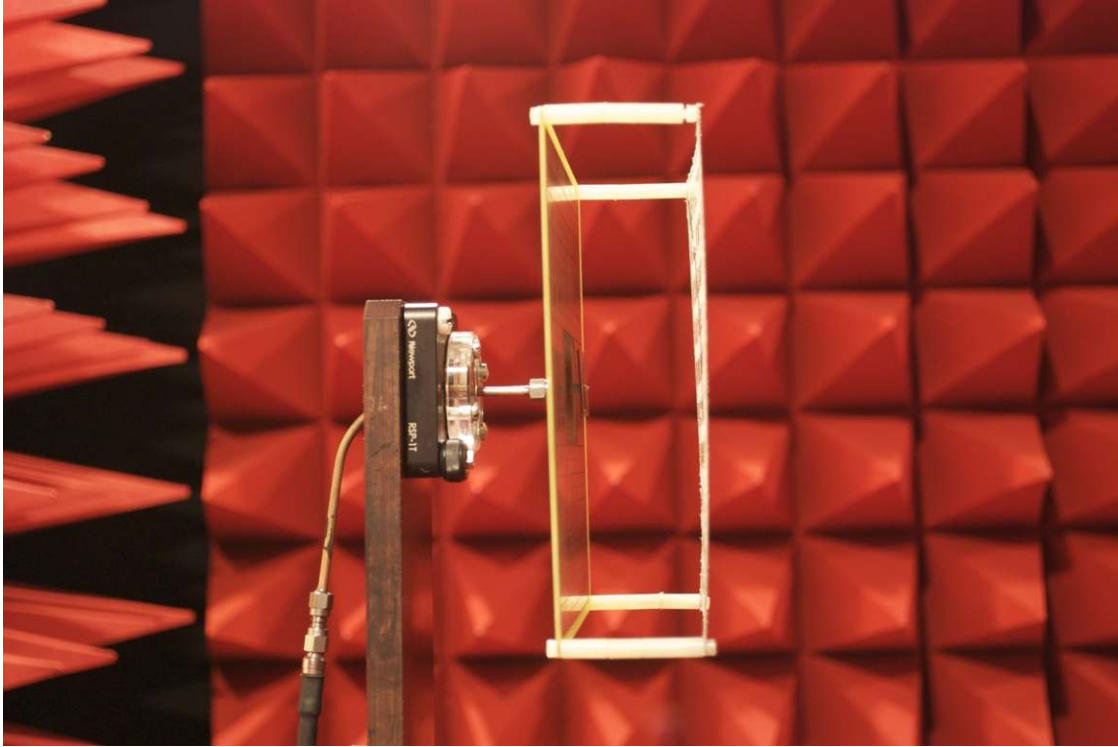
Fig. 6.10 – Fabry-Pérot antenna mounted in the ground plane.

The return loss is shown in Fig. 6.11. It can the noted that the curves present a much a larger bandwidth and deeper S11 compared to the results obtained for the antenna without the superstrate Fig. 5.16. The realized gain (E-plane and H-plane) are shown in Fig. 6.12, again the diagrams present more directive behavior compared to those antennas without FS superstrate. The same simulation process used for the patch antenna is used in this analysis.
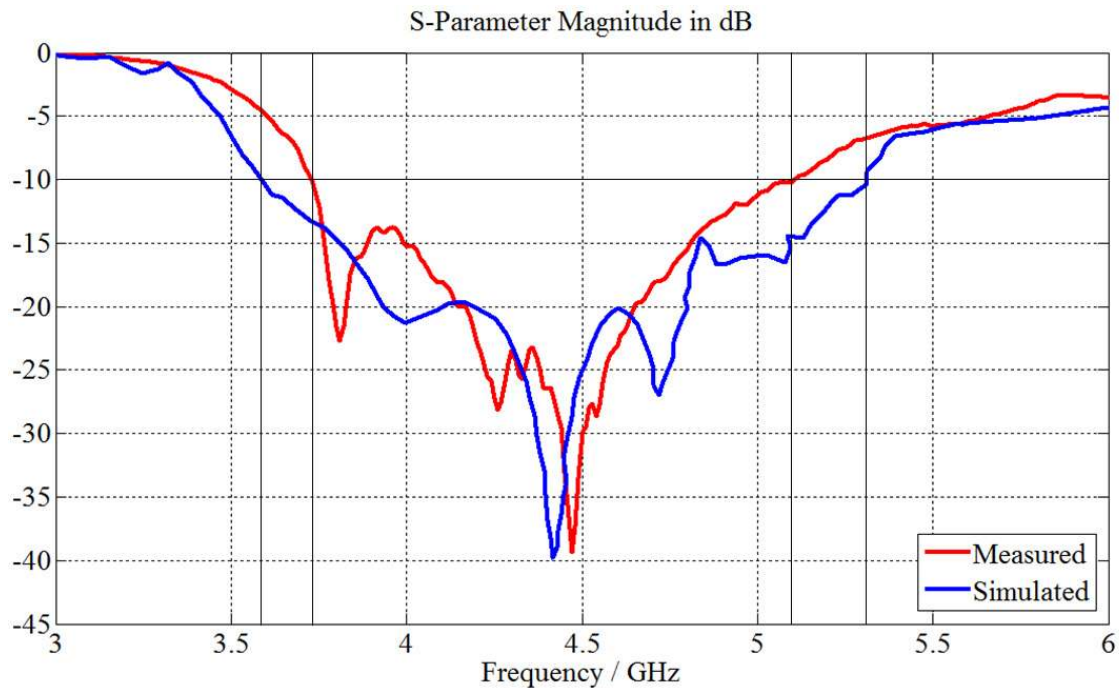
Fig. 6.11 – Return loss for the suspended U-slot antenna.
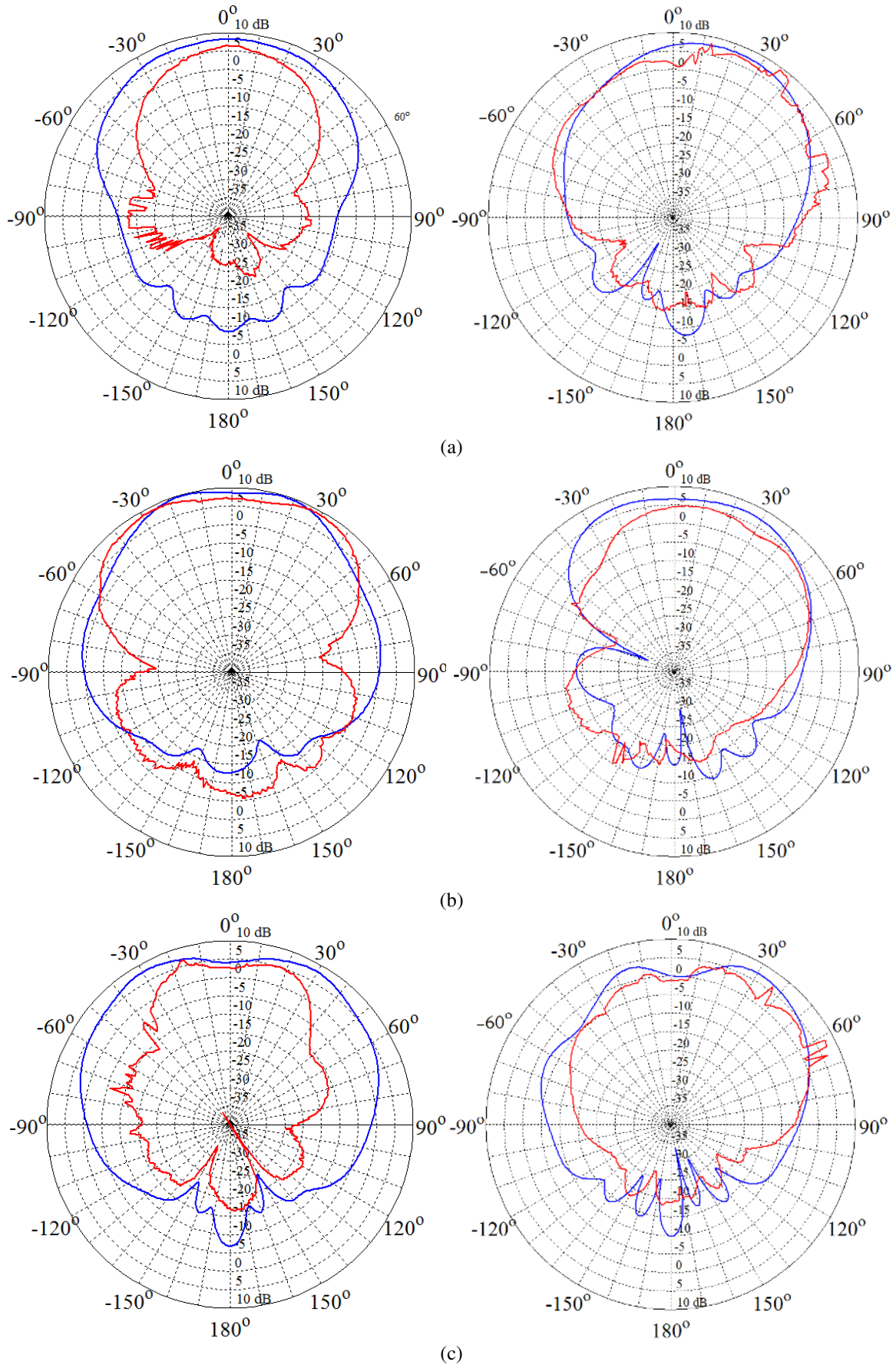
Fig. 6.12 – Realized gain radiation pattern: (a) 3.6 GHz, (b) 4.4 GHz and (c) 5.5 GHz, the E-plane is on the left and H-plane is on the left. Blue simulated and red measured results.

6.3 – Summary

In this chapter double layer periodic structures were analyzed. Employing a patch-type FSS-cover with low-pass rather than band-stop response to get a stable response of reflectivity and reflection phase. The mushroom-type HIS was used as base to suppress the lateral waves between the cover and base, which enlarges the directivity-bandwidth product and supports enough aperture efficiency. Tow samples of Fabry-Pérot antennas are designed by employing these techniques. The measured results are in good agreement with the simulated ones.

Chapter 7

Conclusions

This chapter includes a brief summary of previous chapters and the results of this thesis work. In addition, we will briefly mention the new questions and possible future work that our results have led. In the second chapter, we had a discussion about the theoretical background of materials. We provided theoretical information about the components of a left-handed material, negative permittivity and negative permeability structures, with examples. We also showed that the simultaneous negative values for permittivity and permeability results in negative refraction through Maxwell's equations.

In the third chapter, an introduction to frequency selective surfaces was given in to provide the necessary insight about periodic structures and their applications. These periodic structures are designed on a substrate with metal. These metallic structures behave like inductance and capacitance towards incident waves and hence behave as spatial filters. Therefore, an FSS either blocks or passes waves of certain frequencies in free space. Different shapes like a circle, square, cross, hexagon can be used for FSS fabrication. In addition metamaterial like FSSs were shown.

In the fourth chapter we described the stopband characteristics of the complementary split ring resonator. We have presented the design of a small size ultra wide band monopole antenna. The CSRR exhibits a band-notched characteristic that was designed to block for the UN-II band. The antenna consists of a ring structure as the primary radiation element, a CSRR element with a high quality factor etched in the conductor patch, and a rectangular cut in the ground plane to improve the impedance matching. The dimensions of these elements have been examined and optimized using computer simulation. Simulated and measured results have shown good agreements. The antenna was then analyzed in the time domain to prove that it can be used in UWB systems. The CSRR has good selectivity at both lower and higher frequency ends and flat group-delay response over the whole band. Finally a stopband filter

was designed and then fabricated. This filter is used as an alternative solution to block the UN-II band.

In the fifth chapter, we have seen that while a conductive sheet is useful as a reflector, it also has several drawbacks such as permitting the propagation of surface waves, and a phase reversal for reflected plane waves. To overcome this problem a HIS is used eliminate these surface waves. It has been shown that HIS can suppress surface currents. The high-impedance structure is easily fabricated using printed circuit technology. It was shown that surface waves propagation is suppressed over a certain frequency range on the HIS. The necessary role of the conducting vias is illustrated. The high impedance surface is studied in the context of an antenna ground plane, and its benefits are illustrated in two examples, a patch antenna, and suspended U-shaped. The antennas were simulated and measured with a good agreement achieved between theoretical and experimental results showing the usefulness of the proposed approach. This improves the performance and reduces the thickness of the antenna.

In the sixth chapter, an approach for enhancing the directivity of the antennas described in chapter 5 is presented. The frequency of maximum directivity and the beam width at different frequencies have been predicted. Two antenna prototypes have been fabricated and tested, and a good agreement was achieved. Their single feed system allows to increase the directivity with low complexity compared to feeding networks used in conventional antenna arrays. The directive antennas are composed of a resonating element embedded inside a Fabry-Perot medium. Beside the small thickness and the single feeding device, the weight of our prototypes is low. Thus they could be interesting for applications that require low profile.

The electromagnetic metamaterials described in this work leaves many possibilities for further research. Other filter configurations can be done using the CSSR directly in the transmission line and place on/off switches between the rings for frequency tuning of the bandstop frequency.

Since capacitive loading limits the bandwidth in the HIS, inductive loading can be explore. Ideally, the inductance and capacitance would be used in equal ratio to the impedance of free space. Another possible research topic is considering aperiodic grids in the frequency selective surface superstrate. This could also open new opportunities for high surface efficiency antennas.

The different shapes between the simulated and measured results (Fig. 6.12) for the suspend U-Slot FP antenna might be attributed to the FSS superstrate. The Arlon DiClad 880

has a thickness of 0.768 mm. Once the copper is completely removed in on side and partially in the other the superstrate becomes malleable considering the area 180 x 180 mm, much bigger than the superstrate used in the patch antenna. This flexibility has caused ripples in the structure when the screws were fixed so the structure was not completely flat as in the simulation were the superstrate is completely flat. Therefore a further investigation with different materials should be done.

References

[1] Y. Hao, and R. Mittra, "FDTD Modeling of Metamaterials: Theory and Applications", 1st ed. Artech House Publishers, 2008.

[2] R. Marqués, F. Martín, and M. Sorolla, "Metamaterials with Negative Parameters: Theory, Design and Microwave Applications" 1st ed., Wiley-Interscience, 2008.

[3] C. M. Krowne, and Y. Zhang, "Physics of Negative Refraction and Negative Index Materials: Optical and Electronic Aspects and Diversified Approaches" 1st ed, Springer 2007.

[4] T. J. Cui, D. R. Smith, and R. Liu, "Metamaterials: Theory, Design, and Applications" 1st ed., Springer, 2009.

[5] N. Engheta, and R. W. Ziolkowski, "Electromagnetic Metamaterials: Physics and Engineering Explorations" 1st ed., Willey-IEEE Press, 2006.

[6] G. V. Eleftheriades, and K. G. Balmain, "Negative Refraction Metamaterials: Fundamental Principles and Applications" 1st ed., Willey-IEEE Press, 2005.

[7] C. Caloz, and T. Itoh, "Electromagnetic Metamaterials: Transmission Line Theory and Microwave Applications" 1st ed., Willey-IEEE Press, 2005.

[8] F. Capolino, "Theory and Phenomena of Metamaterial". 1st ed. Taylor & Francis, 2009.

[9] J. C. Bose, "On the rotation of plane of polarization of electric waves by a twisted structure," Proc. Roy. Soc., vol. 63, pp. 146–152, 1898.

[10] H. Lamp, ''On Group-Velocity,'' Proc. London Math. Soc. 1, pp. 473-479, 1904.

[11] V. G. Veselago, "The electrodynamics of substances with simultaneously negative values of eps and mu", Soviet Phys. Usp., Vol. 10, pp. 509-514, 1968.

[12] W. Kock, ''Metallic delay lenses,'' Bell Syst. Tech. J., Vol. 27, pp. 58-82, 1948.

[13] D. R. Smith, W. J. Padilla, D. C. Vier, S. C. Nemat-Nasser, and S. Schultz. "Composite medium with simultaneously negative permeability and permittivity," Phys. Rev. Lett., vol. 84, no. 18, pp. 4184–4187, May 2000.

[14] J. B. Pendry et al., ''Extremely Low Frequency Plasmons in Metallic Mesostructures,'' Phys. Rev. Lett., Vol. 76, Issue 25, pp. 4773-4776, 1996.

[15] J. B. Pendry, "Negative refraction makes a perfect lens'', Phy. Rev. Lett., Vol. 85, pp. 3966–3969, 2000.

[16] J. A. Kong, "Theorems of Bianisotropic Media" Proc. of the IEEE Vol. 60, Issue 9, pp. 1036-1046, Sep. 1972.

[17] A. Sihvola, ''Metamaterials in Electromagnetics,'' Metamaterials, Vol. 1, Issue 1, pp.2-11, 2007.

[18] D. R. Smith, D. C. Vier, N. Kroll, and S. Schultz, "Direct calculation of permeability and permittivity for a left-handed metamaterial," App. Phys. Lett., vol. 77, Issue 14, pp. 2246–2248, Oct. 2000.

[19] E. Yablonovitch, T. Gmitter, and K. Leung, ''Photonic Band Structure: the Facecentered Cubic Case Employing Nonspherical Atoms,'' Phys. Rev. Lett., Vol. 67, Issue 17, pp. 2295-2298, 1991.

[20] H. Boutayeb, T. A. Denidni, K. Mahdjoubi, A.-C. Tarot, A.-R. Sebak, and L. Talbi, ''Analysis and Design of a Cylindrical EBG-Based Directive Antenna,'' IEEE Trans. on Ant. and Prop., Vol. 54, Issue 1, pp. 211-219, 2006

[21] Y. Zhao, Y. Hao, and C. G. Parini, ''Radiation Properties of PIFA on UC-EBG Substrates,'' Micro. and Opt. Tech. Letts., Vol. 44, Issue 1, pp. 21-24, January 5, 2005.

[22] L. Damaj, A. C. Lepage, and X. Begaud, " Low profile, directive and very wideband antenna on a high impedance surface", Proceedings of the Fourth European Conference on Antennas and Propagation (EuCAP) 2010, pp. 1-5, Apr. 2010.

[23] D. Rittenhouse, "An optical problem, proposed by Mr. Hopkinson, and solved by Mr. Rittenhouse" Trans. Amer. Phil. Soc. Vol. 2, pp. 201-206, 1786.

[24] T. K. Wu, "Frequency Selective Surfaces and Grid Array", 1st ed., John Wiley and Sons, Inc., 1995.

[25] B. A. Munk, "Frequency Selective Surfaces: Theory and Design", 1st ed. John Wiley & Sons, Inc., 2000.

[26] T. Cwik, R. Mittra, K. Lang and T. Wu, T., "Frequency Selective Screens", IEEE Ant. and Prop. Soc. News., Vol. 29, Issue 2 pp. 5 – 10, 1987.

[27] R. M. S. Cruz, P. H. F. Silva, and A. G. d'Assunção, "Neuromodeling stop band properties of Koch Island patch elements for FSS filter design," Microwave and Optical Technology Letters, v.51, pp. 3014-3019, 2009.

[28]   S. Lee, G. Zarrillo, C. Law, "Simple Formulas for Transmission Through Periodic Metal Grids or Plates", IEEE Trans. Ant. Prop. 30, 904-909, Sep. 1982.

[29]   F. T. Ulaby, "Fundamentals of Applied Electromagnetics", 3rd ed. Prentice Hill, 2001.

[30]   B. A. Munk, "Finite Antenna Arrays and FSS", 1st ed. John Wiley & Sons, Inc., 2003.

[31]   Y. He, H. Peng, S. D. Yoon , P. V. Parimic, F. J. Rachford, V. G. Harris, and C. Vittoria, "Tunable NIM using yttrium iron garnet", Jour. of Magnetism and Magnetic Mat., Vol. 313, Issue 1. pp. 187-191, Jun 2007.

[32]   A. Alù, and E. Nader,   "Evanescent Growth and Tunneling Through Stacks of Frequency-Selective Surfaces", IEEE Ant. and Wir. Prop. Letts. Vol. 04 pp. 417-420, Dec. 2005.

[33]   D. Sievenpiper, L. Zhang, R. F. J. Broas, N. G. Alexopolous, E. Yablonovitch, "High-Impedance Electromagnetic Surfaces with a Forbidden Frequency Band", IEEE Trans. on Micro. Theo. and Tech. Vol. 47, Issue 11, pp. 2059-2074. Nov. 1999.

[34]   J. R. Sohn, K. Y. Kim, H.-S. Tae, and H. J. Lee "Comparative study on various artificial magnetic conductors for low-profile antenna." Progress In Electromagnetics Research Vol. 61, pp. 27–37, 2006.

[35]   Y. E. Erdemli, K. Sertel, R. A. Gilbert, D. E. Wright, J. L. Volakis, "Frequency-Selective Surfaces to Enhance Performance of Broad-Band Reconfigurable Arrays" Antennas and Propagation, IEEE Transactions on, pp. 1716- 1724. Dec 2002

[36]   J. D. Shumpert, W. J. Chappell, and L. P. B. Katehi, "Parallel-plate mode reduction in conductor-backed slots using electromagnetic band gap substrates," IEEE Trans. Microwave Theory Tech., vol. 47, pp. 2099–2104, Nov. 1999.

[37]   U. Yeo, and D. Kim, "Novel Design of a High-gain and Wideband Fabry-Pérot Cavity Antenna Using a Tapered AMC Substrate", International Journal of Infrared and Millimeter Waves, Dec 2008.

[38]   G. Gampala, and A. B. Yakovlev, "Wideband High Impedance Surface for X-Band Antenna Applications" In IEEE Antennas and Propagation Society International Symposium, pp. 1329-1332, Jun 2007.

[39]   S. Maci and P. S. Kildal, "Hard and soft Gangbuster surfaces," Proc. URSI International Symposium Electromagnetic Theory, Pisa, Italy, pp. 290-292May 2004,

[40]   S. Maci, M. Caiazzo, A. Cucini, and M. Casaletti, "A pole-zero matching methodfor EBG surfaces composed of a dipole FSS printed on a grounded dielectric slab," IEEE Trans. Antennas Propagat., Vol. 53, no. 1, pp. 70-81, Jan. 2005.

[41] G. Goussetis, Y. Guo, A. P. Feresidis, and J. C. Vardaxoglou, "Miniaturized and multi-band artificial magnetic conductors and electromagnetic band gap surfaces," IEEE Antennas Propagation Society Int. Symp., 20-25 June 2004, Vol. 1, pp. 293-296.

[42] M. Hiranandani, A. B. Yakovlev, and A. A. Kishk, "Artificial magnetic conductors realized by frequency selective surfaces on a grounded dielectric slab for antenna applications," IEEE Proceedings Microwave Antennas Propagation, Vol. 153, no. 5, pp. 487-493, Oct. 2006.

[43] A. A. Kalteh, R. Fallahi, and M. G. Roozbahani, "A novel Microstrip-fed UWB Circular slot antenna with 5-Ghz Band-notch characteristics", IEEE International Conference on Ultra-wideband (ICUWB2008), vol.1, 2008, pp.117-120.

[44] M. Ojaroudi, G. Ghanbari, N. Ojaroudi, and C. Ghobadi, "Small square monopole antenna for UWB applications with Variable frequency band-notch function", IEEE Antennas and Wireless Propagation Letters, vol.8, 2009.

[45] X. Begaud, "Ultra wideband wide slot antenna with band-rejection characteristics" Proceedings of the First European Conference on Antennas and Propagation (EuCAP) 2010, pp. 1-6, Nov. 2006.

[46] H. W. Liu, C. H. Ku, T. S. Wang, and C. F. Yang, "Compact monopole antenna with band-notched characteristic for UWB applications", IEEE Antennas and Wireless Propagation Letters, vol. 9, 2010.

[47] B. Ahamadi, and R. F. Dana, "A miniaturized monopole antenna for ultra- wideband applications with band-notch filter", IET Microwave antennas Propagations, vol.3, 2009, pp.1224-1231.

[48] W. T. Lo, X. W. Shi, and Y. Q Hei, "Novel Planar UWB Monopole Antenna With Triple Band-Notched Characteristics", IEEE Ant. And Wire. Prop. Letters, Vol. 8, pp. 1094-1098, Oct. 2009.

[49] L. Zhu, S. Sun, and W. Menzel, "Ultra-wideband (UWB) bandpass filters using multiple-mode resonator", IEEE Microwave Wireless Compon Lett 11 (2005), 796–798.

[50] C.Y. Hung, M.H. Weng, Y.K. Su, R.Y. Yang, and H.W. Wu, "Design of compact and sharp rejection UWB BPFs using interdigital stepped impedance resonators", IEICE Electron Lett 1 (2007), 1652–1654.

[51] M. R. Silva, C. L. Nóbrega, A. M. Zenaide, P. H. F. Silva, and A. G. d'Assunção, "Monopolos Circular e Elíptico de Microfita para Sistemas UWB," In: Anais do Simpósio Brasileiro de Telecomunicações (SBrT 2008), Recife, PE, v.1, pp.1-4. 2008.

[52] K. G. Thomas, and N. Lenin, "Ultra wideband printed monopole antenna", Microwave Opt. Technol Lett, Vol. 49, pp. 1082-1084, May 2007.

[53] C. H. Hsu, "Planar multilateral disc monopole antenna for UWB application", Microwave Opt. Technol Lett, vol. 49, pp. 1101-1103, May 2007.

[54] K. Siwiak and D. McKeown, "Ultra-wideband Radio Technology", Wiley Intercienci, 1st ed. 2004.

[55] B. Allen, M. Dohler, E. Okon, W. Malik, A. Brown, and D. Edwards, "Ultra Wideband Antennas and Propagation for Communications, Radar and Imaging" Wiley Intercienci, 1st ed. 2006.

[56] V. H. Rumsey, "Frequency-independent antennas", IRE National Convention Record, Vol. 1. pp. 251–259, 1957.

[57] S. Uda, and Y. Mushiake. "The input impedances of slit antennas," Tech. Rep. of Tohoku Univ., Vol. 14, No 1. pp. 46-59, Sept. 1949.

[58] W. Runge, "Polarization diversity reception", U.S. Patent 1,892,221, 27 Dec. 1932.

[59] C. A. Balanis, "Antenna Theory: Analysis and Design", 3rd ed., Wiley Interscience, 2005.

[60] J. A. Stratton "Electromagnetic Theory (IEEE Press Series on Electromagnetic Wave Theory)" Wiley-IEEE Press, 2007.

[61] J. B. Pendy, J. B. A. J. Holden, D. J. Robbins, and W. J. Stewart, "Magnetism from conductors and enhanced nonlinear phenomena", IEEE Trans. Microw. Theory Tech., vol. 47, pp. 2075– 2084, Nov. 1999.

[62] R. Marqués, F. Mesa, J. Martel, and F. Medina, "Comparative analysis of edge- and broadside-coupled split ring resonators for metamaterial design—Theory and experiment," IEEE Trans. Antennas Propag., vol. 51, no. 10, pp. 2572–2581, Oct. 2003.

[63] H. G. Booker, "Slot aerials and their relation to complementary wire aerials (Babinet's principle)." J. IEE, vol. 93, pt. III–A, no. 4, pp. 620–626, May 1946.

[64] G. A. Deschamps, "Impedance properties of complementary multiterminal planar structures." IRE Trans. Antennas Propag., vol. AP–7, pp. 371–378, Dec. 1959.

[65] J. D. Baena, J. Bonache, F. Martín, R. M. Sillero, F. Falcone, T. Lopetegi, M. A. G. Laso, J. García–García, I. Gil, M. F. Portillo, and M. Sorolla, "Equivalent-Circuit Models for Split-Ring Resonators and Complementary Split-Ring Resonators Coupled to Planar Transmission Lines", IEEE Trans. On Microw. Theory and Tech., vol. 53, no 4, pp. 1451 – 1461, Apr. 2005.

[66] D. B. Brito, X. Begaud, A. G. D'Assuncao, and H. C. C. Fernandes, "Ultra wideband monopole antenna with Split Ring Resonator for notching frequencies", EuCAP 2010. 4th European Conference on Antennas and Propagation, pp. 1 - 5, Apr. 2010.

[67] A. Thior, A. C. Lepage, and X. Begaud, "Low profile, directive and ultra wideband antenna on a high impedance surface", EuCAP 2009. 3rd European Conference on Antennas and Propagation, pp. 3222 - 3226, Mar. 2009.

[68] P. Deo, A. Mehta, D. Mirshekar-Syahkal, and H Nakano, "An HIS-Based Spiral Antenna for Pattern Reconfigurable Applications", IEEE Antennas and Wireless Propagation Letters, Vol. 8, pp. 196-199, Nov. 2009.

[69] M. G. Floquet, "Sur les equations différentielles Iinéaires a coefficients périodiques," Annale École Normale Superieur, pp. 47-88, 1883.

[70] A. Foroozesh, and L. Shafai, "Investigation Into the Effects of the Patch-Type FSS Superstrate on the High-Gain Cavity Resonance Antenna Design", IEEE Trans. on Ant. and Propag, Issue 2, Vol. 58, pp. 258-270, Dec. 2009.

[71] Y. Ge and K. P. Esselle, "Designing high gain microwave antennas by optimising a FSS superstrate", European Microwave Conference, pp. 412-415, Oct 2007.

[72] F. Costa, E. Carrubba, A. Monorchio, and G. Manara, "Multi-Frequency Highly Directive Fabry-Perot based Antenna", IEEE AP-S 2008 Antennas and Propagation Society International Symposium, pp. 1-4, Jul. 2008.

[73] J. Yeo, and D. Kim, "Novel Design of a High-gain and Wideband Fabry-Pérot Cavity Antenna Using a Tapered AMC Substrate", Journal of Infrared, Millimeter and Terahertz Waves, Vol. 30, No. 3, pp. 217-224, Dec. 2008.

[74] J. R. Kelly, and A. P. Feresidis, "Array Antenna With Increased Element Separation Based on a Fabry–Pérot Resonant Cavity With AMC Walls", IEEE Transactions on Antennas and Propagation, Vol. 57, Issue 3, pp. 682-687, Mar. 2009

[75] N. Guérin, S. Enoch, G. Tayeb, P. Sabouroux, P. Vincent, and H. Legay, "A Metallic Fabry–Perot Directive Antenna" Vol. 54, No. 1, pp. 220-22, Jan 2006.

[76] J. S. Zheng1, L. X. Chen1, Y. G. Lu, and C. H. Liu, "A High-gain Wideband Antenna with Double Fabry-Pérot Cavities", International Journal of Infrared and Millimeter Waves, Vol. 29. No. 9, pp. 839-845, Jul 2008.

[77] J. F. Mulligan, "Who were Fabry and Pérot?", American Journal of Physics, 1998, vol. 66, pp. 797.

[78] A. Perot, and C. Fabry, "Sur les franges des lames minces argentées et leus application a la mesure de petites épasseur d'air", Ann. Chim. Phy., 1987, vol. 12, p. 459